Surface scattering dynamics of graphene and graphite

Dissertation
zur Erlangung des mathematisch-naturwissenschaftlichen Doktorgrades
„Doctor rerum naturalium“
der Georg-August-Universität Göttingen

im Promotionsprogramm Chemie
der Georg-August University School of Science (GAUSS)

vorgelegt von
Sven Meyer
aus Hannover

Göttingen, 2022

Betreuungsausschuss:

Prof. Dr. Alec M. Wodtke
Institut für Physikalische Chemie, Max-Planck-Institut für Biophysikalische Chemie

Prof. Dr. Martin A. Suhm
Institut für Physikalische Chemie

Referent:
Prof. Dr. Alec M. Wodtke
Institut für Physikalische Chemie, Max-Planck-Institut für Biophysikalische Chemie

Korreferent:
Prof. Dr. Martin A. Suhm
Institut für Physikalische Chemie

Weitere Mitglieder der Prüfungskommission:

Prof. Dr. Theofanis Kitsopoulos, Department of Chemistry, University of Crete

Prof. Dr. Dirk Schwarzer, Max-Planck-Institut für Biophysikalische Chemie

Prof. Dr. Jürgen Troe, Institut für Physikalische Chemie

Dr. Daniel Steil, 1. Physikalisches Institut

Tag der mündlichen Prüfung: 15.03.2022

Abstract

Since its first successful preparation in 2004, graphene has been extensively studied because of its outstanding mechanical, thermal and electronic properties. Graphene is an especially interesting material because of its zero-bandgap electronic structure, which puts it right on the edge between metals and semiconductors. Up to this point, non-adiabatic interactions have only been observed on metal surfaces. In this work, vibrational excitation of NO was investigated as a probe for non-adiabatic interactions by scattering a molecular beam of NO from epitaxial graphene on Pt(111) (Gr/Pt) and highly oriented pyrolytic graphite (HOPG). No signs of non-adiabatic interactions were found. Instead, thermal vibrational excitation of NO was observed on Gr/Pt as a result of a trapping-desorption scattering mechanism, which is supported by state to state time of flight measurements. In contrast, on HOPG only direct scattering without vibrational excitation has been observed. Further state to state time of flight experiments revealed a very efficient coupling between the surface and the kinetic energy of the NO, resulting in a high translational energy loss of up to 80% for Gr/Pt, and up to 66% for HOPG. An enhanced sticking probability of NO on graphene compared to HOPG was observed that could be modeled using detailed balance. This enhanced sticking probability makes graphene an interesting substrate for catalysts, where it can act as a net to catch the reactands.

Contents

1 Introduction

Zero, one and two dimensional materials have been of great research interest for more than a decade now, because of their outstanding properties, which reach from strongest to softest, from most insulating to most conducting. These Materials include 0D Fullerenes, 1D Carbon nano tubes (CNTs), 2D single- and multi layered graphene, hexagonal boron-nitride (hBN), $NbSe_2$,TaS_2, MoS_2 and many more.[1,2] Out of all of these materials, graphene, a zero bandgap semiconductor, was discovered about 20 years ago[3] and thus has been investigated for a long time, leading to numerous (possible) applications, not only in reasearch. Depending on the type of graphene used (flakes, low or high quality sheets, or even CNTs, see Figure 1.1), possible applications include (flexible) electronics[4,5], optical or gas sensors and lasers[4–7], support for chemical reactions or membranes[8], coatings for air- and spacecraft[9–12] or anti-corrosion coatings of metals,[1,13] made possible by its exceptional thermal and mechanical properties.[14,15] Most applications lead to contact of the graphene with reactive species such as O_2, NO_x or H_2O, and the use in air- and spacecraft also leads to the necessity to withstand extreme conditions, such as high temperatures or collisions with high energy gas molecules or ions.

Molecule surface scattering has been a very useful tool to understanding basic interactions of gas molecules with different types of surfaces, from noble metal single crystals, insulators, metal oxides to corrugated and stepped surfaces.[17] These experiments are usually carried out under ultra-high vacuum (UHV), and use well defined conditions to provide experimental data to test and improve current theoretical methods. Among others, they have helped in understanding the breakdown of the Born-Oppenheimer approximation during the interaction of gas molecules with metal surfaces,[18–22] the effect of internal degrees of freedom on dissociation dynamics[20,23,24] or the oxidation of CO on platinum, a reaction that was long thought to be completely understood.[25,26]

As an example, in 1987, Kay *et al.* investigated the excitation of the umbrella vibration in NH_3 when scattered from a Au(111) surface.[27] They found the vibrational excitation probability to be completely independent of the surface temperature T_S (see Figure 1.2 a), but the normal incidence translational energy had a very strong effect (Figure 1.2 b). As

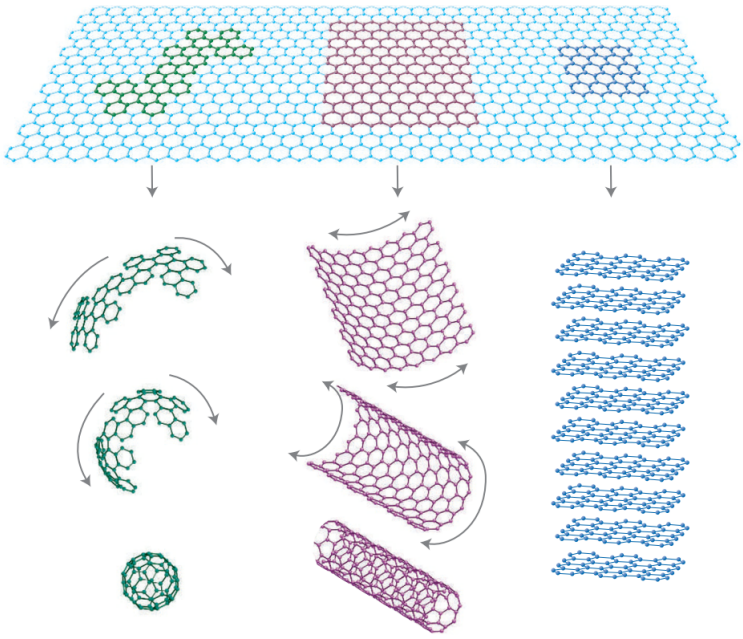

Figure 1.1: Starting with graphene, a 2D material, all other forms can be achieved: 0D Fullerenes (left) via introduction of five-membered rings, 1D Carbon nano tubes (CNTs, middle) by rolling a graphene sheet and 3D graphite (right) by stacking multiple layers of graphene. Reprinted by permission from Springer Nature Customer Service Centre GmbH from reference [16], Copyright (2007).

long as the normal component of the translational energy was less than one vibrational quantum of the umbrella mode, no excitation was observed. This threshold-behavior, and the independence of the surface temperature is expected for a purely mechanical (adiabatic) interaction of a molecule with the surface. The energy required for the vibrational excitation is supplied only by the normal component of the kinetic energy of the molecule. Two years earlier in 1985, Rettner *et al.* studied the vibrational excitation of nitric oxide scattered from a Ag(111) surface.[28] They observed a weak dependence on the incidence translational energy, and no threshold was present (Figure 1.3 b). However, opposite to the purely mechanical interaction of NH_3/Au(111), a strong dependence on the surface temperature T_S was observed (Figure 1.3 a). These observations were explained with an interaction of the NO molecules with thermally excited electron hole pairs (EHPs) of the metal surface. This non-adiabatic electron-hole-pair mechanism was later confirmed by further experimental evidence.[29–31] One of these experiments is the vibrational relaxation of highly vibrationally excited NO scattered from Au(111) and LiF, as shown in Figure 1.4. Multiquantum vibrational relaxation is observed for NO/Au(111) but nearly completely absent for NO/LiF. This result is reasonable in the picture of an EHP mechanism, as no electron-hole pairs are present in an insulator like LiF, but are available in

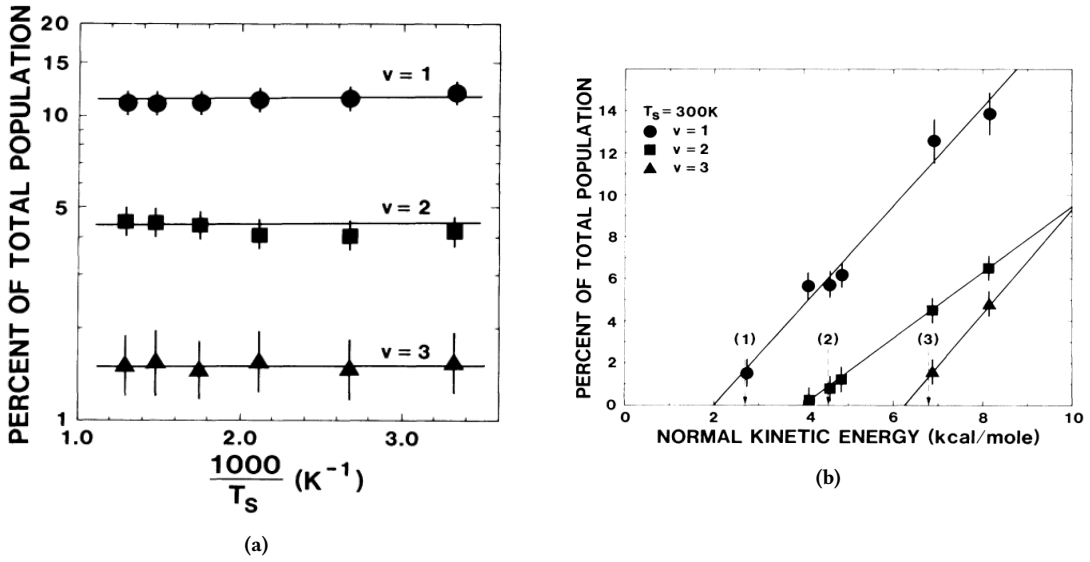

Figure 1.2: Vibrational excitation of the umbrella mode of NH_3 during a collision with Au(111). (a) No surface temperature dependence on the vibrational excitation probability is observed, but the excitation probability strongly depends on the normal incidence translational energy E_n, showing a threshold behavior (b). If E_n exceeds one or multiple quanta of vibrational energy, excitation is observed. Reprinted with permission from reference [27]. Copyright (1987) by the American Physical Society.

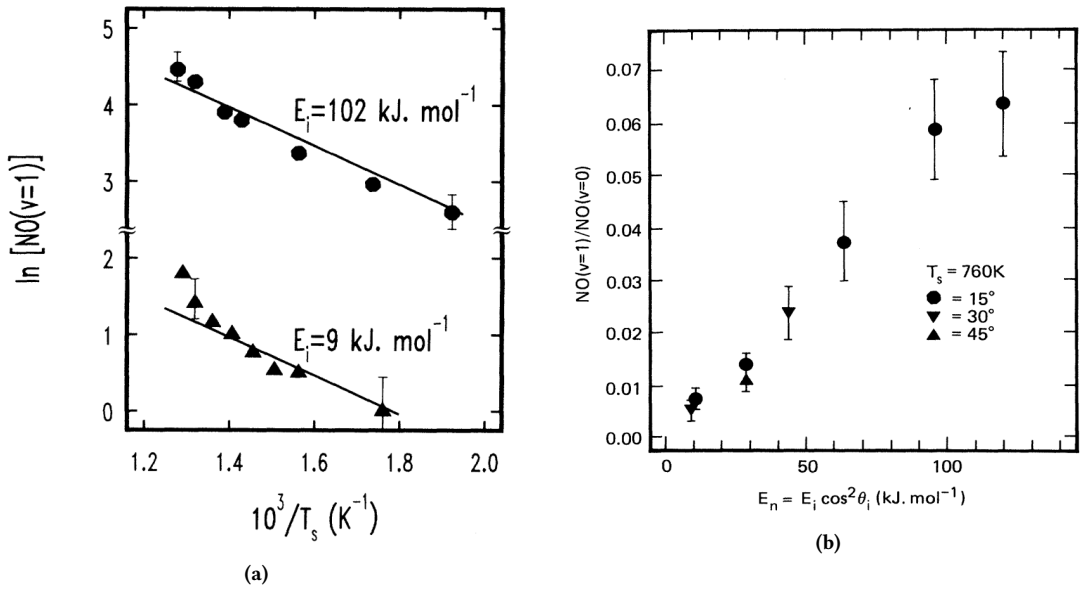

Figure 1.3: Vibrational excitation of NO scattered from Ag(111). (a) A strong surface temperature dependence of the excitation probability is observed. The solid lines represent an Arrhenius function with the energy fixed to the vibrational energy spacing in NO. (b) An increase in normal incidence translational energy also increases the vibrational excitation probability, but opposite to the NH_3/Au(111) system, no threshold is observed. Reprinted with permission from reference [28]. Copyright (1985) by the American Physical Society.

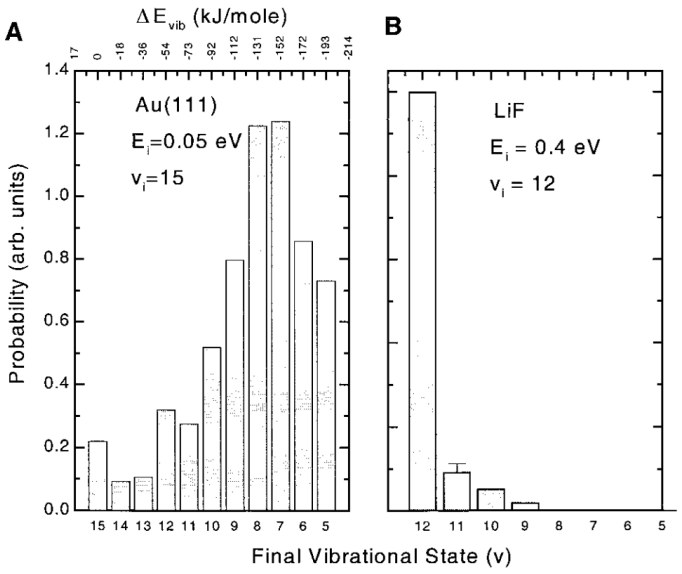

Figure 1.4: Vibrational state distributions for highly vibrationally excited NO scattered from Au(111) (left) and LiF (right). On the metal surface, the vibrational relaxation is mediated by an electron-hole-pair mechanism, leading to multiquantum vibrational relaxation. This interaction is not possible on an insulator as LiF, leading to barely any relaxation. Reprinted with permission from reference [29], Copyright (2000) by AAAS.

metals, such as gold. As a result, molecular motion is coupled to electronic motion, which leads to the breakdown of the Born-Oppenheimer approximation.[19,21,22,29]

Electronically, semiconductors are an intermediate between insulators and metals. Preliminary experiments of NO($v = 11$)/Ge(111) scattering have shown no significant vibrational relaxation, which is most likely caused by the band gap of 0.6 eV that inhibits any contribution of electrons in the conduction band.[32] This in turn makes graphene an interesting material for investigation. It is a semiconductor, but due to its special electronic structure, has a band gap of 0 eV,[33] which leads to the question, if non-adiabatic effects will play any role in the surface scattering dynamics of graphene.

Jiang *et al.*[34] scattered H- and D-atoms from graphene covered Pt(111) (Gr/Pt from here on) and found a fast and a slow component of the scattered atoms. The nearly elastically scattered component showed barely any energy loss, whereas a large loss of translational energy was observed if the incidence kinetic energy of the H-atoms was high enough, as shown in Figure 1.5. With the help of theoretical calculations, they were able to assign the fast component to a direct scattering of the atoms, and the slow component to a transient bond formation between the graphene and the D-atoms, in which one of the carbon atoms re-hybridizes and causes a puckering of the surface.[34] To form this transient bond, an activation barrier needs to be overcome. If the normal component of

the incidence kinetic energy is too low (panel (a) of Figure 1.5), then the atoms scatter on this barrier, leading to a low energy loss and an angular distribution that peaks at the specular angle. As soon as the normal kinetic energy is larger than the barrier, the slow component appears (panel (b) of Figure 1.5), because the atoms can cross the barrier, which leads to the formation of a transient bond that makes the energy transfer to the surface very efficient. If the incidence energy is increased even further (panel (c) of Figure 1.5), all atoms can cross the reaction barrier and the fast component vanishes.[34,35]

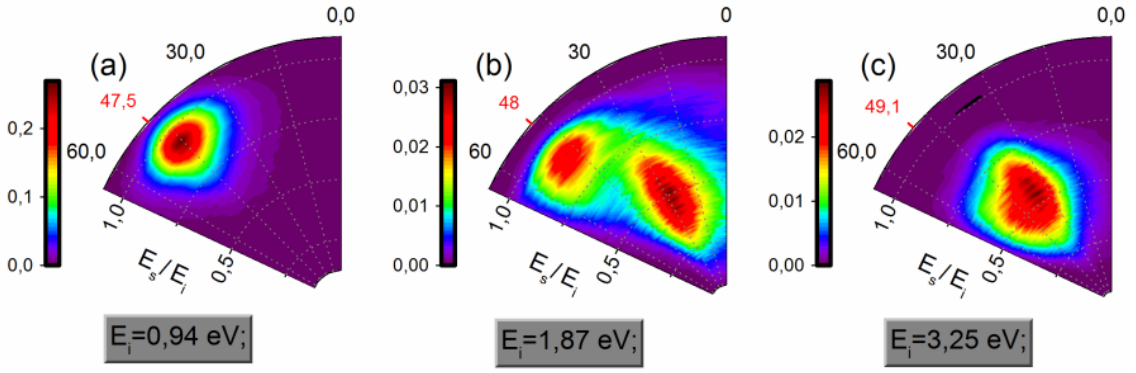

Figure 1.5: Final translational energy distributions as a function of the scattering angle for D-atoms scattered from Gr/Pt(111). The incidence angle is marked by the red tick. (a) For low translational energies, a specularly scattered component with very little energy loss is observed. (b) Increasing the kinetic energy of the D-atoms leads to the appearance of a new component with a high energy loss and a peak off the specular angle. (c) For even faster deuterium atoms, the specular component vanishes completely and only the slow component is observed. Theoretical calculations showed that a transient bond is formed between the D(H)-atoms and the graphene, if the incidence translational energy is large enough to overcome the reaction barrier, which results in the slow component. Taken from Reference [35] under Creative Commons Attribution Non-commercial Non-Derivative 4.0 International license (CC BY-NC-ND 4.0).

The work presented herein focuses on the scattering of nitric oxide (NO) from Gr/Pt and highly ordered pyrolytic graphite (HOPG) using molecular beam techniques. NO was chosen, because not only are its spectroscopic properties well known, but also easily reachable with table-top laser systems, making the detection and analysis of vibrationally and rotationally resolved spectra possible. As a result, a similar resolution to the H-atom scattering experiments is achievable. This makes nitric oxide a proxy for a possible reactand hitting the surface, with the possibility to investigate the interactions with a quantum state resolution. Similar to H-atoms, nitric oxide has an unpaired electron that could lead to possible bond formation on the surface. Platinum is used as the substrate, because the interaction of the graphene with the metal is very small and thus it can be considered as a model system for free-standing graphene.[36–38] On top of that, graphene on platinum can be easily synthesized inside the UHV apparatus using chemical

vapor deposition (CVD). Different mechanisms of vibrational excitation were observed for NO/Ag(111) and NH_3/Au(111) as discussed above, which leads to the following question: Is there vibrational excitation detectable in scattering NO from Gr/Pt and HOPG? If there is, temperature dependent studies can be used to probe for non-adiabatic behavior.

The comparison of Gr/Pt and HOPG might give insight into the effect the substrate has, as it can be seen as "graphene on platinum" vs. "graphene on graphite", even though the interaction of the graphene with the platinum is very small. Early experiments from Segner *et al.*[39] and Frenkel *et al.*[40] have shown that trapping of NO on graphite and "graphitized" platinum only occurs for surface temperatures below 400 K and for incidence angles larger than 30° at low kinetic energies (up to 210 meV). The sticking coefficient for an incidence angle of 60° as a function of the surface temperature is shown in Figure 1.6. Similar experiments of N_2 scattering from HOPG by Majumder *et al.*[41] and Mehta *et al.*[42] have shown a very strong dependence of the kinetic energy transfer between the molecule and the surface on the angle of incidence. All of the previously mentioned studies agree that trapping on graphite is highly unlikely for surface temperatures above 400 K and incidence angles close to the surface normal.

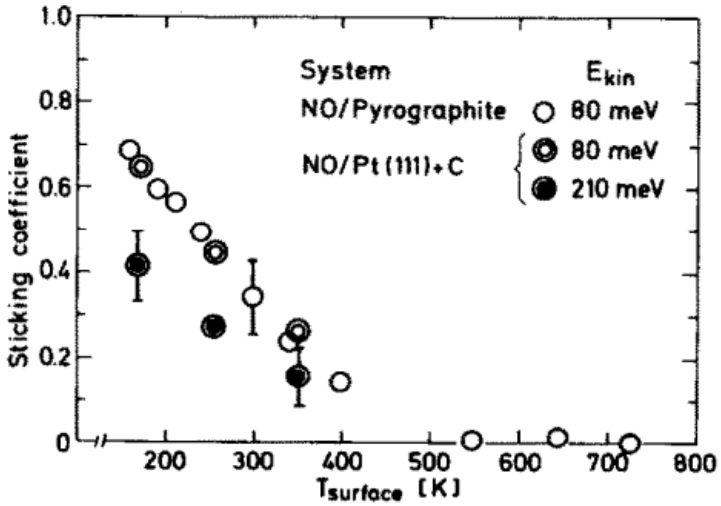

Figure 1.6: Sticking coefficient of NO on HOPG ("pyrographite") and "graphitized" platinum as a function of the surface temperature. All values for an incidence angle of 60°. Reprinted from Reference [39]. Copyright (1983), with permission from Elsevier.

More recently, Greenwood and Köhler investigated ground state NO scattering from graphene on Au(111) using molecular beam techniques at near normal incidence angle. They found no sign of trapping, even though the translational energy transfer of the NO to the surface is very efficient, with the NO losing up to 80% of the kinetic energy during the collision (see Figure 1.7). They were unable to model these results using molecular

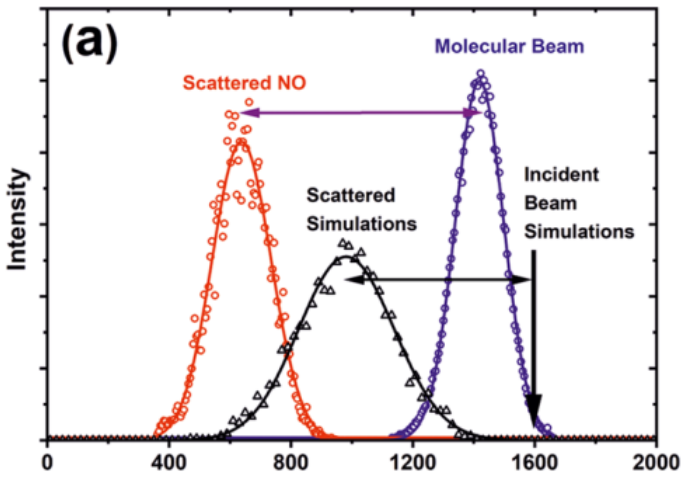

Figure 1.7: Speed distributions of the incidence (blue), scattered (red) and simulated scattered (black) beam of NO off of Gr/Au. The NO molecules lose around 80% of their kinetic energy in the experiment. The simulation underestimates the loss, predicting the loss of 60% translational energy. Adapted with permission from Reference [17]. Copyright (2021) American Chemical Society.

dynamics simulations. In preliminary experiments conducted before starting this work, the transfer of kinetic energy of NO to Gr/Pt was found to be of similar magnitude, but in contrast to the work of Greenwood, trapping seemed to play a non-negligible role in the scattering mechanism. Enhanced trapping on graphene would make it an interesting substrate for catalysts, that consists of active nanoparticles on a graphene substrate. The molecules could be ”caught” by the graphene and diffuse to the catalytically active sites to react and desorb. This leads to the next questions: Are the scattering dynamics between Gr/Pt and HOPG different? Does the nitric oxide trap on one surface, but not on the other? If yes, is the enhanced trapping caused by a difference in translational inelasticity?

Moreover, the experimental data produced for this thesis will improve the understanding of the interactions of NO with epitaxial graphene and can be used to test and improve theoretical methods. For example, current theoretical calculations of the binding energy of NO on freestanding graphene range from $-0.029\,\mathrm{eV}$ to $-2.4\,\mathrm{eV}$,[43–47] which is a sign that the theoretical methods cannot describe the interaction very well.

2 Theoretical Background

2.1 Graphene

Graphite consists of multiple stacked layers of graphene, which has been investigated for more than 75 years by now. In 1947, Wallace successfully calculated the electronic structure of graphene and was able to describe the zero-bandgap structure as well as the large difference in electrical conductivity parallel and perpendicular to the planes.[48] A long time after that, graphene was labeled an "academic" material, because free-standing 2D crystals (such as graphene) were thought to be thermodynamically unstable.[16] This changed drastically in 2004, when Andre Geim and Konstantin Novoselov were able to isolate monolayer graphene using mechanical exfoliation ("the scotch tape method"),[49] which led to them being awarded the Nobel prize of Physics in 2010.[50]

Lattice structure

The lattice structure and the first Brillouin zone of graphene are shown in Figure 2.1. The elementary cell consists of a rhombus and contains two carbon atoms A and B. In the reciprocal lattice, the center point of the first Brillouin zone is labeled Γ-point, the corners are labeled *K*-points and called Dirac points, and the middle between two neighboring Dirac points is called the *M*-point. The lattice vectors a_1 and a_2 are given by equation 2.1, where $a \approx 1.42\,\text{Å}$ is the C−C-bond length:

$$a_1 = \frac{a}{2}\left(3, \sqrt{3}\right), \quad a_2 = \frac{a}{2}\left(3, -\sqrt{3}\right). \tag{2.1}$$

The reciprocal lattice vectors b_1 and b_2 are given by equation 2.2:[33]

$$b_1 = \frac{2\pi}{3a}\left(1, \sqrt{3}\right), \quad b_2 = \frac{2\pi}{3a}\left(1, -\sqrt{3}\right) \tag{2.2}$$

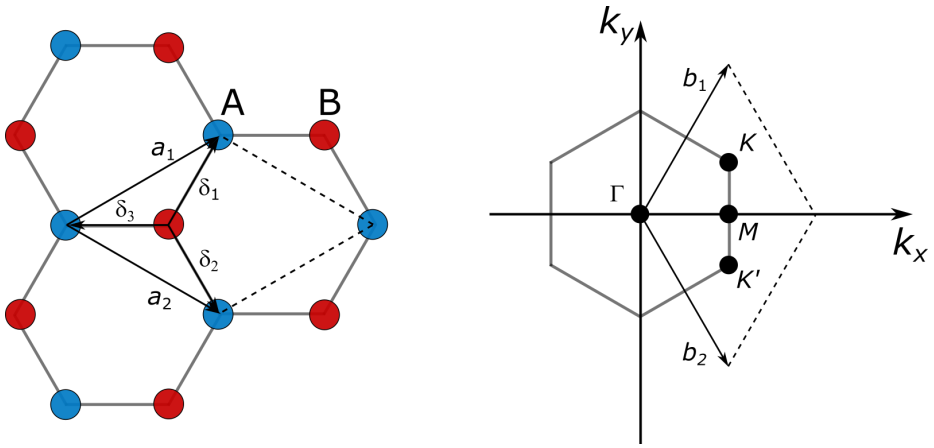

Figure 2.1: Left: Lattice structure of graphene, with the lattice unit vectors a_1 and a_2. δ_1, δ_2 and δ_3 are the nearest-neighbor vectors. Right: First Brillouin zone of graphene with the reciprocal lattice vectors b_1 and b_2. The dashed line indicates the complete elementary cell of graphene. The corner points are called Dirac points (K, K') and the middle point between them is called M-point, while the middle point of the first Brillouin zone is labeled Γ-point. Adapted from reference [33] and modified.

The nearest neighbor vectors δ_i in real space are given by equation 2.3 and the location of the Dirac points in momentum space is given by equation 2.4.[33]

$$\delta_1 = \frac{a}{2}\left(1, \sqrt{3}\right), \quad \delta_2 = \frac{a}{2}\left(1, -\sqrt{3}\right), \quad \delta_1 = -a(1, 0) \tag{2.3}$$

$$K = \left(\frac{2\pi}{3a}, \frac{2\pi}{3\sqrt{3}a}\right), \quad K' = \left(\frac{2\pi}{3a}, -\frac{2\pi}{3\sqrt{3}a}\right) \tag{2.4}$$

Electronic structure

The electronic structure of freestanding graphene is shown in Figure 2.2, based on calculations using the tight binding approximation.[33] The image shows the valence and conduction band in the lower and upper part of the graph, respectively. The unusual electronic properties of graphene are caused by the dispersion around the Dirac points, which is shown in the right part of the same figure. The Fermi energy (for freestanding graphene) is located at the Dirac points and within 1 eV of them, the dispersion is linear, and can be described by Equation 2.5.

$$E_{\pm}(k) \approx \pm \hbar v_F |k - K| \tag{2.5}$$

Here, $\hbar$ is the reduced Plank's constant, v_F the Fermi frequency, K the wave vector for the Dirac point, k that of the carrier, and $E_{\pm}(k)$ the energy of the valence and conduction bands.[35] This dispersion relation resembles that of light, meaning that charge carriers can be better described using a 2D analog (Equiation 2.8) of the Dirac equation (Equation 2.7) instead of the Schrödinger equation (with an effective mass m^*, Equation 2.6), which is usually used to describe charge carriers in condensed matter physics.[3,51]

$$\hat{H} = \hat{p}^2/2m^* \tag{2.6}$$

$$\hat{H} = c\vec{\sigma} \cdot \hat{p} \tag{2.7}$$

$$\hat{H} = v_F \vec{\sigma} \cdot \hat{p} \tag{2.8}$$

The charge carriers are treated as massless Dirac fermions, the speed of light c is replaced by the Fermi velocity v_F with $v_F \approx 10^6$ m/s and a 2D pseudospin matrix takes the roll of the Pauli matrix $\vec{\sigma}$.[3] $\hat{p}$ is the momentum operator.

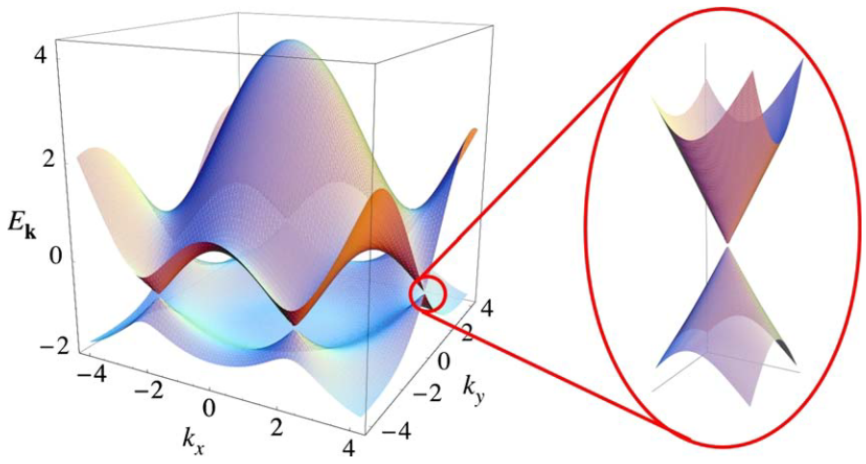

Figure 2.2: Left: Calculated electronic dispersion of freestanding graphene. The lower part is the valence band, and the upper part the conduction band. Both bands meet at the Dirac points, which leads to the zero bandgap structure. Right: close view on the linear dispersion near one of the Dirac points. Reprinted with permission from reference [33], Copyright (2009) by the American Physical Society.

Epitaxial graphene on transition metals

Mechanical exfoliation is not the only method to produce high quality graphene. Epitaxial growth of graphene on different transition metal surfaces such as Pt(111), Ni(111), Ru(0001), Ir(111), Rh(111), Pd(111), Re(0001), Cu(111), Co(0001)[52] using chemical vapor deposition (CVD) has also gained a lot of popularity. Growing an overlayer of carbon on

platinum for example has been used to passivate the surface in early scattering experiments,[39] but did not result in the growth of an ordered layer of graphene on the surface, because the growth conditions were not right. When growing graphene on a transition

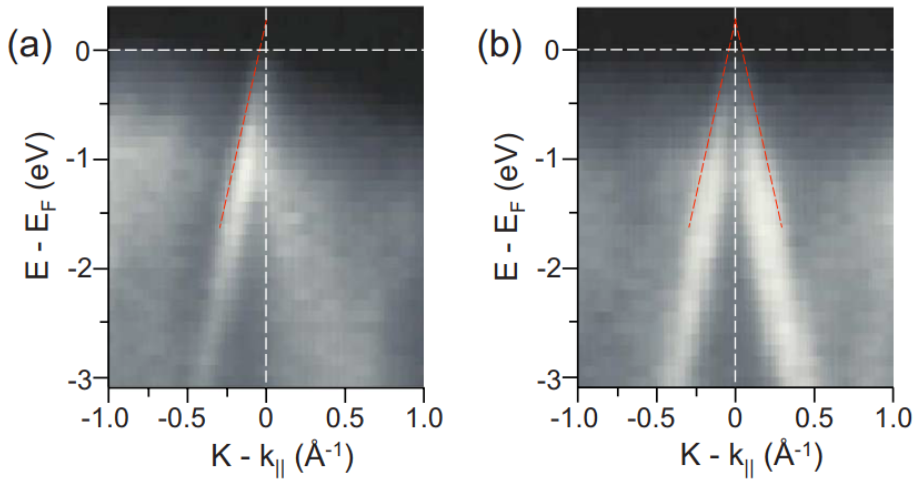

Figure 2.3: Micro-ARPES measurements of Gr/Pt(111) near the K-point along the Γ-K direction (a) and perpendicular to the Γ-K direction (b). The slope of the red line indicates a Fermi velocity of 10^6 m/s and is a guide to the eye. Reprinted with permission from reference [38], Copyright (2009) by the American Physical Society.

metal, there are three types of graphene that can be achieved:[52] First, for a low mismatch between the graphene and substrate lattice constant and low interaction, a very flat and quasi-freestanding layer of graphene is achieved, which is the case for Pt and Ir. For high interaction systems such as Ru, Re, Pd, and Rh, the graphene is strongly rippled. Third, for Ni and Co the lattice mismatch is negligible, which results in strong hybridization between the *d*-bands of the metal and the π-bands of graphene, creating a chemisorbed graphene layer with very small distances to the substrate (2.1 Å for Ni and $1.5 - 2.2$ Å for Co).[52]

The addition of a substrate to the graphene, even if it's one with low interaction such as platinum, causes changes in the electronic structure that has been discussed above. Figure 2.3 shows micro-ARPES spectra near the Dirac point of epitaxial graphene grown on Pt(111). As indicated by the red lines (a guide to the eye), the Dirac cones don't meet at the Fermi level, as they do for freestanding graphene, but about 0.3 eV above, meaning that the graphene is slightly p-doped on platinum.[38]

Phonon dispersion

Figure 2.4 shows the phonon dispersion along the $\overline{\Gamma}$ to $\overline{K}$ direction of graphene measured by high resolution electron energy loss (HREELS) spectra. In Figure 2.4 a, three different substrates are compared, one of each of the previously mentioned categories. Note that most phonon modes for Gr/Ni and Gr/Ru are softened with respect to Gr/Pt, either due to strong interaction with the substrate or due to corrugation.[52] Figure 2.4 b shows a

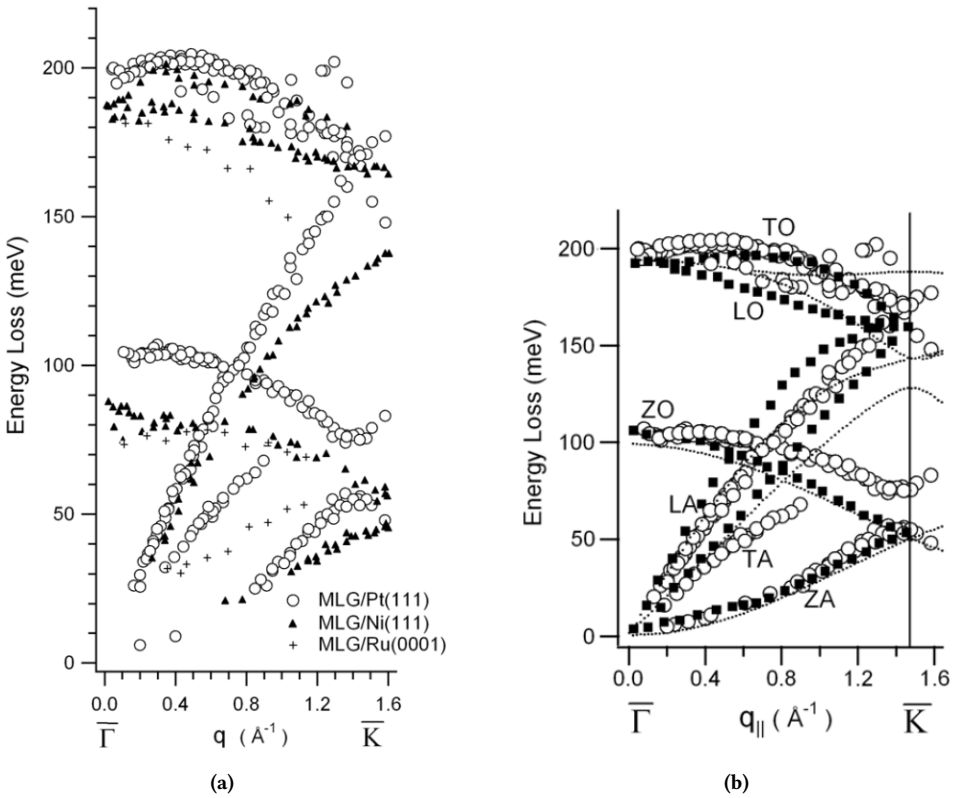

Figure 2.4: (a) Phonon dispersion along the $\overline{\Gamma} - \overline{K}$ of the Brillouin zone of monolayer graphene (MLG) on three different substrates. The phonon modes are softened when Nickel and Ruthenium are used as substrates compared to Platinum. (b) Phonon dispersion along the $\overline{\Gamma} - \overline{K}$ of the Brillouin zone for Gr/Pt(111) (open circles), bulk graphite (filled squares, from calculations), and free standing graphene (dotted curve, from calculations). Note that the phonons of Gr/Pt are nearly identical to those of graphite. Reprinted with permission from reference [52]. Copyright (2012) IOP Publishing, Ltd.

comparison of the phonon dispersion of Gr/Pt(111), graphite and freestanding graphene. The differences between graphene and graphite are very small, except for the degeneracy of the out-of-plane optical (ZO) and acoustical (ZA) phonons at the $\overline{K}$-point which is present for graphite and freestanding graphene but lifted for Gr/Pt(111). The addition of a substrate causes a symmetry reduction in the graphene, as some carbon atoms sit atop a substrate atom and some in a three-fold site, resulting in the lifted degeneracy of the

ZA/ZO modes at the $\overline{K}$-point.[52]

Structure of epitaxial graphene

As this work focuses on graphene epitaxially grown on Pt(111), this part will briefly discuss the structure of the surface. Gr/Pt was chosen due to the low interaction with the substrate as well as very flat surface, resembling quasi-freestanding graphene. Also, the distance between the graphene and the platinum is 3.31 Å,[37,52] which is very close to the interlayer distance in graphite (3.34 Å).[53] Depending on the growth conditions, mainly the substrate temperature, different rotational domains of the graphene lattice will dominate. LEED images for three different growth temperatures are shown in Figure 2.5, and the angle noted in the LEED patterns specifies the orientation of the graphene lattice with respect to the platinum substrate. The 19° domain has been used in the experiments conducted during this work, see Figure 3.13.

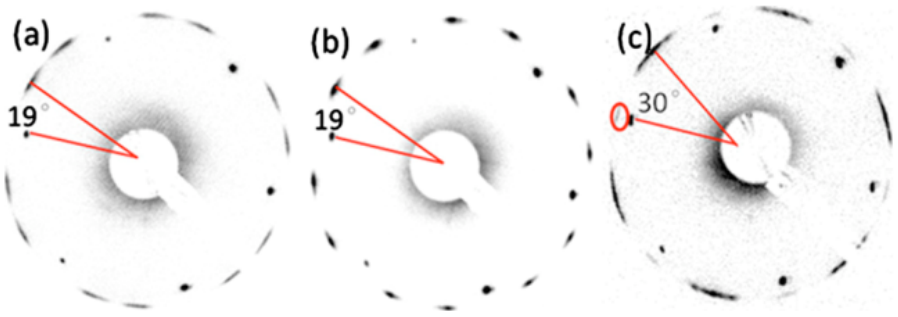

Figure 2.5: LEED patterns of two different orientations of graphene. Angles are given with respect to the platinum substrate. Graphene grown via CVD of ethylene at increasing temperatures: (a) 773 K,(b) 873 K, and (c) 973 K. The 19° domain is the one used for the experiments in this thesis, see Figure 3.13. Reprinted with permission from reference [54]. Copyright (2011) by the American Institute of Physics..

Changing the substrate temperature and amount of ethylene used during the growth process not only changes the dominant rotational domain, but also the size of the individual domains, as can be seen in Figure 2.6.[54] The left side (a) of the image shows graphene grown at $T_S = 1073$ K with an exposure of 376 L. The high surface temperature in combination with the abundance of gas causes a high amount of nucleation sites, which results in tiny graphene domains with barely any preferred orientation. The differences are straighforward, when comparing this to the right side (b) of Figure 2.6, which shows graphene grown at $T_S = 773$ K with an exposure of 37.6 L. Using these conditions, the low nucleation rate causes growth of graphene domains of a few tens of nanometers in

diameter, which is more desirable for surface scattering experiments, because it results in a more homogenous surface.[35,54]

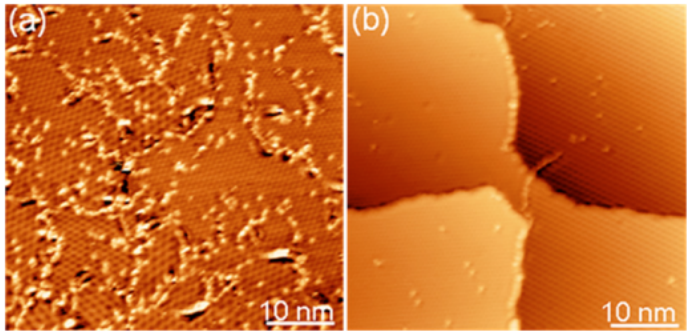

Figure 2.6: Domain size of graphene for two different growth conditions: (a) 1073 K, 376 L, (b) 773 K, 37.6 L. Higher growth temperatures lead to smaller domain sizes due to an increased rate of nucleation on the surface. Reprinted with permission from reference [54]. Copyright (2011) by the American Institute of Physics.

As mentioned before, the 19° domain is preferred for this work, which has a 3×3 Moiré super structure. Figure 2.7 shows atomically resolved STM images of the graphene surface for different rotaional orientations. The yellow arrow indicates the lattice vector of graphene and the green rhombus the unit cell of the Moiré pattern. Panels (g) and (h) show the height profiles.[54] The low interaction between the graphene and the platinum causes a very flat height profile.

2.2 Molecule-surface scattering

In a non-reactive gas-surface collision, a few basic things can happen – the molecule bounces back directly, it sticks to the surface or dissociates at the surface.[55] These scattering channels are called direct scattering, trapping-desorption and dissociative adsorption, respectively, and are not mutually exclusive. They are illustrated in Figure 2.8. For example, when Frenkel and co-workers investigated NO scattering from graphite,[40] they saw that the angular distribution consists of two components (see Figure 2.9). They observed a narrow component that peaks at the specular angle, as well as a broad component with a cosine shaped distribution.

Direct scattering

The component with a narrow angular distribution that peaks around the specular angle is caused by direct scattering. The interaction time with the surface is very short

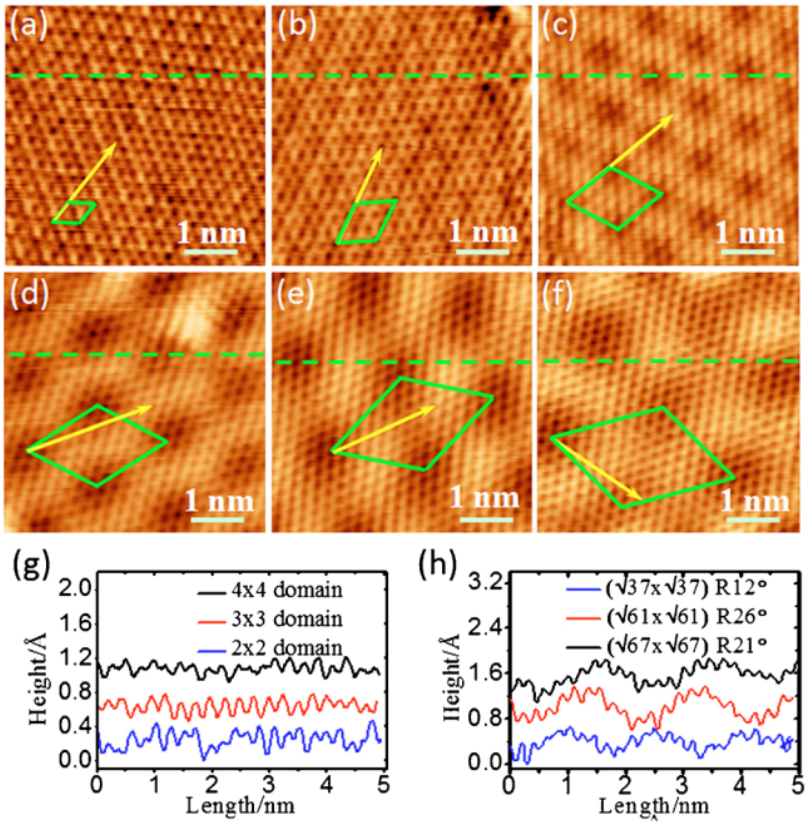

Figure 2.7: STM images of different rotational domains, that lead to different Moiré supercells. The yellow arrows show the lattice vector of graphene and the green boxes the moiré unit cells. The rotation angle between the graphene and the platinum lattice is given in parentheses. (a) 2×2 (30°), (b) 3×3 (19°), (c) 4×4 (14°), (d) $(\sqrt{37} \times \sqrt{37})$ R21° (6°), (e) $(\sqrt{61} \times \sqrt{61})$ R26° (3°), (d) $(\sqrt{67} \times \sqrt{67})$ R12° (2°). The height profiles along the dashed green lines are shown in (g) and (h). Reprinted with permission from reference [54]. Copyright (2011) by the American Institute of Physics.

(<1 ps)[57] for direct scattering, hence the molecular degrees of freedom cannot equilibrate completely with the surface. As a result, the distribution of energy across the degrees of freedom of the molecule strongly depends on the incidence conditions and less on the temperature of the surface. Consequently, a rotational temperature independent of the surface temperature is often observed.[55]

The interaction of the gas molecules (or atoms) with the surface can either be purely mechanical (adiabatic) or show signs of non-adiabatic effects. The excitation of the vibrational umbrella mode of NH_3 scattered from Au(111) is a good example for an adiabatic direct scattering. Excitation of the umbrella mode is only visible if the incidence translational energy exceeds the energy of the vibration, because the kinetic energy is converted to vibrational energy during the collision.[27] The vibrational excitation probability is independent of the surface temperature, as shown in Figure 1.2. On the other hand, vi-

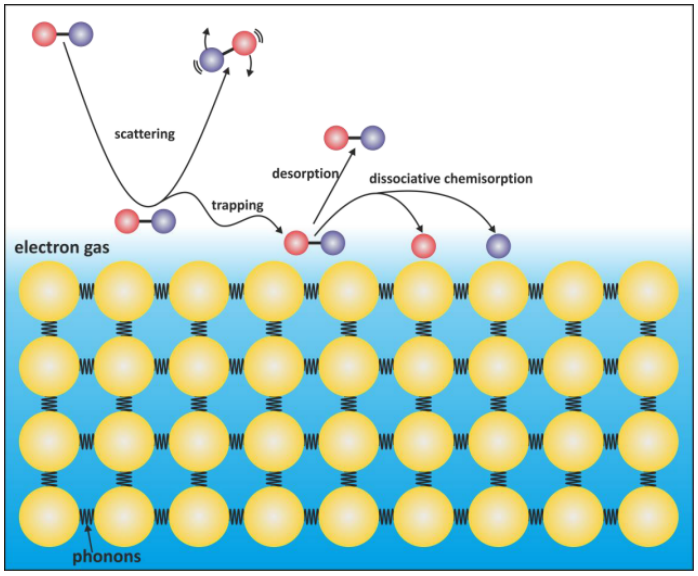

Figure 2.8: Illustration of the possible interactions of molecules with surfaces. Taken from Reference [56] under Creative Commons Attribution Non-commercial Non-Derivative 4.0 International license (CC BY-NC-ND 4.0).

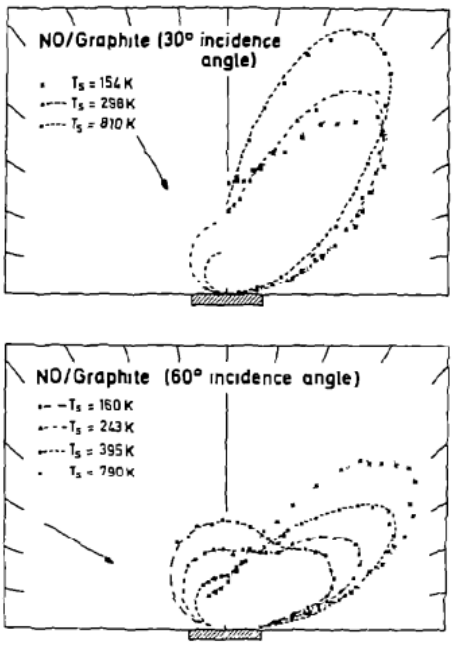

Figure 2.9: Angular distributions for NO scattered from graphite for different surface temperatures and an incidence angle of 30° (top) and 60° (bottom). Reprinted from Reference [40]. Copyright (1982), with permission from Elsevier.

brational excitation of NO during the collision with a Ag(111) surface is a good example for non-adiabatic interactions. Figure 1.3 shows the population of NO($v = 1$) as a function of the incidence kinetic energy as well as the surface temperature. The vibrational excitation probability strongly depends on the surface temperature and increases with increasing kinetic energy, but does not show a similar threshold-behavior as NH_3/Au(111). The vibrational excitation was assigned to interaction of the molecular vibration with thermally excited electron-hole pairs in the surface, which results in the strong surface temperature dependence of the excitation probability.[28]

In a very simple mechanical picture, the collision of a gas particle with a surface can be described by the collision of two hard spheres of masses m (gas particle) and M (mass of a surface atom), which was modeled in 1914 by B. Baule.[58] The dependence of the final translational energy E_f on the incidence energy E_i can be described by Equation 2.9:

$$E_\mathrm{f} = \left(\frac{m - M}{M + m}\right)^2 E_\mathrm{i} \tag{2.9}$$

Even though this model is very simple and doesn't take attractive forces between the surface and the molecule or effects of the surface temperature into account, it can be used to describe the translational inelasticity of molecules surface scattering. For example, Golibrzuch *et al.* investigated the vibrationally elastic scattering of NO($v = 3$) from Au(111).[59] They found that the translational energy loss during the collision is described well by the Baule limit with the surface mass of one gold atom, which is shown in Figure 2.10.

Trapping-desorption

The second component of the angular distributions shown in Figure 2.9 is broad, near cosine-shaped with the peak near the surface normal and is caused by trapping-desorption. For trapping desorption, the interaction time between the surface and the molecules is >1 ps.[57] The interaction time τ can be estimated using Equation 2.10:

$$\tau = \nu^{-1} \exp\left(-\frac{E_\mathrm{ads}}{k_\mathrm{B} T_\mathrm{S}}\right), \tag{2.10}$$

where T_S is the surface temperature, E_ads is the adsorption energy of the molecule at the surface, and a good estimate for the frequency factor ν is $10^{13}\,\mathrm{s}^{-1}$.[40] For the current example of NO scattered from graphite, this results in interaction times of $\tau \approx 1\,\mathrm{ns}$ for $T_\mathrm{S} = 150\,\mathrm{K}$ and $\tau \approx 1\,\mathrm{ps}$ for $T_\mathrm{S} = 700\,\mathrm{K}$, which is why the broad cosine-part of the angular

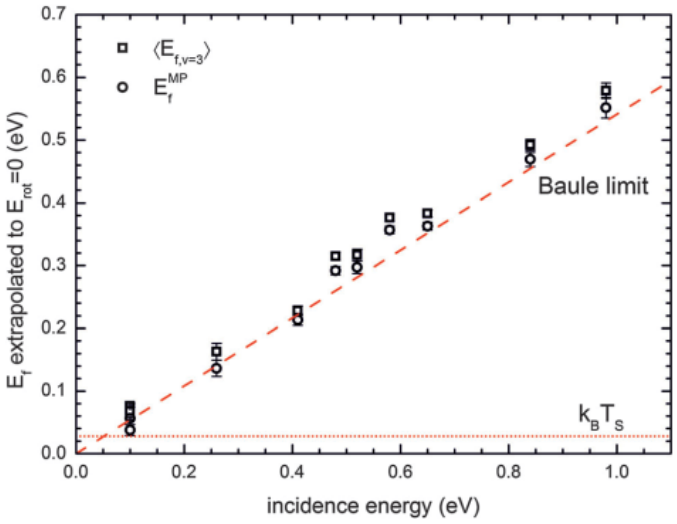

Figure 2.10: The final kinetic energy of vibrationally elastically scattered NO($v = 3$) from a Au(111) surface at $T_S = 320$ K. The measured data agrees well with the kinetic energy predicted by the Baule-model (dashed line). The thermal energy of the surface is indicated by the dotted line. Taken from Reference [59] under Creative Commons Attribution 3.0 unported License (CC-BY 3.0).

distributions vanishes at high surface temperatures.

For trapping desorption (and in contrast to direct scattering), the surface temperature has a very strong influence on the interaction as well as the energy distribution within the molecule. The interaction times in trapping desorption are long enough for the molecules to reach thermal equilibrium with the surface. Hence, the translational, rotational and vibrational distributions of molecules undergoing trapping-desorption can be described well with thermal Maxwell-Boltzmann-distributions fixed at the surface temperature,[55,60] and do not depend strongly on the incidence conditions. The angular distribution is also expected to be cosine-shaped, because the molecules desorb in random directions. Note however, that while the incidence translational energy doesn't affect the energy in the internal degrees of freedom, it does affect the sticking probability and thus the chance of trapping-desorption to occur. An illustration of two different trapping-desorption cases is shown in Figure 2.11. In the upper panel, an adsorption barrier is present. As a result, only molecules with enough kinetic energy to cross the barrier will stick (upper arrow), slow molecules will scatter directly on the barrier (lower arrow). The opposite is the case for the lower panel, where no adsorption barrier is present. In this case, only those molecules that can dissipate enough energy during the collision will stick (lower arrow). If the kinetic energy after the scattering is still larger than the adsorption well, the molecules will scatter directly (upper arrow).[60] On the other hand, vibrational

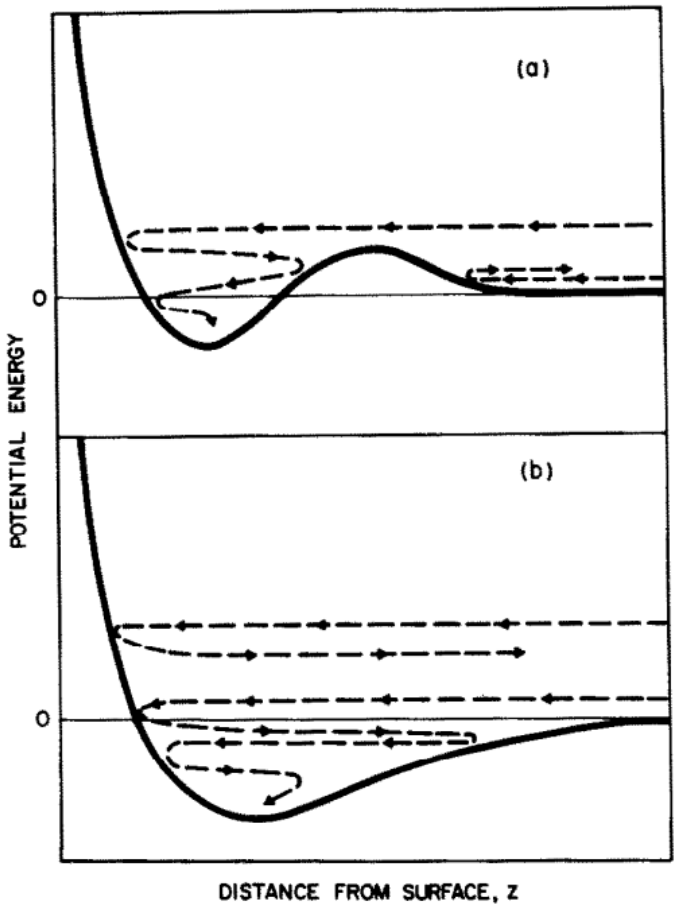

Figure 2.11: Schematic picture of two different trapping-desorption mechanism. (a) If an adsorption barrier is present, molecules with a translational energy larger than the barrier will adsorb. Molecules with insufficient kinetic energy will scatter on the barrier. (b) For an adsorption without a barrier, molecules will scatter directly, if they cannot dissipate enough energy during the collision. As a result, slow molecules are more likely to stick. Kinetic energy distributions for both cases can be understood in the picture of detailed balance, which is explained in detail in section 2.3. Reprinted from Reference [60]. Copyright (1981), with permission from Elsevier.

excitation of the molecule prior to the collision does not affect the trapping probability, but it does enhance the chance for dissociative adsorption.[24] The changes in trapping probability with changing incidence energy can be explained using the concept of *detailed balance*, which will be discussed in the next section.

2.3 Detailed balance

The concept of *detailed balance* is a generalization of the *principle of microscopic reversibility* that was first introduced by Tolman in the mid 1920s.[61,62] The principle of microscopic reversibility states that for every molecule leaving state A via a particular path,

another molecule has to enter state A via the reverse path in unit time, if the system is in equilibrium. No cyclic processes are allowed, only direct transitions between the two states. If this were not the case, the system would leave equilibrium. Note however that the principle of microscopic reversibility is only valid for a single microscopic step.[1] In 1929, Fowler expanded this concept from a single to all microscopic steps in a system, making it applicable to macroscopic systems and called it *the principle of detailed balance.*[64] Applying this concept to a gas-surface interaction under equilibrium conditions, the flux of molecules impinging on the surface f_{in} must be balanced by an equal but opposite flux of molecules leaving the surface f_{out} to maintain equilibrium:[65]

$$f_{\mathrm{in}}(v, \theta, \phi; T, p) = f_{\mathrm{out}}(v, \theta, \phi; T, p). \tag{2.11}$$

Here, v is the speed of the molecules, θ and ϕ are the angles between the surface and the surface normal and the azimuthal angle, respectively, and T and p are the temperature and pressure describing the thermodynamic state of the system. If multiple interactions of the molecules with the surface are possible, e. g. an equilibrated and a non-equilibrated component, it is important that they are clearly distinguishable, and that the non-equilibrated component leaves the surface chemically unchanged.[2] [64,65] Then, the flux impinging and leaving the surface can be written as

$$f_{\mathrm{in}} = \Gamma + \Gamma^* \quad \text{and} \quad f_{\mathrm{out}} = R + R^*, \tag{2.12}$$

where the non-equilibrated component is marked with the asterisk. The equilibration probabilities for the incoming $P_{\mathrm{eq,in}}$ and outgoing molecules $P_{\mathrm{eq,out}}$ can then be written as

$$P_{\mathrm{eq,in}} = \frac{\Gamma}{f_{\mathrm{in}}} \quad \text{and} \quad P_{\mathrm{eq,out}} = \frac{R}{f_{\mathrm{out}}}. \tag{2.13}$$

To keep the equilibrium at the surface, the differential rate of adsorption has to equal the differential rate of desorption

$$\Gamma = R, \tag{2.14}$$

[1] The author later stated that the name *principle of microscopic reversibility* was not "appropriately descriptive". [63]

[2] These conditions are for example not fulfilled for an Eley-Rideal type reaction, where one component is supplied directly from the gas phase. [65]

which leads to the necessary requirements[65] that

$$P_{\mathrm{eq,in}} = P_{\mathrm{eq,out}} = P_{\mathrm{eq}} \quad \text{and} \quad \Gamma^* = R^*. \tag{2.15}$$

In other words, detailed balancing is the mechanism that maintains the steady-state properties of a system in equlibrium.

For gas-surface interactions with no barrier, P_{eq} is only dependent on the probability of the impinging molecule to lose enough translational energy and often described by a sticking (or trapping) function $S_{\mathrm{trap}}[E, \cos(\theta)]$.[66] Since the molecules only need to lose the energy perpendicular to the surface, the angle of incidence also plays an important role in the sticking probability.

One example for a no barrier adsorption of atoms is Ar scattering from a 2H-W(100) surface[67], where a sub-thermal speed distribution of the desorbing molecules was observed (see Figure 2.12). Applying detailed balance arguments to these results gives a sticking coefficient that decreases with increasing incidence translational energy, as shown in Figure 2.12 a. The product of this sticking function and a thermal Maxwell-Boltzmann distribution at surface temperature (top panel of Figure 2.12 b) describes the experimental results very well (bottom panel of the same figure).

Recombinative desorption of H_2 or D_2 from copper[23,68–70] or gold[71] shows the opposite behavior, where the sticking probability increases with increasing incidence translational energy, starting at a certain threshold (see Figure 2.13 for the resulting sticking function of H_2 on Cu(111)), and results in hyper-thermal speed distributions of the trapped component. A comparison of a molecular beam study with a study of the desorption after diffusion through a copper crystal revealed the same hyper-thermal speed as well as highly peaked angular distributions. The angular distributions in the molecular beam study were also independent of the incidence angle and kinetic energy, although S_{trap} was strongly dependent on both.[68] These results can again be explained using the concept of detailed balancing. If the molecules have sufficient translational energy to overcome the adsorption barrier, they will stick to the surface, otherwise they scatter back directly. Figure 2.13 also shows the sticking function for different vibrational states, and the kinetic energy required for dissociative adsorption decreases with increasing vibrational excitation, because the bond-stretching during the vibrational motion is part of the dissociation pathway.[24,70]

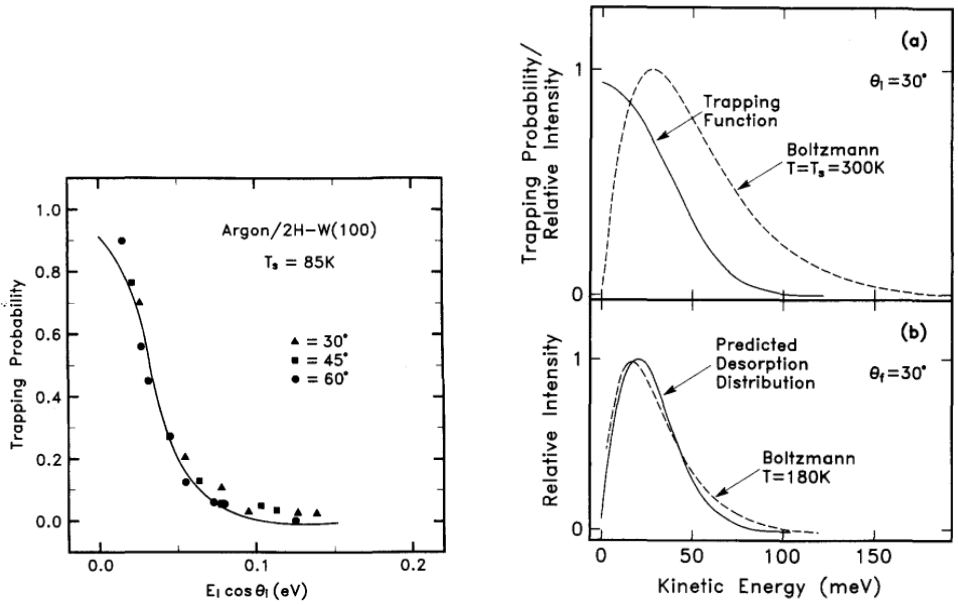

Figure 2.12: (a) Trapping probability of Ar on a 2H-W(100) surface as a function of incidence energy and angle. (b) The product of the trapping function and a thermal Maxwell-Boltzmann distribution fixed at the surface temperature (upper panel) agrees well with the observed subthermal speed distribution (lower panel). Reprinted with permission from reference [67]. Copyright (1989) by the American Institute of Physics.

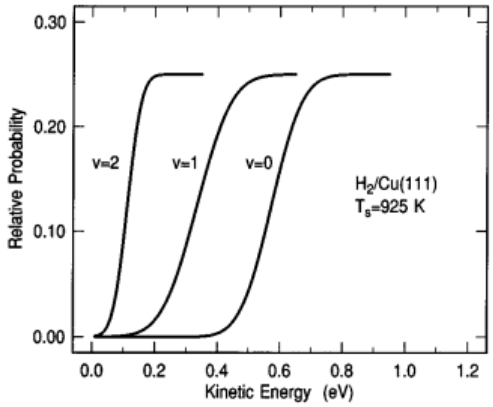

Figure 2.13: Sticking probability as a function of incidence kinetic energy for the direct dissociative adsorption of H_2 on a Cu(111) surface. The kinetic energy required for sticking decreases with increasing vibrational excitation, because vibrational motion weakens the bond and thus reduces the barrier for dissociation. Reprinted with permission from reference [23]. Copyright (1995) by the American Institute of Physics.

2.4 Spectroscopy of nitric oxide

Throughout the years of spectroscopic studies conducted on nitric oxide, a lot of electronic states have been observed and investigated.[72] For this work, the electronic ground state $X^2\Pi_\Omega$ and the first electronically excited state $A^2\Sigma^+$ state are of interest. Transitions between these two states form the γ-band system (see Fig. 2.14), which can be used for quantum state specific detection of NO using a 1+1 REMPI scheme. Most of the relevant transitions of the γ-band can be reached with relative ease, because wavelengths between 220 nm − 250 nm are needed and can be produced by commercially available table top laser systems. The detection method will be explained in detail in chapter 3.2.1, while this section will briefly discuss the two relevant electronic states, based on references [32, 73–76].

The electronic ground state $X^2\Pi_\Omega$

An effective Hamiltonian for a $^2\Pi$ state of a diatomic molecule can be written as

$$H = H_0 + V \quad \text{with} \quad V = H_{\text{SO}} + H_{\text{Rot}} + H_{\text{SR}}, \tag{2.16}$$

where the vibronic energies are given by the eigenvalues of H_0 and the perturbation Hamiltonian V describes the fine structure. H_{SO} is the spin-orbit Hamiltonian, H_{Rot} the rotational Hamiltonian, and H_{SR} the spin-rotation Hamiltonian, defined by

$$H_{\text{SO}} = A\mathbf{L}\cdot\mathbf{S} \tag{2.17}$$

$$H_{\text{rot}} = B\mathbf{R}^2 \tag{2.18}$$

$$H_{\text{SR}} = \gamma\mathbf{R}\cdot\mathbf{S}, \tag{2.19}$$

with $\mathbf{R} = \mathbf{J}-\mathbf{L}-\mathbf{S}$, where $\mathbf{J}$, $\mathbf{L}$, and $\mathbf{S}$ are the quantum numbers for total angular momentum, orbital angular momentum and spin, respectively.[73] The values for the spectroscopic constants A, B, and γ are listed in References [73] and [77].

The wave functions are given for the Hund's case (a)[78] basis, which is valid for low J-states up to $J \approx 35.5$ in the X-state[79] by

$$|JM\Omega_\epsilon\rangle = \frac{1}{\sqrt{2}}\left(|JM+\Omega\rangle + \epsilon|JM-\Omega\rangle\right). \tag{2.20}$$

M is the projection of the angular momentum on a lab frame axis and Ω is the projection of J onto the internuclear axis. The parity ϵ can take values of ±1 and is related to the

total parity (+/−) via $(-1)^{J-\epsilon/2}$.

The Hamiltonian can then be written as a 2×2 matrix for each parity state:

$$H_\epsilon = \begin{pmatrix} H_{11,\epsilon,\Omega=3/2} & H_{12,\epsilon} \\ H_{21,\epsilon} & H_{22,\epsilon,\Omega=1/2} \end{pmatrix}, \tag{2.21}$$

and the relation of the matrix elements and the spectroscopic constants in cm^{-1} is given by equations 2.22, 2.23, and 2.24. z is used to improve the readability of the equations and is defined as $z = (J - 0.5)(J + 0.5)$.

$$\begin{aligned} H_{11,\epsilon} =& hc(T_0 + W + 0.5A + 0.5A_D \cdot z \\ &+ B \cdot z - D \cdot z(z+1) + H \cdot z(z+1)(z+2)) \end{aligned} \tag{2.22}$$

$$\begin{aligned} H_{22,\epsilon} =& hc(T_0 + W - 0.5A - 0.5A_D \cdot (z+2) \\ &+ B \cdot (z+2) - D \cdot (z+1)(z+4) + H \cdot (z+1)(z^2+8z+8) \\ &- 0.5\epsilon \cdot p_\Lambda \cdot (J+0.5) - \epsilon \cdot q_\Lambda \cdot (J+0.5)) \end{aligned} \tag{2.23}$$

$$\begin{aligned} H_{12,\epsilon} =& hc(-B\sqrt{z} + 2D\sqrt{z} \cdot (z+1) - H\sqrt{z} \cdot (z+1)(3z+4) \\ &+ 0.5\epsilon \cdot q_\Lambda \cdot \sqrt{z} \cdot (J+0.5)) \end{aligned} \tag{2.24}$$

Here, T_0 is the electronic and W the vibrational term energy, and B, D and H are rotational constants. The spin-orbit splitting is described by A and A_D and the Λ-doubling by q_Λ and p_Λ. The latter is stronger for the $\Omega = 0.5$ state and is commonly attributed to interaction with $^2\Sigma^-$ states.

The first electronically excited state $\mathrm{A}^2\Sigma^+$

To simplify the calculation of the transitions, the quantum number J is used for the A-state instead of the more appropriate choice of pure nuclear rotational motion N. Being a $^2\Sigma$ state, the A-state is best described using Hund's case (b)[78] and equations 2.25 and 2.26 can be used to calculate the term energies for the e and f parity states, respectively.

$$\begin{aligned} H_e =& hc(T_A + W_A + B_A \cdot (J-0.5)(J+0.5) \\ &- D_A \cdot (J-0.5)^2(J+0.5)^2 + 0.5\gamma_A(J-0.5)) \end{aligned} \tag{2.25}$$

$$\begin{aligned} H_f =& hc(T_A + W_A + B_A \cdot (J-0.5)(J+0.5) \\ & - D_A \cdot (J-0.5)^2(J+0.5)^2 - 0.5\gamma_A(J-0.5)) \end{aligned} \tag{2.26}$$

The spin-rotation interaction is characterized by the spin splitting constant γ_A, and all other constants are labeled similar to the ones describing the X-state, except they now depend on the vibrational level v_A of the A-state and thus are marked with the index A.

Transitions of the γ-band

The selection rules are listed in equations 2.27–2.30. Taking these into account, especially eq. 2.30, 12 rotational branches can appear for a vibrational band in the γ-band system, because only transitions between different parity states are allowed.

$$\Delta J = 0, \pm 1 \tag{2.27}$$

$$\Delta \Lambda = 0, \pm 1 \tag{2.28}$$

$$\Delta S = 0 \tag{2.29}$$

$$+ \leftrightarrow -, + \nleftrightarrow +, - \nleftrightarrow - \tag{2.30}$$

Equation 2.27 results in the P,Q and R-branches for $\Delta J = -1, 0, +1$. All twelve rotational transitions are shown in Figure 2.14 and they are labeled using the spin labels F1 and F2 according to $\Delta J_{F''F'}$. The spin rotation interaction γ_A in the A-state causes a small splitting between F1 and F2, whereas for the X-state, all F1 states belong to $\Omega = 0.5$ and all F2 states to $\Omega = 1.5$ due to spin-orbit coupling.

Based on these selection rules, a MATHEMATICA notebook was written in the Wodtke group,[80] which was used in this work for the assignment and simulation of REMPI spectra of the γ-band.

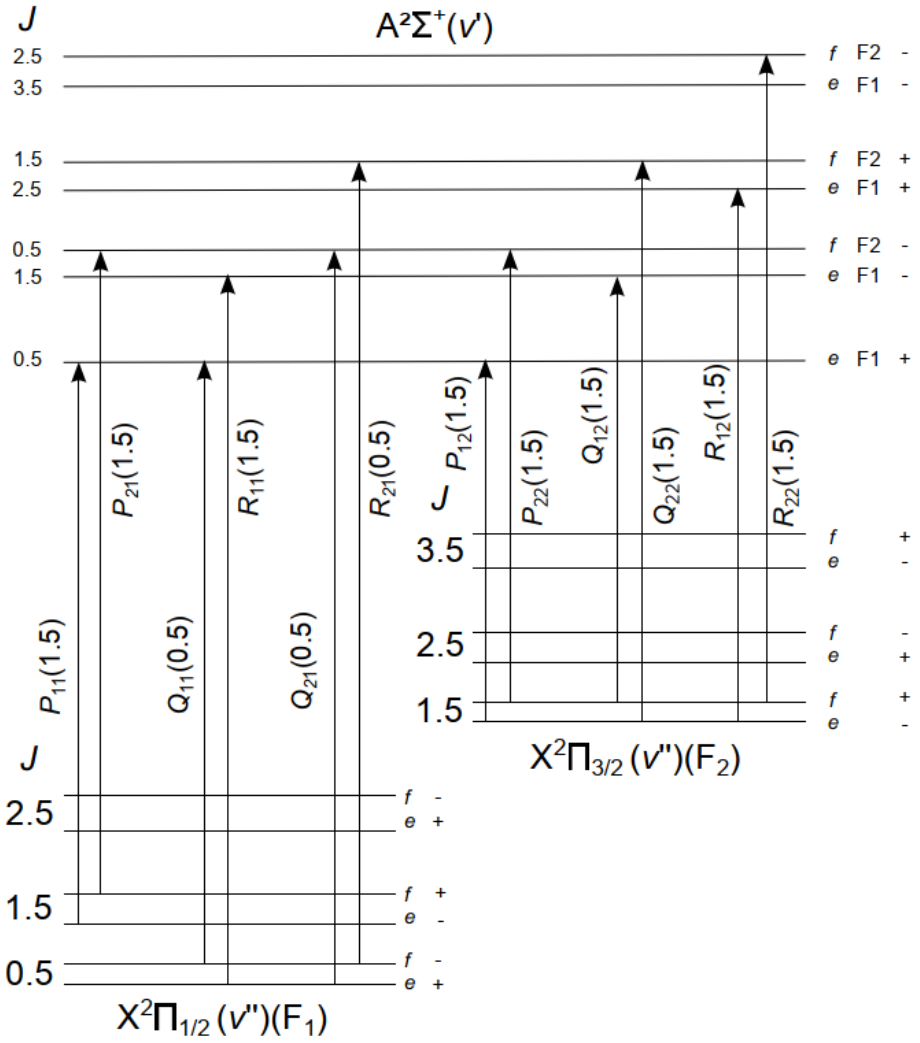

Figure 2.14: Rotational transitions for a vibrational band of the γ-band system of NO. Taken from Reference [32] under Creative Commons Attribution Non-commercial Non-Derivative 4.0 International license (CC BY-NC-ND 4.0).

3 Experimental setup

This chapter will give an overview over the equipment and experimental conditions needed to successfully carry out molecule-surface scattering experiments. To guarantee the cleanliness of the surface, these experiments have to be carried out in ultra-high vacuum (UHV) and the required apparatus will be described in the first part of this chapter. The second part focuses on the used experimental methods - surface preparation, and characterization as well as the optical preparation and ionization of nitric oxide.

3.1 Molecule-surface scattering apparatus

A sketch of the molecule surface scattering apparatus used in the experiments for this thesis is shown in Fig. 3.1. The pulsed molecular beam is formed by expansion of NO in different carrier gases (see Table 3.1) through a home-built nozzle of Even-Lavie-design[82] in the SOURCE CHAMBER (1) with 8 bar backing pressure, resulting in pulses of 30-40 µs length FWHM. The molecules then pass a skimmer and two differentially pumped stages (DIFF I (2) and DIFF II (3)), and enter the UHV-CHAMBER (4), where they scatter from the surface. The four chambers are pumped by the following pumps, resulting in the base pressures noted in Figure 3.1.

- Source chamber: Leybold Turbovac Mag W2200 iP, 2100 Ls^{-1}
- Diff. I: Leybold Turbovac 350 iX, 350 Ls^{-1}
- Diff. II: Osaka Vacuum TF160CA, 120 Ls^{-1}
- UHV chamber: Pfeiffer TPU 240, 240 Ls^{-1}, backed by Pfeiffer TPU 062, 60 Ls^{-1}

The molecules can be prepared in a specific quantum state using a narrow bandwidth pulsed IR laser before or after scattering, and are ionized via 1+1-REMPI using a pulsed UV laser. The NO^+ ions are detected with two MCP plates in chevron configuration. A detailed sketch of the detection region and the laser positions is shown in Figure 3.2 b. The

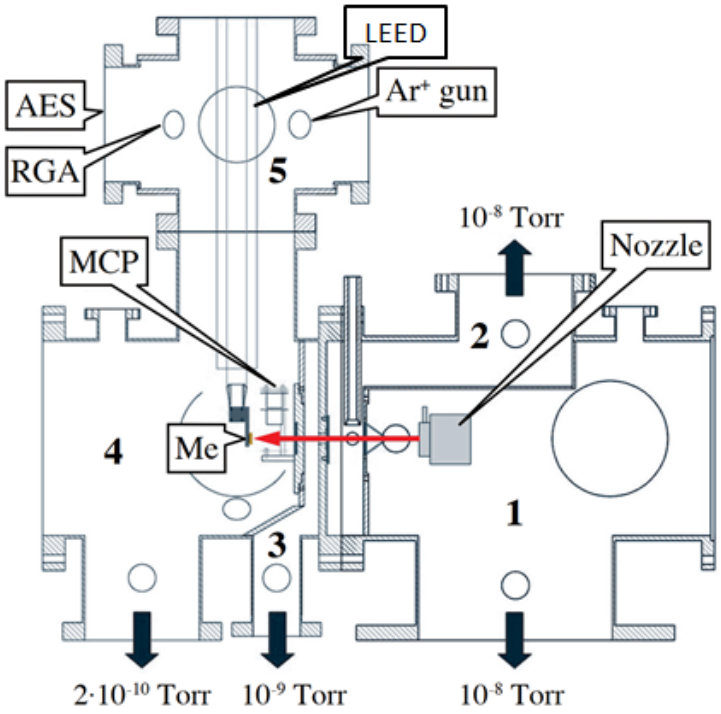

Figure 3.1: Sketch of the vacuum chamber used for the experiments.[81] The chamber consists of four differentially pumped stages. The nozzle is located in the source chamber (1) and the molecular beam is formed by supersonic expansion of NO seeded in He oder Ne as carrier gases. The beam then passes through a skimmer into the first differential chamber (2), through a small orifice into the second differential chamber (3) and then into the UHV-chamber (4), where the surface scattering experiment takes place. The surfaces are mounted on a double sided sample holder (see Figure 3.2 a) and can be moved between the scattering position and the preparation chamber (5) with the manipulator (4-axis: x, y, z, θ). The preparation chamber contains the equipment necessary for surface preparation and characterization: Quadrupole mass spectrometer (RGA), Auger electron spectrometer (AES), LEED and an Ar^+-ion gun. Reused and modified from ref. [81] with permission from the author (added "LEED").

crystals (Pt(111), Au(111) or HOPG) are mounted on a two-sided sample holder with tantalum wires, and can be resistively heated up to 1050 K while the temperature is measured using K-type thermocouples that are fixed inside a small hole drilled into the crystal. With the molecular beam turned on, all pressures rise by one order of magnitude. The preparation chamber (5) is directly connected to the UHV chamber, and contains and Ar-ion gun (LK Technologies NGI3000-SE) for surface cleaning, a quadrupole mass spectrometer (residual gas analyzer (RGA), SRS RGA200), an Auger electron spectrometer (AES, STAIB ESA 100) and a LEED spectrometer (Low Energy Electron Diffraction, OCI Vacuum BDL600IR-LaB_6-LMX-ISH), the latter two being used for surface characterization.

As shown in Figure 3.2 b, the focus of the IR laser used for optical preparation of the NO is located 1.5 mm in front of the surface, which is close enough to hit both the incoming

and the scattered beam. The REMPI laser is located about 11.5 mm away from the surface, below the ion lenses of the detector. The REMPI laser is located about 4 mm above the incoming molecular beam during the measurements of scattered molecules to suppress background signal from the incoming molecular beam. For the measurement of angular distributions, the ionization laser is moved in 0.6 mm steps along the green arrow in Figure 3.2 b.

3.2 Experimental methods

Each day before starting the experiments, the HOPG and Gr/Pt surfaces were annealed at 700 °C for 15 minutes to remove any adsorbates that might have accumulated over night.

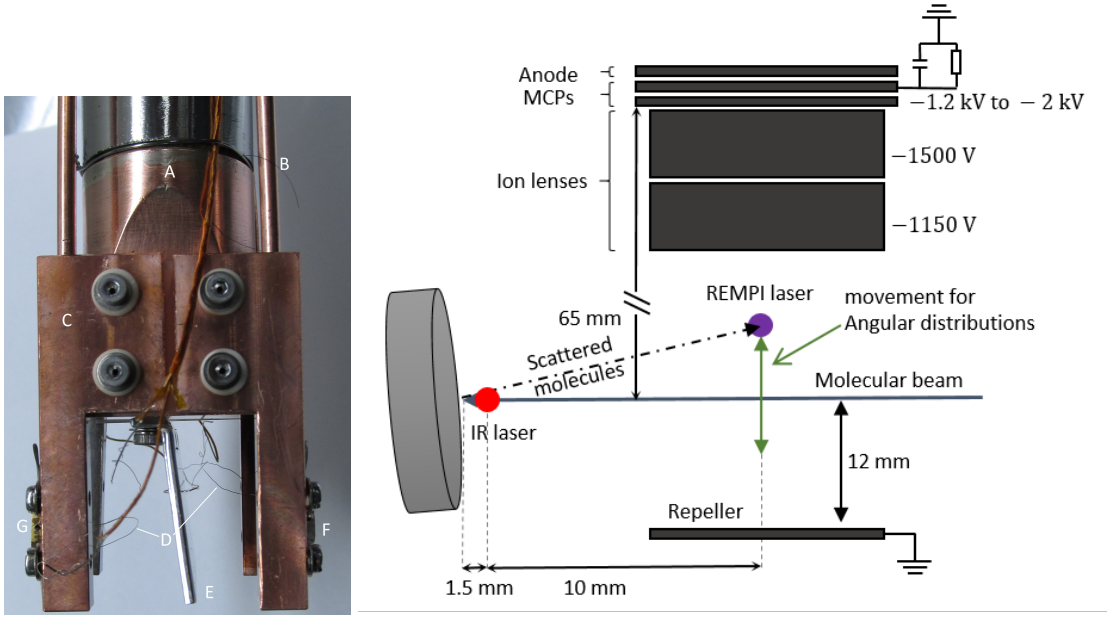

(a) (b)

Figure 3.2: (a) Picture of the double sided sample holder. Two pairs of copper arms (C) are mounted on a cold finger (A). They are electrically insulated using sapphire plates. The metal single crystals (F, Pt(111)) and (G, Au(111)) can be heated individually via resistive heating and are connected by copper rods (B). A heat shield (E) inhibits evaporation of material from one crystal to the other. The surface temperatures are measured using K-type thermocouples (D). (b) Schematic drawing of the detection region. The detector consists of a grounded repeller plate, two ion lenses (−1150 V and −1500 V) and two MCPs in chevron configuration. The MCPs are at a base voltage of −1200 V and are pulsed to up to −2000 V, depending on the required sensitivity. The molecules are tagged 1.5 mm in front of the surface by the IR laser and ionized about 10 mm further away. For further details on tagging and ionization see sections 3.2.2 and 3.2.1, respectively. To measure the angular distributions of the scattered molecules, the REMPI laser is moved up and down along the green arrow. Note that the surfaces are tilted by about 4° to separate the directly scattered from the incoming molecules.

Table 3.1: Gas mixtures used for the experiments and their measured mean velocities and mean energies.

gas mix	$\overline{v}/\mathrm{m}\cdot\mathrm{s}^{-1}$	$\overline{E}/\mathrm{eV}$
1% NO in H_2	2573 ± 100	1.03 ± 0.08
1% NO in He	1785 ± 76	0.49 ± 0.04
10% NO in He	1445 ± 44	0.33 ± 0.02
1% NO in Ne	830 ± 25	0.108 ± 0.006

The integrity of the graphene was checked using LEED at the start and at the end of each set of measurements. The Au(111) crystal that is used as a reference in the vibrational excitation experiments, was sputtered using Ar^+-ions (3 kV, $2.5 \cdot 10^{-6}$ torr Ar pressure, 20 minutes) before annealing at 700 °C for 30 minutes.

3.2.1 REMPI

Resonance enhanced multiphoton ionization (REMPI) is a technique that enables ionization of gas molecules with quantum state resolution.[83,84] A general REMPI scheme is labeled as $m + n$-REMPI, where m and n are the number of photons required for the resonant and the ionization step, respectively. If two different photon energies are required, the labeling changes to $m+n'$-REMPI. Since the spectroscopy of nitric oxide has been well known for years, a few different REMPI schemes exist.[56,76] For this work, 1+1 REMPI of NO was used, meaning that one photon was used for the resonant $A^2\Sigma^+ \leftarrow X^2\Pi$-transition, and a second photon of the same wavelength ionizing the molecules in the A-state. This allows for the recording of rotationally resolved spectra of different vibrational bands of NO. The used wavelengths are listed in Table 3.2. A potential energy diagram of nitric oxide and example transitions are shown in Figure 3.3.

The second harmonic (SHG) of a pulsed dye laser (Sirah Cobra-Stretch) that is pumped by the third harmonic (THG) of a Nd:YAG-Laser (Continuum Surelite SLIII-Ex) running at 10 Hz was used as the REMPI laser system and the setup is shown in Fig. 3.4. All vibrational bands listed in Table 3.2 could be accessed with a dye mix of 95% C480 and 5% C503 (0.38 g/L and 0.02 g/L, respectively) in ethanol, with added DABCO[1] (1 g/L) for longer dye-lifetimes.

[1] 1,4-diazabicyclo[2.2.2]octane

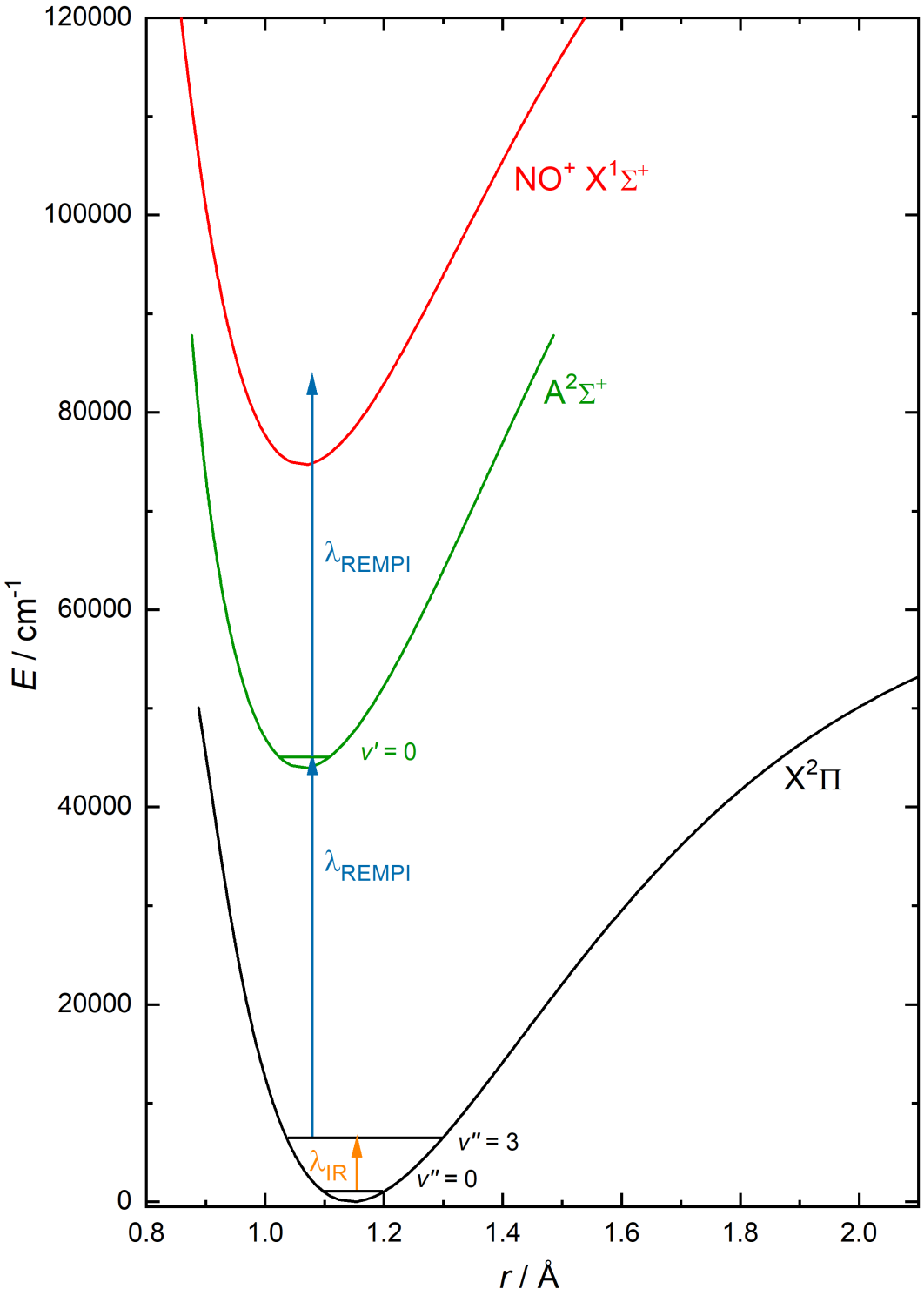

Figure 3.3: Potential energy diagram of the relevant electronic states of NO. The arrows indicate the optical preparation using the IR laser (orange) and the 1+1 REMPI transition via the A($v' = 0$) state (blue). Adapted from references [32, 76].

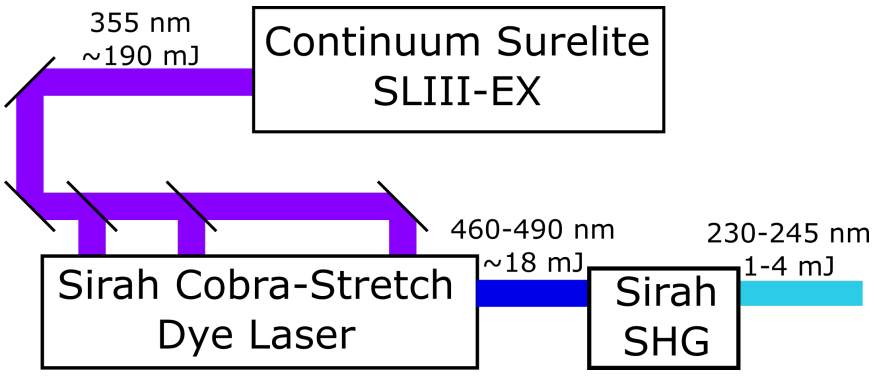

Figure 3.4: Sketch of the UV Laser system used as the REMPI laser. A Sirah Cobra-Stretch pulsed dye laser is pumped by the THG of a Nd:YAG laser (Continuum Surelite SLIII-EX, 10 Hz), producing about 18 mJ of blue light, which is then frequency doubled in the Sirah SHG unit (BBO) to the desired wavelength region with 1-4 mJ output power.

Table 3.2: REMPI transitions and the scan ranges for the whole vibrational band.

transition	$\lambda_{\mathrm{REMPI}}/\mathrm{nm}$
$A^2\Sigma^+(v'=0) \leftarrow X^2\Pi(v''=1)$	$233.0 - 237.5$
$A^2\Sigma^+(v'=0) \leftarrow X^2\Pi(v''=2)$	$245.0 - 248.0$
$A^2\Sigma^+(v'=1) \leftarrow X^2\Pi(v''=3)$	$242.0 - 245.0$

Analysis of REMPI spectra

The population factor $x(v, J, \Omega)$ for each quantum state has to be known to acquire the rotational and vibrational state distributions of the scattered molecules, where each quantum state is defined by the quantum numbers v for vibration, J for the total angular momentum and Ω for the projection of J on the molecular axis (see also section 2.4). The measured REMPI spectrum $S_{\mathrm{NO}}(\tilde{\nu})$ can be simulated using Equation 3.1, where $\tilde{\nu}$ is the wavenumber of the REMPI transition.[32]

$$S_{\mathrm{NO}}(\tilde{\nu}) = \sum_{v} \sum_{J} \sum_{\Delta v} \sum_{\Delta F} \sum_{\Delta J} x(v, J, \Omega) f(v, J, \Omega, \Delta v, \Delta J, \Delta F) \\ g(\tilde{\nu}, \tilde{\nu_0}(v, J, \Omega, \Delta v, \Delta J, \Delta F)) \tag{3.1}$$

The detection efficiency $f(v, J, \Omega, \Delta v, \Delta J, \Delta F)$ of a single quantum state in the electronic ground state is specified by $\Delta v, \Delta J, \Delta F$. ΔF describes the change of the spin label, Δv that of the vibrational and ΔJ that of the rotational state in the A $\leftarrow$ X-transition of the REMPI scheme. Finally, $g(\tilde{\nu}, \tilde{\nu_0}(v, J, \Omega, \Delta v, \Delta J, \Delta F))$ is a line shape function around the center wavenumber $\tilde{\nu_0}$ for each electronic transition.[32] The analysis of the measured REMPI

spectra was carried out using a WOLFRAM MATHEMATICA notebook that is described in detail in references [80] and [32]. To summarize very briefly, the measured data is first corrected for the REMPI laser power (assuming a linear power dependence)[80] and for the detector voltage. Then a spectrum of the chosen vibrational band is simulated using Brown's hamiltonian[73] and the spectroscopic constants from References [75] and [77] for the X- and A-state, respectively. Using the population factors $x(v, J, \Omega)$ as fit parameters, the difference between simulation and measured spectrum is then minimized and the population P of a specific quantum state results from Equation 3.2:[32]

$$P(v, J, \Omega) = \frac{x(v, J, \Omega)}{\sum_v \sum_J \sum_\Omega x(v, J, \Omega)}. \tag{3.2}$$

Figure 3.5 shows an example of a measured REMPI spectrum and the corresponding simulation.

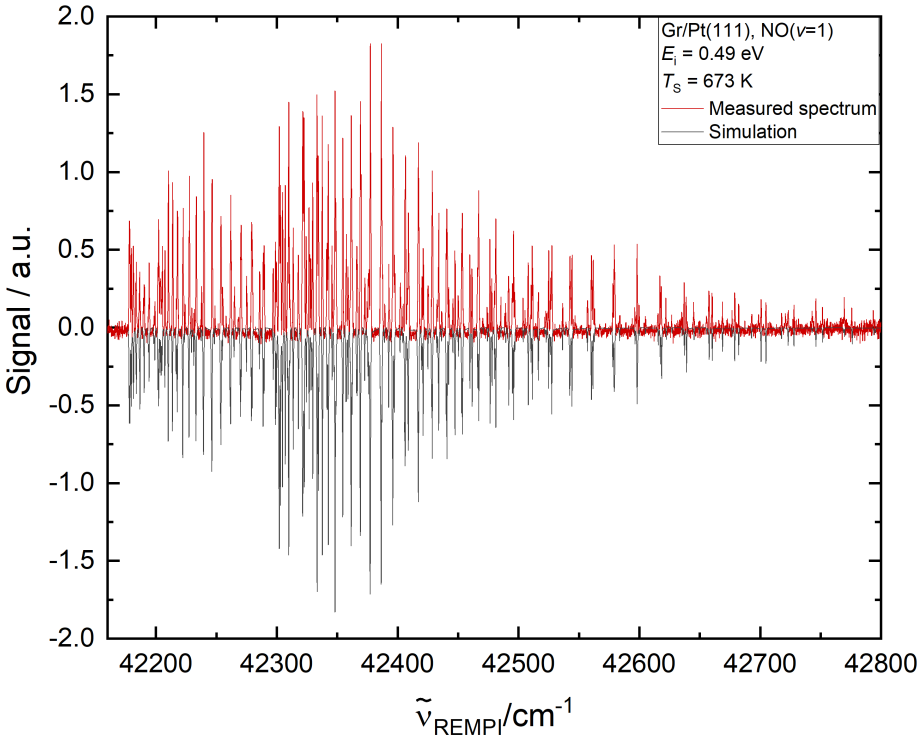

Figure 3.5: Measured REMPI spectrum of the NO($v = 1$) band (red) and the spectrum simulated using the method described above (gray).

The correction factor for the detector voltage (the MCP gain) was determined experimentally. The UHV chamber was filled with a background pressure of $2.5 \cdot 10^{-9}$ torr NO and the REMPI laser set to the Q_{11} branch of the A($v' = 0$) ← X($v'' = 0$) transition at 226.25 nm. The NO^+ ion signal was then measured as a function of the MCP-voltage, and

the correction factors for the MCP gain were obtained by fitting an interpolation function to the normalized ion signal, as shown in Figure 3.6.

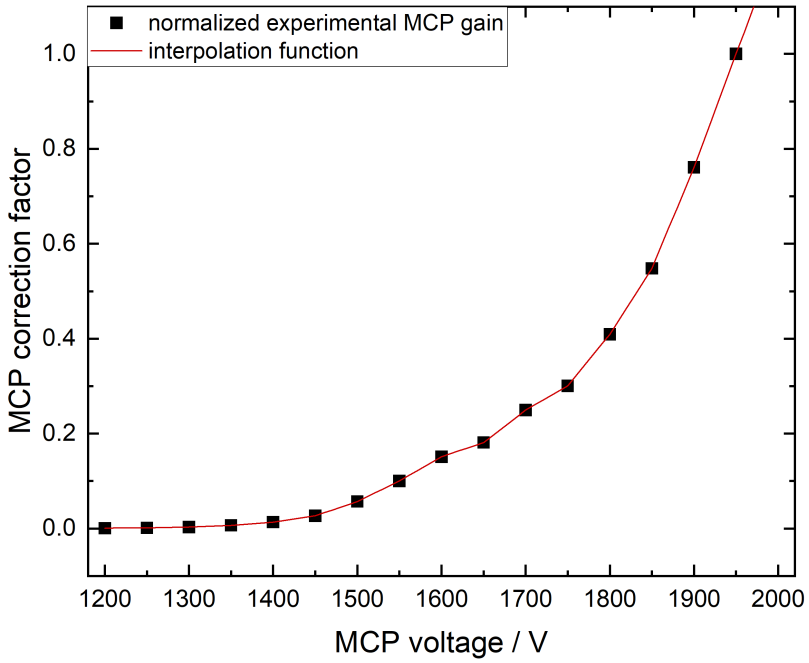

Figure 3.6: Normalized MCP gain (black squares) and the interpolation function (red line) used for correction of the measured REMPI spectra. Data was obtained by filling the UHV chamber with a background pressure of $2.5 \cdot 10^{-9}$ torr NO and measuring the ion signal as a function of the MCP voltage, using the Q_{11} branch of the $A(v' = 0) \leftarrow X(v'' = 0)$ transition at 226.25 nm.

Determination of absolute vibrational excitation probabilities using Au(111) as a reference

Absolute vibrational excitation probabilities could be determined, because a two-sided sample holder was used. A Au(111) and a Pt(111) sample were mounted on opposite sites at the same time, see Figure 3.2 a. This allowed back-to-back measurements of the vibrational excitation probability within ~20 minutes for both surfaces. Under these conditions, fluctuations in the experiment (e. g. in the molecular beam) were assumed negligible.

The whole population distribution over all states has to be known to know the absolute population of a single quantum state $P(v, J, \Omega)$, as well as the angular distribution and the kinetic energy distribution of the scattered molecules. As the detection only happens in a very small volume, the signal in that detection volume will be much weaker for a broad angular distribution than for a very narrow (e. g. specular) angular distribution. In a similar fashion, this effect is important for the velocity distribution of the scattered molecules

and thus both have to be taken into account. Determining the population of the vibrational ground state can also be rather difficult, because of the large NO($v = 0$) background from the incoming beam. On top of that, rotational line strengths, Franck-Condon factors (for the resonant A ← X-transition) and the ionization cross section (which also depends on the photon energy) have to be considered for each individual state. Cooper *et al.* considered all these factors and determined the absolute vibrational excitation probabilities of the NO/Au(111) system.[85]

As mentioned earlier, it is possible to use the data of Cooper *et al.* as an internal reference to determine the absolute vibrational excitation probabilities for the NO/Gr/Pt(111)-system, because NO/Au(111) and NO/Gr/Pt(111) were mounted on opposite sites of the double sided sample holder. The NO($v = 1$)-spectrum is first recorded with a specific incidence energy and surface temperature for the Au(111) surface. The molecular beam is then blocked, the Gr/Pt(111) surface moved into position, and the scan is repeated. Both surfaces are measured back to back to ensure similar conditions of the incoming molecular beam.

The recorded data were analyzed as described above and the measured values for NO/Au(111) were set to the values of reference [85] using the closest experimental conditions. The same correction factor was then applied to the NO/Gr/Pt(111) values to gain the absolute vibrational excitation probabilities.

3.2.2 State-to-state time of flight

In order to improve time-resolution, a second laser with a pulse duration of 10 ns is introduced to *tag* the molecules. As stated in the previous section, the FWHM of the molecular beam is 30-40 µs, which means that using the whole pulse, one cannot distinguish between trapping-desorption and direct scattering channels (see section 2.2). For points in time, t_0 and t_1 (with $t_0 < t_1$), the direct scattering component of the molecules hitting the surface at t_1 will overlap with the trapping-desorption component of the molecules that hit the surface at t_0. Tagging refers to the excitation of a state of interest to a state that is not present in the incoming beam, reducing the FWHM to 1-2 µs, because the time resolution of the tagged molecules is limited by the interaction region of the IR tagging laser with the molecular beam and not the laser pulse width. The REMPI laser is then tuned to ionize molecules in the tagged state, making the rest of the beam (the *untagged* part) "invisible". Figure 3.3 shows an example for NO($v = 3$). In the incoming molecular beam, more than 99.9% of all molecules are in the ground vibrational state $v = 0$. This tagging can take place before or after the scattering event (or both), depending on the chosen transition.

The transitions and wavelengths used for the current experiments are listed in Table 3.3. The time of flight spectra are measured by recording the ion signal as a function of time delay between the lasers.

Table 3.3: IR and REMPI transitions and frequencies used for state-to-state time of flight experiments. IR transitions were chosen based on the population of the starting-J-state in the incoming beam, and molecules were tagged before scattering if not noted otherwise. For the chosen REMPI transitions, there were no other ro-vibrational lines within 0.5 cm^{-1} and they all ionized different rotational states of NO($v = 3$). See Figure 3.7 for a sketch clarifying when the molecules were tagged.

IR excitation			REMPI		
$v \rightarrow v'$	rot. transition	$\tilde{\nu}/cm^{-1}$	ionized state	branch	λ_{REMPI}/nm
$0 \rightarrow 3$	R(0.5)	5548.875	1.5	Q_{11}	243.926
			8.5		243.639
			16.5	R_{11}	243.120
			22.5		242.565
			27.5		241.995
			31.5	P_{22}	243.138
$0 \rightarrow 3^{\dagger}$	R(16.5)	5585.852	17.5	Q_{11}	258.139
$1 \rightarrow 3^{\dagger}$	R(8.5)	3695.983	9.5	Q_{11}	258.577
	R(16.5)	3714.717	17.5		258.139
	R(22.5)‡	3725.800	23.5		257.611
	R(27.5)‡	3733.057	28.5		257.043
	R(31.5)‡	3737.546	32.5		256.507

†Molecules tagged after scattering from the surface.

‡Transitions not useful due to low signal to noise.

The rotational distribution of the incoming beam is shown in Figure 3.8. The rotational temperature is about 20 K, hence the population $P(J)$ for $J > 7.5$ is very small ($P(J > 7.5) < 1 \cdot 10^{-4}$). This knowledge combined with a suitable choice of states to pump gives the opportunity to investigate different scattering channels.[86] Exciting the $v = 0 \rightarrow 3$ R(0.5) transition before scattering and detecting NO($v = 3$) enables background-free investigation of the vibrationally elastic $v = 3 - 3$ channel (read as $v = 3$

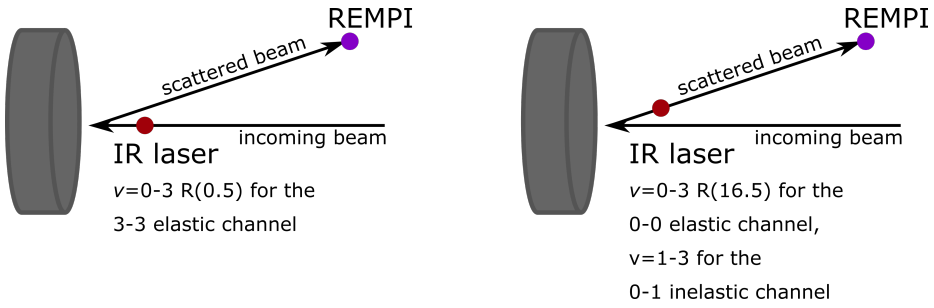

Figure 3.7: Illustration of the tagging setup. (left) For investigation of the vibrationally elastic $v = 3 - 3$ channel, the molecules were tagged in the incoming beam shortly before the collision with the surface. (right) For the time of flight (ToF) measurements of the vibrationally elastic $v = 0 - 0$ and the vibrationally inelastic $v = 0 - 1$ channels, the molecules were tagged after scattering from the surface. Note that the position of the IR tagging laser changes in the figure to highlight which molecules were tagged. In the experiment, the position was not changed. All used transitions are listed in Table 3.3.

to $v = 3$ scattering channel). To investigate the $v = 0 - 0$ channel, the $v = 0 \rightarrow 3$ R(16.5) transition is chosen, because $J = 16.5$ is not present in the incoming beam. As a consequence, if any NO($v = 0, J = 16.5$) is detected after tagging, it had to be rotationally excited during the collision with the surface. Investigation of the $v = 0 - 0$ channel is important, because trapping desorption and direct scattering are expected to be visible (if both happen), whereas the $v = 3 - 3$ channel will most likely only show the direct scattering component. Figure 3.7 shows a sketch clarifying when and where the molecules were tagged for each of the investigated channels.

To excite and tag single ro-vibrational transitions in diatomic molecules, a narrow-bandwidth infrared laser system is used. A sketch of this laser system is shown in Figure 3.9. A cw-ring dye laser (Sirah Matisse DR, pumped by a Coherent Verdi-V10) produces approximately 380 mW narrow bandwidth radiation around 669 nm, which is then pulse-amplified in a pulsed dye laser (Sirah PulseAmp 5X) that is pumped by the SHG of a seeded Nd:YAG-Laser (~300 mJ, SpectraPhysics Quanta Ray Pro 230) to produce 30-40 mJ of narrow bandwidth pulsed red light. The output of a difference frequency mixing unit (pulsed amplifier output and fundamental of the Nd:YAG) is amplified in an OPA-process to generate the needed wavelengths. The signal or idler photons (1.802 µm, 10 mJ and 2.676 µm, 6 mJ respectively) created by this process can be used, depending on the transition.

State-to-state time of flight analysis

On the time scale of a laser pulse (~10 ns) the molecules are approximately at rest, because the molecules would take approximately two orders of magnitude longer to cross

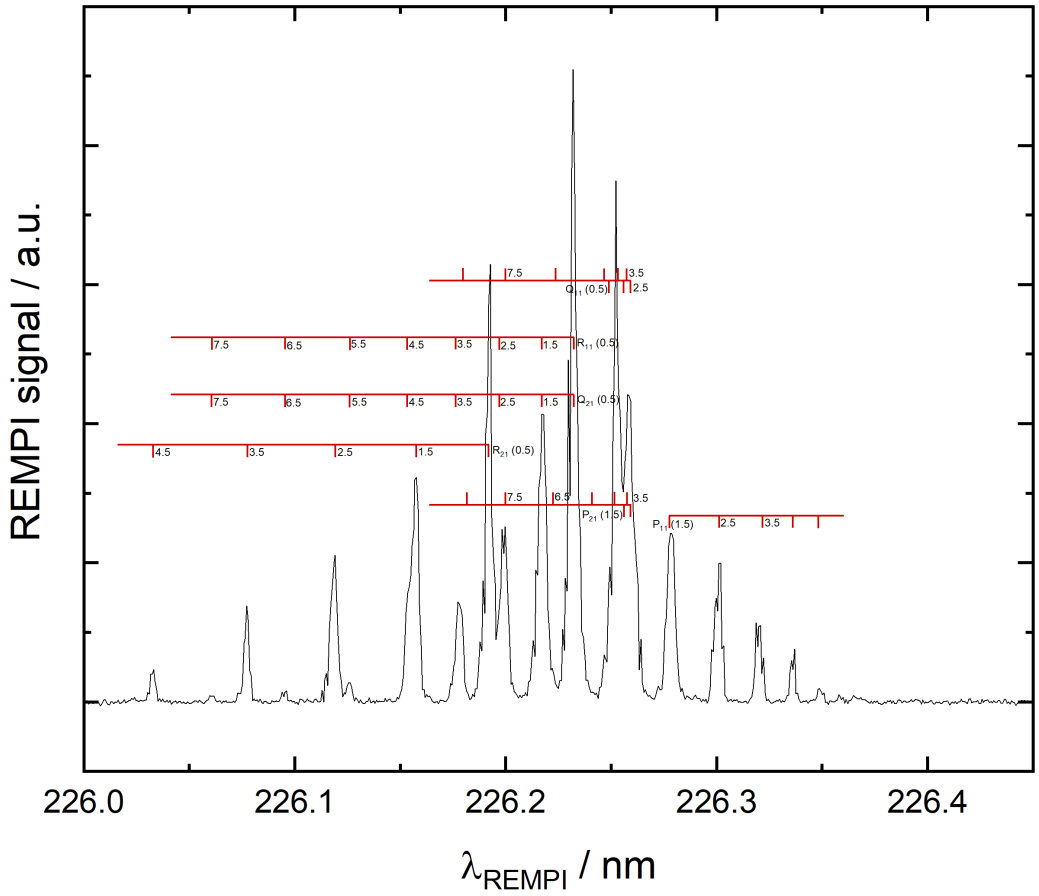

Figure 3.8: Measured rotational distribution with assigned transitions of NO($v = 0$) in the incoming beam. The rotational temperature is about 20 K due to efficient rotational cooling during a supersonic expation. Hence, J-states with $J > 7.5$ are barely populated. The rotational lines were assigned using LIFBase[87].

the interaction region compared to the length of the laser pulse. As the REMPI signal S is proportional to the number density, the measurement yields density distributions. These need to be converted to flux, because flux is proportional to probability, in constrast to density. Conversion of density to flux is achieved by multiplication with the time dependent velocity $v(t)$.[88] Since state-to-state time of flight measurements involve two laser pulses (IR tagging laser and REMPI laser), the density-to-flux conversion needs to be applied twice, once per laser pulse.[81] The data is fitted with a flowing 3D-Maxwell-Boltzmann distribution with the center velocity v_0 and the width parameter α.[32,56]

$$P(v) = Av^2 \exp\left[-\left(\frac{v - v_0}{\alpha}\right)^2\right] \quad \text{with} \quad v = \frac{l}{t}, \tag{3.3}$$

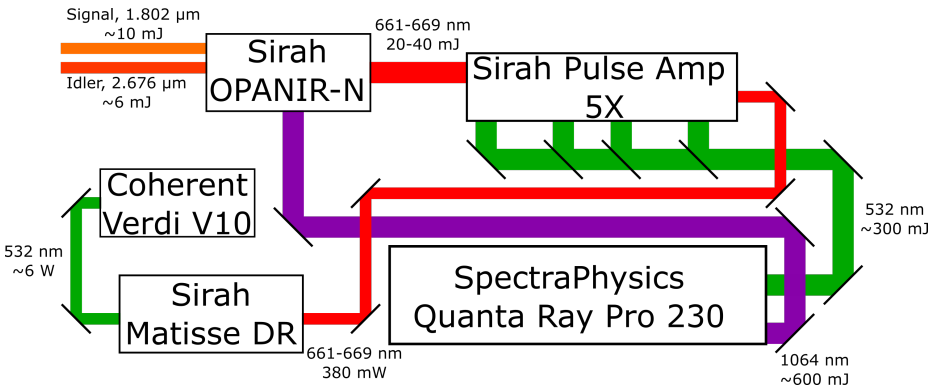

Figure 3.9: Narrow bandwidth IR laser system used for optical preparation of NO. The Sirah Matisse DR ring dye laser (pumped by a Coherent Verdi V10) produces a narrow bandwidth cw output between 661 nm and 669 nm. The Sirah Pulse Amp 5X (pumped by the SHG of a seeded SpectraPhysics Quanta Ray Pro 230) turns this cw radiation into approx. 30 mJ at 10 Hz of narrow bandwidth pulsed light. The Sirah OPANIR-N then produces the desired signal output via difference frequency mixing (LNB) of the pulse amp output and the fundamental of the Nd:YAG laser, which is then amplified in an OPA process (LNB) that also generates the idler output. Depending on the excitation channel, both signal and idler output can be used.

l being the distance and t the flight time. To fit the measured data, this distribution has to be converted into time-space while also applying the density to flux conversion, using

$$S(t)v^2\mathrm{d}t = P(v)\mathrm{d}v \tag{3.4}$$

$$\Rightarrow S(t) = P(v)\left|\frac{\mathrm{d}v}{\mathrm{d}t}\right| v^{-2}, \tag{3.5}$$

and the Jacobian[88]

$$\left|\frac{\mathrm{d}v}{\mathrm{d}t}\right| = \frac{l}{t^2}, \tag{3.6}$$

which leads to

$$S(t) = P(v)\frac{l}{t^2}\left(\frac{t}{l}\right)^2 = P(v)l^{-1} \tag{3.7}$$

$$\Rightarrow S(t) = A\left(\frac{l}{t}\right)^3 \exp\left[-\left(\frac{v-v_0}{\alpha}\right)^2\right] l^{-1}. \tag{3.8}$$

Fitting the time of flight data then gives the fit parameters v_0 and α in mm/µs as well as the amplitude A. To transform the velocity distribution $P(v)$ into an energy distribution $P(E)$, the following relation has to be considered:

$$P(E)\mathrm{d}E = P(v)\mathrm{d}v \tag{3.9}$$

$$\Rightarrow P(E) = P(v)\left|\frac{\mathrm{d}v}{\mathrm{d}E}\right|, \tag{3.10}$$

again using the Jacobian

$$\left|\frac{\mathrm{d}v}{\mathrm{d}E}\right| = \frac{1}{mv} = \frac{1}{m\sqrt{\frac{2E}{m}}} \quad \text{with} \quad m = m_{\mathrm{NO}}, \tag{3.11}$$

which then leads to the energy distribtion:[81]

$$P(E) = A\frac{2E}{m^2}\exp\left[-\left(\frac{\sqrt{\frac{2E}{m}} - v_0}{\alpha}\right)^2\right]. \tag{3.12}$$

Using these equations, the state-to-state time of flight data can be analyzed and transformed into velocity and energy space. If $v_0 = 0$, the distribution turns into a thermal Maxwell-Boltzmann distribution with

$$\alpha = \frac{m}{2k_{\mathrm{B}}T}. \tag{3.13}$$

3.2.3 Angular distributions

Traditionally, to measure angular distributions, a detector (often a mass spectrometer) is moved on a circular path in front of the surface.[89] In this work, the REMPI laser is moved parallel to the surface, because the detector is fixed inside the machine. See the the green arrow in Figure 3.2 b or the arrow in Figure 3.10 for a sketch of how the angular distributions are measured. The scattering angle β can be calculated when the distance between the ionization laser and the surface is known. The angular resolution of these measurements is $\sim 10^{\circ}$.[56]

Moving the REMPI laser along the z-axis changes the distance between the point of ionization and the detector, which changes the efficiency of the ion lenses. To correct this change in ion collection efficiency, the chamber was filled with $2{\cdot}10^{-9}$ torr nitric oxide and the signal as a function of the z-position of the REMPI laser was recorded, which is shown in Figure 3.11. A possible issue of this calibration method is that ionizing background gas will result in production of ions in positions that are never reached by scattered molecules. This is especially important for 1+1 REMPI with an unfocused laser, because ions will be produced along the complete laser path and not just in front of the surface, where the scattered molecules are detected.

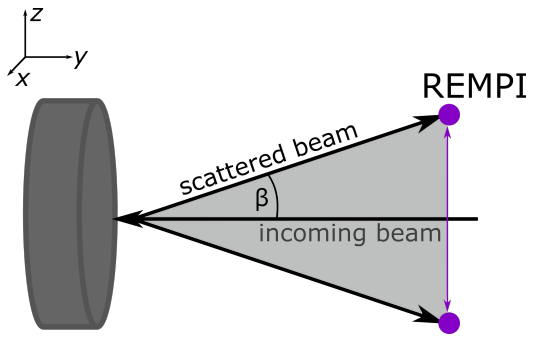

Figure 3.10: Sketch of the experimental setup to measure angular distributions of the scattered molecules. The REMPI laser is moved along the z direction and the signal is recorded. The scattering angle β can be calculated with knowledge of the laser-surface distance and the position of the REMPI laser along z.

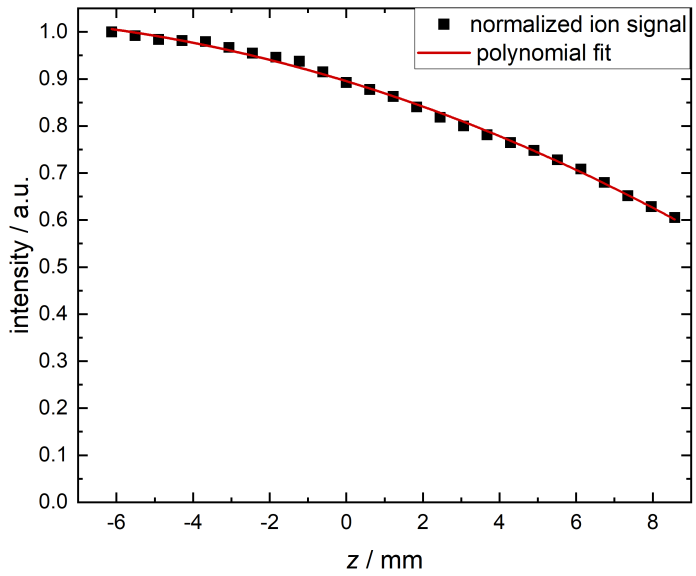

Figure 3.11: Measured ion collection efficiency, by moving the ionization laser along the z direction while the chamber was filled with $2 \cdot 10^{-9}$ torr nitric oxide. The position of the REMPI laser on the x-axis is scaled with respect to the molecular beam at $z = 0$. Larger values of z are closer to the detector.

The two biggest problems with this method of measurement are that density and temporal dilution need to be accounted for.[81] Moving the ionization laser along a line results in longer flight paths for larger scattering angles, as shown by the red and blue circles in Figure 3.12. Since the molecules do not have a single velocity, but follow a velocity distribution, they spread in time with increasing flight distances, resulting in lower densities at the point of ionization. Also, the section of the molecular beam that is detected changes for large scattering angles, because of the longer flight path. For a velocity of 1000 m/s and a scattering angle of 50°, this results in a shift of roughly 3 µs. Correcting for this shift

is done by measuring the time of flight distributions at all positions of z.[81]

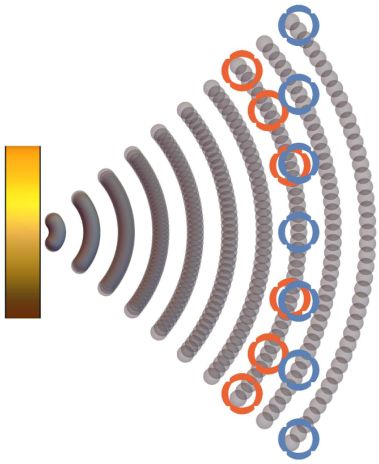

Figure 3.12: Sketch of the molecules leaving the surface after the scattering. The red circles indicate the ideal detection geometry for angular distributions. Moving a detector on a circular path in front of the surface results in a constant density of molecules getting detected. The blue circles indicate the method of measuring angular distributions used in the current work. Here, the REMPI laser is moved on a line parallel to the surface in z-direction, as shown in by the green arrow in Figure 3.2 b. This results in a decrease of density of detected molecules close to the edges of the angular distribution, and is especially important for broad angular distributions. Taken from reference [81] with permission from the author.

The dilution in density is caused by the pulse of scattered molecules spreading spatially, which is indicated by the grey circles in Figure 3.12. Close to the surface, a lot of circles are overlapping, indicating a high density. However, the detected density of molecules is higher for angles close to the surface normal compared to large scattering angles. To correct for this change, the measured density has to be multiplied by d^2, where d is the distance between the surface and the point of detection. This distance has to be taken into account twice, because the molecules spread in x and z direction. If the detection laser that propagates along the x-axis, is not focused, the spread in x-direction is accounted for, because all molecules in the cylindrical volume of the laser beam along x are detected. This changes the correction factor to d instead of d^2, but also means that the correction factor depends on the shape of the angular distribution itself.[81] All angular distributions in this work were corrected for the temporal and density dilutions.

3.3 Synthesis and stability of graphene

3.3.1 Growing graphene on Pt(111)

Growing graphene on platinum involves catalytic cracking of ethylene on the surface and is a self-terminated process, resulting in a monolayer of graphene.[90–92] Depending on the conditions of growth (ethylene pressure and surface temperature), the amount of nucleation sites and thus the growth rate changes. Choosing high pressures ($p_{\text{ethylene}} \geq 5 \cdot 10^{-8}$ torr) and high temperatures leads to a high nucleation rate, resulting in small graphene domains and a high density of grain boundaries, as well as the unwanted R30° domain of graphene being the prominent one.[54] In this case, the graphene is rotated by 30° with respect to the platinum surface. To reliably create the R19° species as the dominant one, the following recipe was used, which gave reproducible graphene LEED patterns. Please note that the possibility of the existence of other graphene domains is high, but the majority of the graphene consists of the R19° domains, as shown in the LEED pattern (Fig. 3.13, compare Figure 2.5 in section 2.1). This method of graphene growth was adapted from reference [35].

(1) Ar^+-ion sputtering of the Pt(111) crystal with 3 kV ions at a pressure of $2.5 \cdot 10^{-6}$ torr for 30 minutes.

(2) Annealing the crystal at 700 °C in $1.5 \cdot 10^{-7}$ torr O_2 for 30 minutes.

(3) Annealing at 900 °C without oxygen for 30 minutes.

(4) Flash-annealing to >1000 °C for 2 minutes.

(5) Dosing ethylene ($1 \cdot 10^{-8}$ torr) at 700 °C for 30 minutes with the surface facing away from the leak valve.

(6) Keeping the surface at 700 °C for 5 minutes while pumping the residual ethene.

3.3.2 Stability of graphene on Pt(111)

Epitaxial graphene is more reactive to oxidizing gases such as NO than clean noble metal surfaces. Hence this chapter will focus on the stability of graphene under different experimental conditions. The left panel of Figure 3.14 shows Auger electron spectra taken from the Gr/Pt(111) surface after exposure to $1.9 \cdot 10^{-8}$ torr NO at different surface temperatures. In this case, the NO was leaked into the UHV chamber via a leak valve with the surface

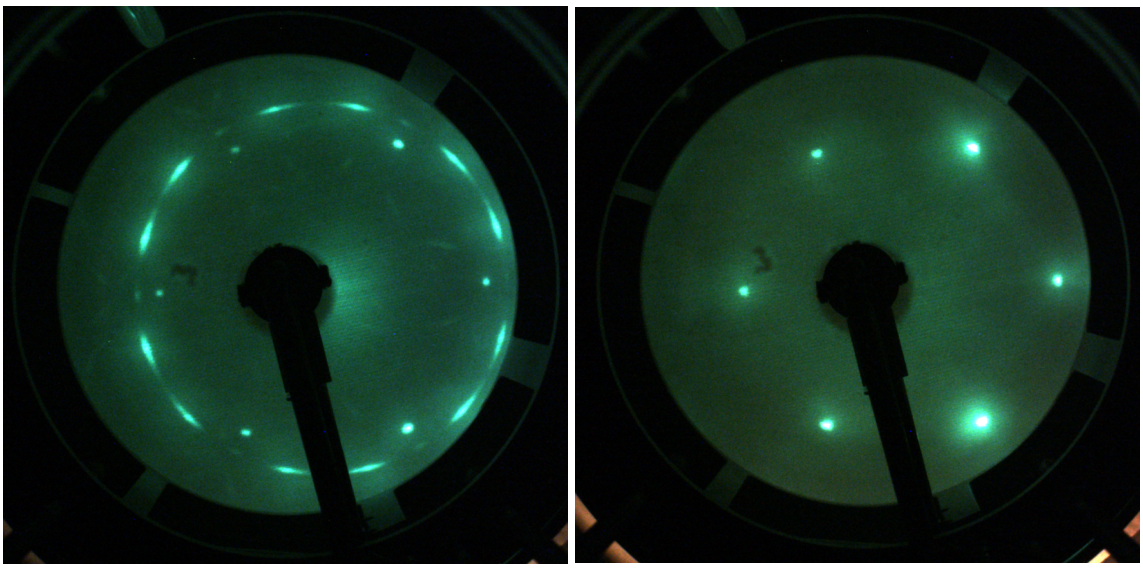

(a) (b)

Figure 3.13: (a) LEED image of freshly grown graphene on Pt(111). The six round spots that visible in (b) are caused by diffraction on the platinum substrate and show the sixfold symmetry of the (111) face. The elongated spots result from the graphene layer and are rotated by 19° with respect to the Pt-spots. See section 2.1, especially Figure 2.5 for a detailed explanation of the different orientations of graphene on Pt(111). Measured at 83 eV electron energy, 39 µA emission and 2.45 µA beam current at 650 ms exposure time. The LEED pattern is off-center, because the surface was tilted slightly. (b) LEED pattern of clean Pt(111).

facing away from the valve. Up to 1073 K, no changes in the carbon peak intensity (272 eV in the Auger spectrum, see red box in Fig. 3.14 a) were observed, but after 15 minutes at 1173 K the intensity of the carbon peak dropped and vanished nearly completely after another 10 minutes under these conditions. The LEED image taken afterwards (Panel B of Fig. 3.14 b) agrees with this, as the graphene spots clearly present for the fresh graphene (Panel A of Fig. 3.14 b) are barely visible anymore. In conclusion, under these conditions, the graphene is not stable above 1073 K.

In a follow-up experiment, the graphene was exposed to molecular beam of NO molecules with hyperthermal translational energy. The used gas mixtures are listed in Table 3.1. The NO/Ne gas mix was not used here. For both helium-seeded beams, minor damage was visible in the LEED image after long time exposure ($>$ 1 h) above 873 K surface temperature. Using hydrogen as a carrier gas resulted in the LEED images shown in Fig. 3.15, where the colored stars indicate the spot the LEED image was taken. All LEED images show damaged graphene (compare with upper panel of Fig. 3.14 b for a LEED image of pristine graphene). At the center spot that was hit by the molecular beam (white star, central LEED image), only the LEED pattern of a clean Pt(111) surface is visible.

Using the LEED, the size of the bare platinum spot was determined to have a diameter of about 2 mm, which agrees well with the size of the molecular beam. Further testing showed that this does not happen on a time scale relevant for the experiments when at or below 873 K. As a consequence, surface temperatures above this threshold were neglected for further experiments.

According to Choubak *et al.*,[93] pure hydrogen does not affect graphene, but etching is observed when even minor contaminations (<1 ppm) of oxidizing gases such as O_2 are present. Since the gas mixes used in this experiment need at least 1% NO for a usable signal-to-noise ratio after scattering, hydrogen was deemed an unfit carrier gas for NO/graphene scattering. Moreover, Kim *et al.* investigated graphene etching using electron beams.[94] They found that using a supersonic oxygen beam drastically boosts the

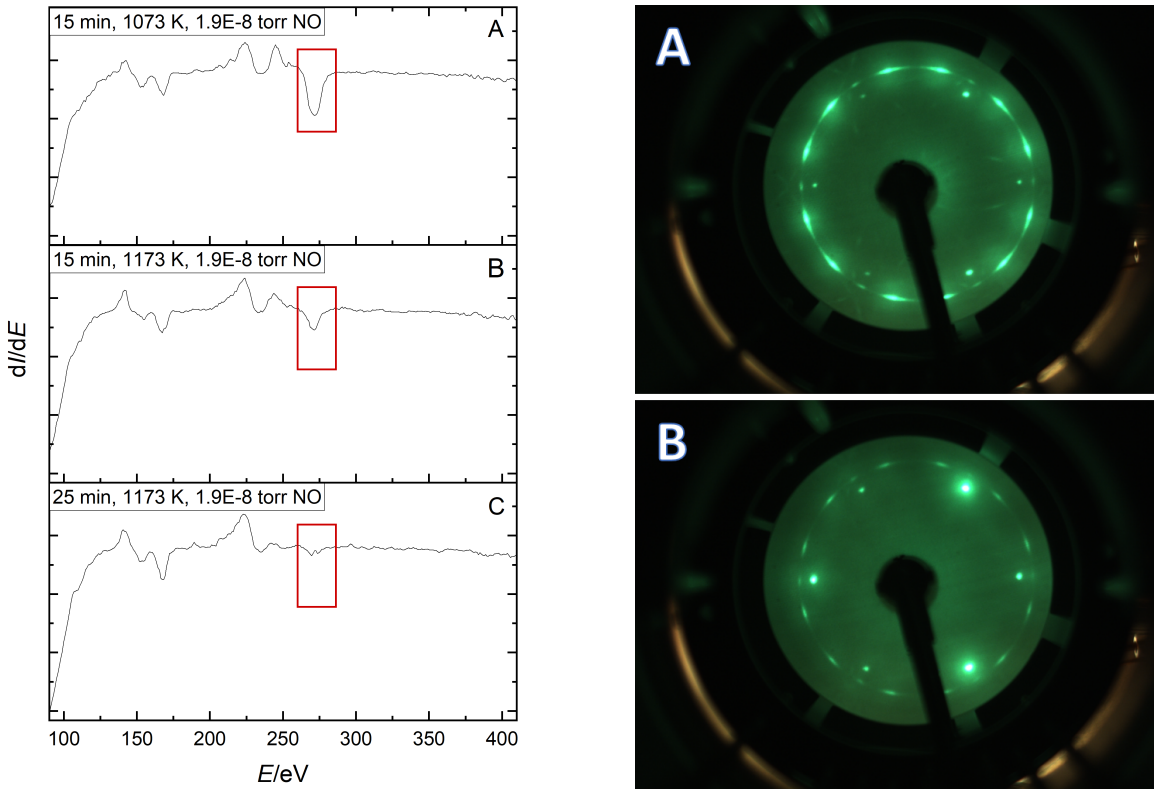

(a) (b)

Figure 3.14: (a) Auger electron spectrum of the Gr/Pt(111) surface after exposure to $1.9 \cdot 10^{-8}$ torr NO at different surface temperatures - A: 15 minutes, 1073 K; B: 15 minutes, 1173 K, C: 25 minutes, 1173 K. The red box highlights the carbon peak at 272 eV. Up to 1073 K, no decrease in carbon intensity was observed but is clearly visible under the conditions shown here. (b) A: LEED pattern of fresh graphene, showing both the distinct spots of the R19° graphene domains as well as the Pt(111) spots underneath. B: LEED pattern after 25 minutes of $1.9 \cdot 10^{-8}$ torr NO exposure at $T_S = 1173$ K. The graphene spots are barely visible anymore, indicating major damage.

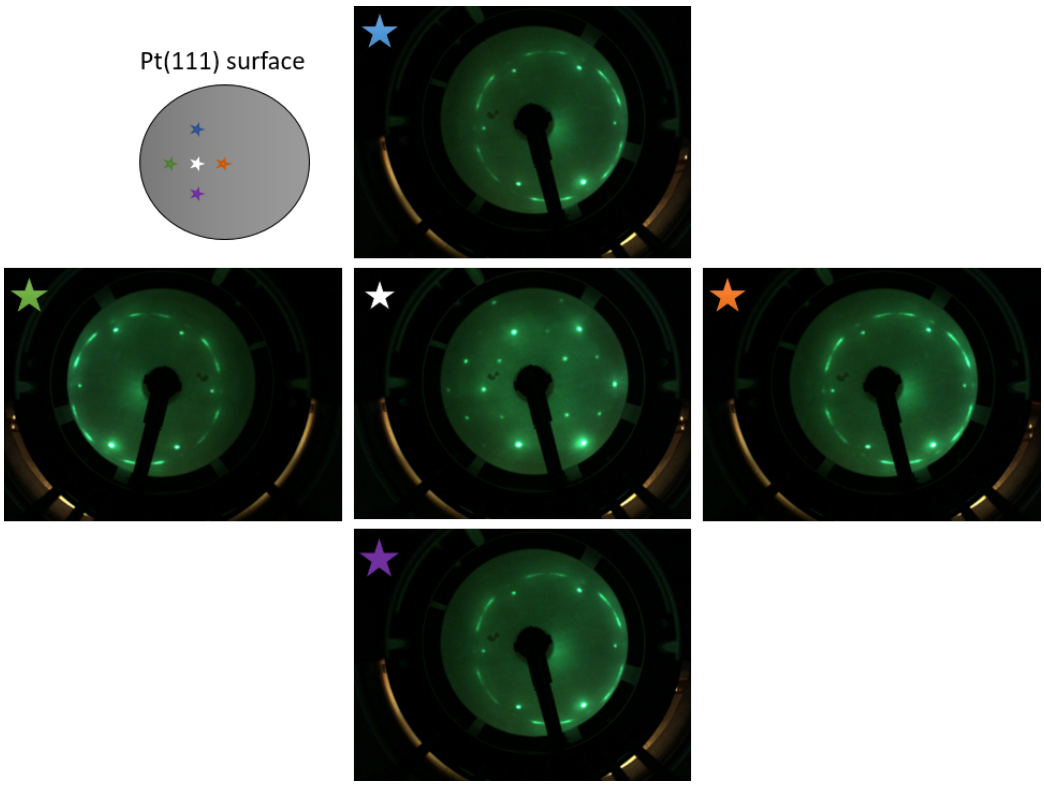

Figure 3.15: LEED images showing the local removal of the graphene by the molecular beam. The colored stars indicate the location of the LEED measurement on the surface. The white star in the middle is the point of the surface that is hit by the molecular beam. LEED images recorded at room temperature after scattering at $T_S = 1073\,\mathrm{K}$.

etching rate. When they locally heated the nozzle to increase the kinetic energy of the oxygen, the etching rates increased even further. This leads to the conclusion, that the kinetic energy of the NO molecular beam and the carrier gas play an important role in the destruction of graphene.

An additional case of graphene-damaging conditions was found during molecule-surface scattering experiments, when vibrationally excited NO($v = 3, J = 1.5$) was scattered from graphene. A spectrum of the NO($v = 2, 3$) bands is shown in Fig. 3.16, where panel A shows the data for 1% NO in H_2 and panel B for 1% NO in He. In both panels, the upper (black) spectrum is measured for scattering from freshly made graphene. The surface is then heated to 873 K with the molecular beam turned off during the heating phase. Afterwards, the surface is exposed to the molecular beam for 40 minutes and another spectrum of the NO($v = 2, 3$) bands is measured after letting the surface cool down (lower, red spectrum in both panels). The NO($v = 3$) region of both spectra does not change, but the $v = 2$ band changes in intensity for the hydrogen-seeded beam, whereas NO($v = 2$) is barely visible for the helium-seeded beam. The vibrational excitation of

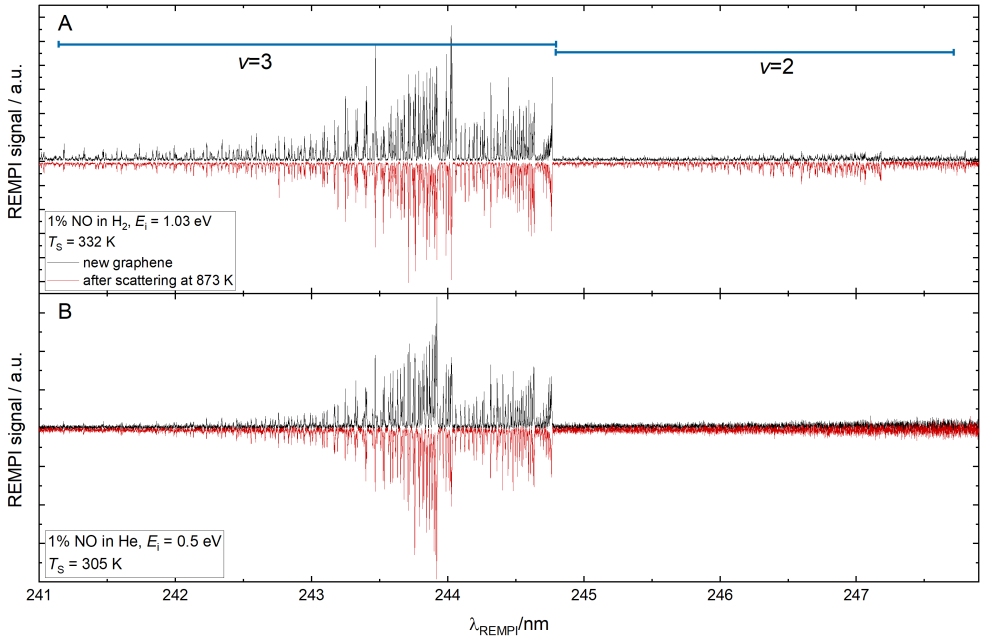

Figure 3.16: Spectra of the NO($v = 2, 3$) bands, recorded after scattering NO($v = 3, J = 1.5$) from freshly made graphene at 332 K (black, upper spectrum in both panels). Panel A shows the spectrum for 1% NO in H_2 and panel B for 1% NO in He. The red (lower) spectrum in both panels is also recorded at 332 K, but after scattering the molecular beam at $T_S = 873$ K for 20 minutes. In panel B, very little NO($v = 2$) is observed in both cases, while the amount of NO($v = 2$) drastically changes in panel A, indicating a change in the surface structure. No change in the LEED pattern was observed in both cases, indicating that the molecule-surface scattering is very sensitive to changes in surface structure. LEED on the other hand is not able to detect small changes if the periodicity of the whole lattice is not majorly damaged.

the molecules is assumed to have no effect on the graphene etching, because only a very small portion of the molecules impinging on the surface were excited to $v = 3$, and no etching was observed for the NO/He beams. As a consequence, this change in the spectra indicates a change in surface structure during the scattering process, which means that hydrogen is not a suitable carrier gas for these experiments as the integrity of the surface cannot be taken for granted.

4 Molecular beam surface scattering on graphene and graphite

4.1 Vibrational excitation of NO

This section focuses on the vibrational excitation of NO during the collision with Gr/Pt and HOPG. Looking for vibrational excitation of a diatomic molecule that is directly scatterd from a surface, is a good way to probe non-adiabatic effects. The excitation probability p_{exc} will scale strongly with the surface temperature and the normal kinetic energy, if the vibrational excitation mechanism involves non-adiabatic interactions, which has been observed, for example, for NO/Ag(111)[28] and NO/Au(111).[59] In contrast, for an adiabatic excitation mechanism, no surface temperature dependence of the excitation probability is expected in a direct collision event. The dependence of p_{exc} on the normal kinetic energy should also exhibit a threshold-behavior, which has been observed for NH_3/Au(111).[27] Vibrational excitation was observed, because efficient translation to vibration coupling was present in the system. Hence, the NO/Gr/Pt and NO/HOPG systems can be probed for non-adiabatic effects by looking for vibrational excitation during the collision.

Vibrational excitation probability

To determine the absolute vibrational excitation probabilities, the NO molecular beam was scattered from each surface at a range of different surface temperatures between 373 K and 873 K. No tagging laser was used and the REMPI laser was set to scan the NO($v = 1$) vibrational band. The vibrational distribution of the incoming beam equals a thermal distribution at room temperature, because vibrational cooling is very ineffective during a supersonic expansion.[95] Therefore, the incoming beam contains 99.99% NO($v = 0$) and 0.01% NO($v = 1$). If more than 0.01% NO($v = 1$) is present after the scattering, the molecules were vibrationally excited during the collision.

REMPI spectra for three different surface temperatures for the vibrational excitation of

NO on Gr/Pt(111) and Au(111) are shown in Figure 4.1. Increasing the surface temperature leads to two things: Firstly, the amount of NO($v = 1$) increases immensely over the range of the investigated surface temperatures. Secondly, for the NO/Gr/Pt(111) system, an increase in surface temperature also leads to higher rotational excitation (see the high J region between 233.5 nm − 234.5 nm).

As explained in Section 3.2.1, the gold surface was used as an internal calibration. Integration of the spectrum over the whole vibrational band gives the relative population. These values are corrected for the individual kinetic energy and angular distributions, and then scaled to the absolute vibrational excitation probabilities, that are listed in Reference [85]. The resulting vibrational excitation probabilities are shown in Figure 4.2 for Au(111) (black squares), Gr/Pt (red triangles) and HOPG (blue diamonds) for incidence translational energies of $E_\mathrm{i} = 0.49\,\mathrm{eV}$ (A) and $E_\mathrm{i} = 0.33\,\mathrm{eV}$ (B). The dashed blue line in Figure 4.2 indicates the thermal limit of vibrational excitation, which is the theoretical maximum value for complete equilibration between the surface and the NO. This limit is described by an Arrhenius-like function (Equation 4.1), where ΔE_vib is the vibrational energy spacing of NO($v = 0 - 1$), and A the pre-factor with $A = 1$.[96] The dash-dotted line indicates the thermal population of NO($v = 1$) at room temperature, which equals the population of $v = 1$ in the incoming beam.

$$p_\mathrm{exc} = A \exp\left[-\frac{\Delta E_\mathrm{vib}}{\mathrm{k_B} T}\right] \tag{4.1}$$

The vibrational excitation probability of NO/Gr/Pt shows a very strong dependence on the surface temperature similar to Au(111), without reaching the thermal limit. In contrast to NO/Au(111), the incidence translational energy only has a small effect on the vibrational excitation probability for NO/graphene scattering, especially at high surface temperatures (see Figure 4.3). For non-adiabatic interactions as for example in NO/Au(111), p_exc is affected stronger by E_i. For NO scattered from HOPG, there is no vibrational excitation observable. The amount of NO($v = 1$) stays constant over the whole investigated temperature range and is indistinguishable from the population in the incoming beam within the margin of error of the experiment. This stark difference between graphene and graphite is quite surprising, because the surfaces are nearly identical, only the substrate differs.

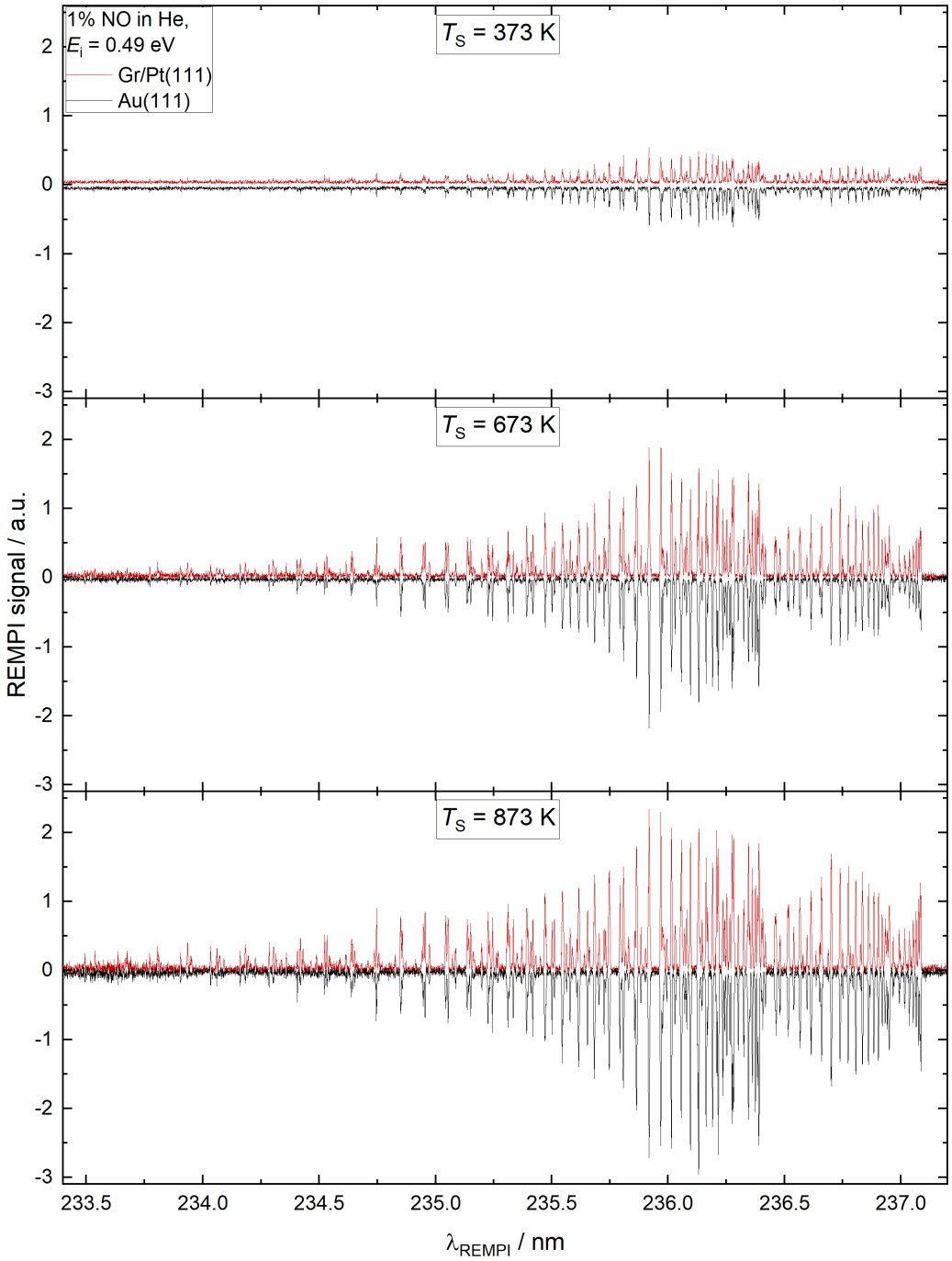

Figure 4.1: REMPI spectra of the NO($v = 1$) band for three different surface temperatures. The red curve shows the data for NO/Gr/Pt(111) and the black for NO/Au(111).

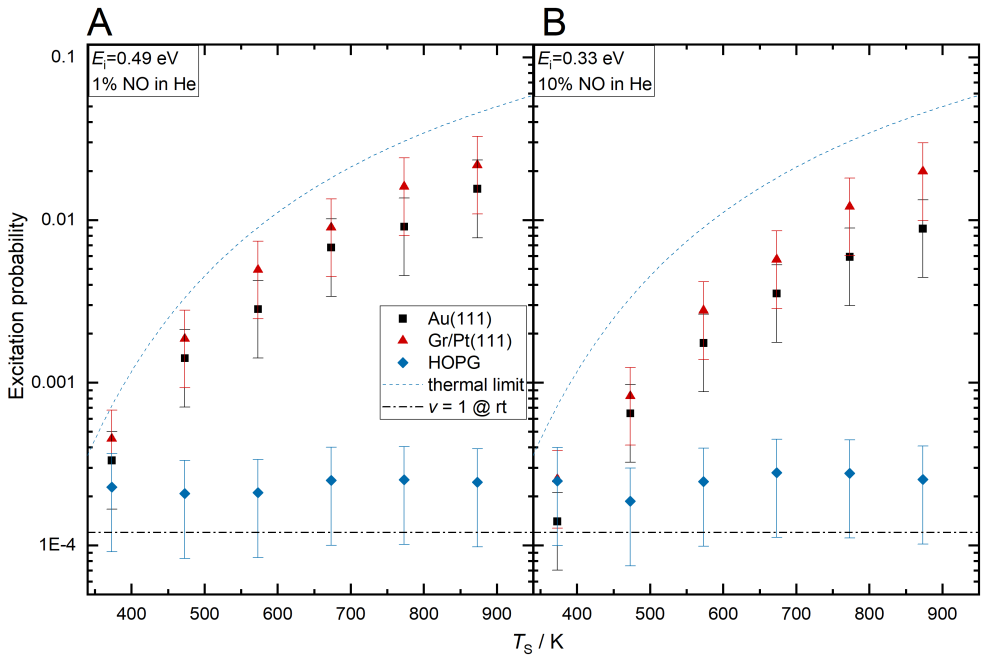

Figure 4.2: Vibrational excitation probabilities of NO scattered off of Au(111) (black squares), Gr/Pt (red triangles) and HOPG (blue diamonds). All values scaled to the values from ref. [85]. The dashed line indicates the thermal limit, i. e. complete equilibration of the degrees of freedom of NO with the surface and the dash-dotted line indicates the NO($v = 1$) population in the incoming beam (thermal population at room temperature). The vibrational excitation probability for NO/Au scattering clearly depends on the incidence translational energy of the NO. This effect is very weak for NO/Gr/Pt and the vibrational excitation probability for both incidence energies is higher than for NO/Au. For both surfaces, increasing the surface temperature drastically increases the excitation probability. On HOPG, no vibrational excitation is observed, the amount of scattered NO($v = 1$) is independent of the incidence energy as well as the surface temperature.

Rotational distribution

The rotational state distributions of NO($v = 1$) scattered from Gr/Pt and HOPG can be fit very well with a Boltzmann distribution. A few exemplary Boltzmann plots of the rotational state distribution are shown in Figure 4.4. In the logarithmic plot, the rotational state distributions show a single linear behavior for Gr/Pt and HOPG without any indications pointing to special effects like rotational rainbows or rotational state dependent trapping probabilites. Rotational rainbows have been observed for the NO/Ag(111) system,[97,98] and a dependence of the trapping probability on the rotational excitation for the NO/Pt(111) system.[99,100] In both cases, a Boltzmann plot of the rotational distribution deviates from a single linear behavior, which can be seen in Figure 4.5 on the example of NO/Pt(111).

The resulting rotational temperatures as a function of surface temperature are shown in Figure 4.6. The rotational temperatures for the NO/Au(111) (black circles) and NO/HOPG

systems (blue triangles) are independent of the surface temperature, which is known to indicate a direct scattering mechanism.[39,40,85] In the case of NO/Au(111), the scattering is vibrationally inelastic. Not only are the molecules rotationally excited during the surface collision, but also the excitation of the first vibrational level is caused by a non-adiabatic interaction with the electrons of the surface.[85,96] For NO on HOPG, the scattering process is vibrationally elastic, but rotationally inelastic. The rotational temperature of $T_{\mathrm{rot}} \approx 200\,\mathrm{K}$ agrees well with the findings of Frenkel *et al.* They investigated the rotational distribution of NO scattered from graphite and found rotational temperatures of $T_{\mathrm{rot}} \approx 250\,\mathrm{K}$ in the same temperature range as the current experiments.

In case of trapping desorption, the molecules coming off the surface have had enough time to reach equilibrium with the surface. As a consequence, the rotational temperature of the molecules should match the surface temperature (indicated by the dotted line in Figure 4.6), which is the case for the NO/graphene system (red triangles). This of course is only true, if the trapping probability is independent of the rotational state, which seems to be the case, as no deviations from a rotational Boltzmann distribution were observed. For the two lowest surface temperatures investigated ($T_{\mathrm{S}} = 373\,\mathrm{K}$ and $T_{\mathrm{S}} = 473\,\mathrm{K}$), the rotational temperature is independent of the surface temperature for NO on Gr/Pt(111).

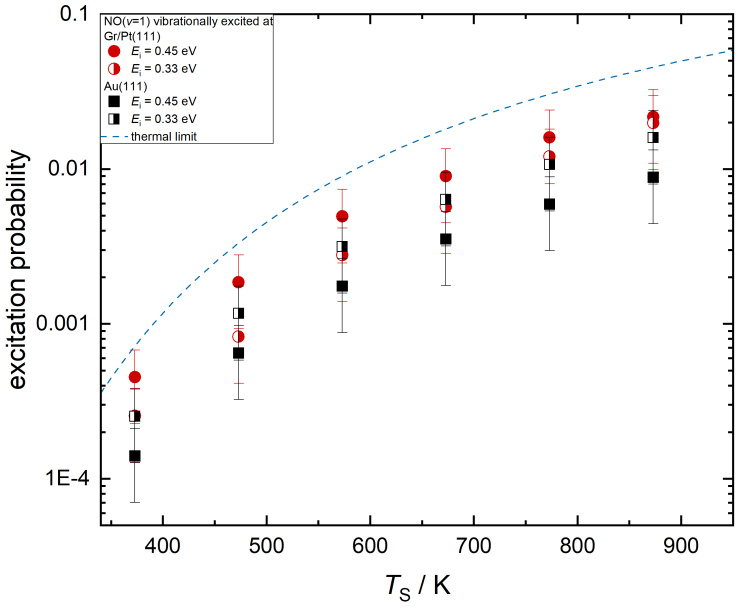

Figure 4.3: Comparison of the absolute vibrational excitation probabilities of NO scattered from Gr/Pt and Au(111) for two incidence kinetic energies. The kinetic energy of the nitric oxide only has a small effect on the excitation probability for Gr/Pt. This difference decreases with increasing surface temperature. For NO(Au(111), the influence of the kinetic energy on the excitation probability does not depend on the surface temperature.

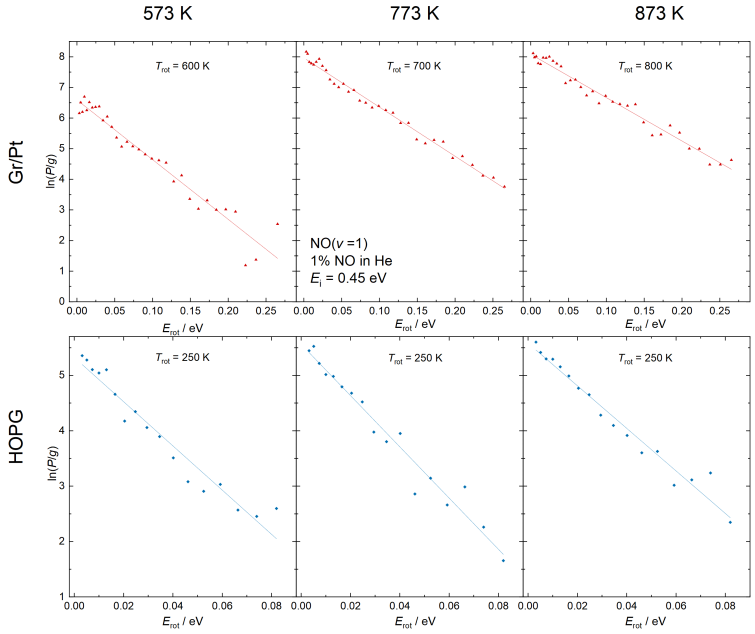

Figure 4.4: Exemplary rotational Boltzmann plots for three different surface temperatures with $E_i = 0.49\,\text{eV}$ for NO scattered from Gr/Pt (top row) and HOPG (bottom row). The rotational distributions can be described very well with a thermal Boltzmann distribution and show no evidence of rotational rainbows.[97,98] For NO on graphene, the calculated rotational temperatures also agree reasonably well with the surface temperature, which can be taken as a sign of a trapping-desorption scattering mechanism, whereas the rotational temperature for NO on HOPG is constant. Note the different scaling of the energy axis for Gr/Pt and HOPG.

The vibrational excitation probability is very low at low T_S, especially at $T_S = 373\,\text{K}$. As a result, the deviation can be explained with a difference in scattering mechanism. In this case, the NO($v = 1$) that is present in the incoming beam is directly scattered from the surface and gets rotationally excited during the collision, leading to the deviation from the linear trend. As the surface temperature increases, the amount of vibrationally elastically scattered NO($v = 1$) becomes insignificant with respect to the molecules that are vibrationally excited at the surface, hence it does not influence the determined rotational temperatures.

The rotational state distributions of NO scattered from Gr/Pt and HOPG show a completely different behavior, similar to the observations from the vibrational excitation probability. In this case, the rotational state distributions indicate a difference in scattering mechanism for both surfaces. While the NO is directly scattered from HOPG, a trapping-desorption mechanism seems to cause the vibrationally excited NO during the collision with Gr/Pt. To gain further insights on the scattering mechanism, angular distributions were investigated for both surfaces.

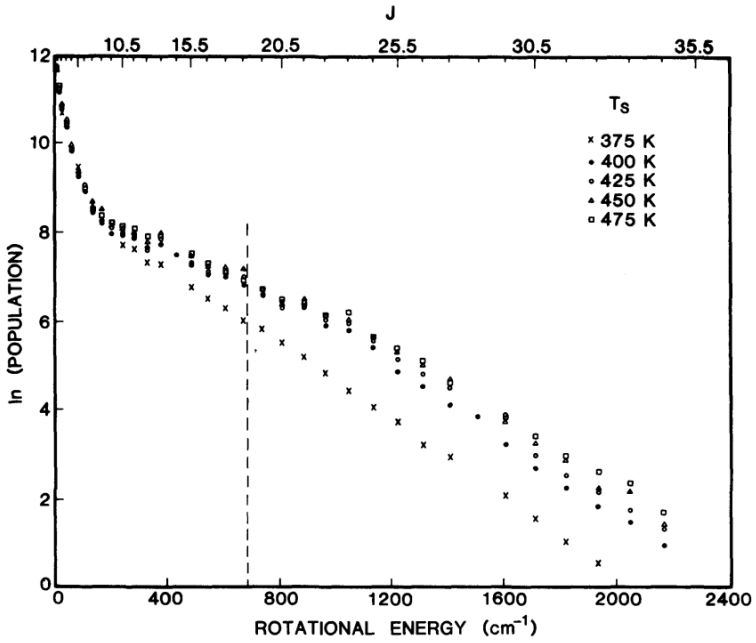

Figure 4.5: Boltzmann plot of the rotational state distribution for NO scattered from Pt(111). For this system, rotationally dependent trapping probabilities were observed, which lead to a deviation from a single straight line. Reprinted with permission from reference [100]. Copyright (1989) by the American Institute of Physics.

Angular distribution

Figure 4.7 shows the angular distributions of NO($v = 1$) scattered from Gr/Pt in red and HOPG in blue. As discussed before, the scattered NO($v = 1$) is a result of vibrational excitation at the surface for Gr/Pt. On HOPG, it is the NO($v = 1$) in the incoming beam that is vibrationally elastically scattered from the surface. The angular distributions were measured at a surface temperature of $T_S = 773\,\mathrm{K}$ for incidence translational energies of $E_i = 0.49\,\mathrm{eV}$ (panels A and C of Figure 4.7) and $E_i = 0.33\,\mathrm{eV}$ (panels B and D) by moving the REMPI laser parallel to the surface, as described in section 3.2.3. The angular distributions for NO scattered from HOPG are narrow, while the angular distributions for NO scattered from Gr/Pt are very broad. For $E_i = 0.49\,\mathrm{eV}$, the angular distribution agrees well with a $\cos(\beta)$ distribution, which is indicated by the dashed pink line. For $E_i = 0.33\,\mathrm{eV}$, the angular distribution of NO/Gr/Pt does not agree with the $\cos(\beta)$ distribution, but is still a lot broader than for NO/HOPG, and the angular resolution is for these measurements is 10°.[56] For a trapping-desorption mechanism, a $\cos(\beta)$ angular distribution about the surface normal is expected, because the molecules desorbing from the surface are treated like an effusive source of molecules.[89] For a direct scattering mechanism, a narrow angular distribution that peaks at the specular angle, similar to those

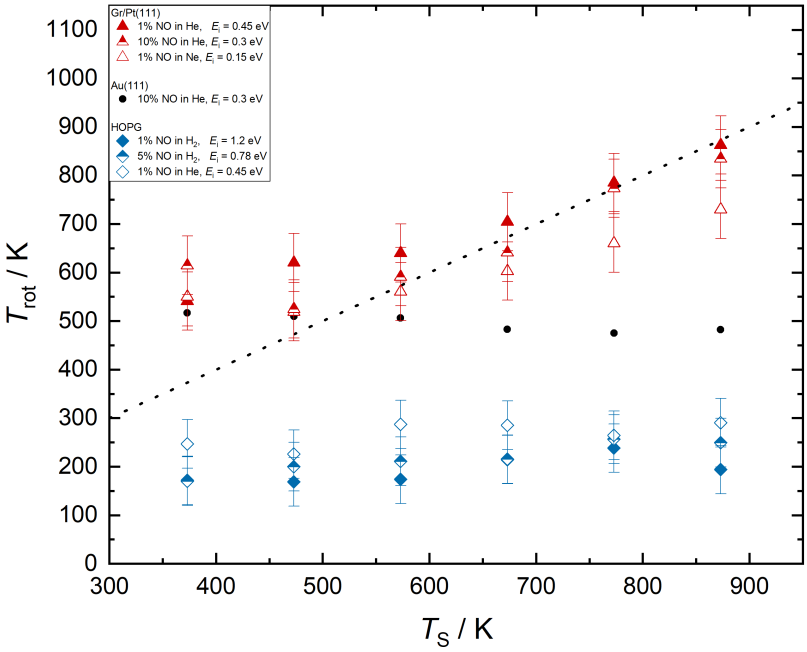

Figure 4.6: Rotational temperatures of NO scattered from Au(111) (black circles), Gr/Pt(111) (red triangles) and HOPG (blue diamonds) for different incidence kinetic energies. All rotational temperatures for NO($v = 1$). The dotted line is a guide to the eye with a slope of unity, meaning the rotational temperature equals the surface temperature. For NO/Au(111) and NO/HOPG the rotational temperature is independent of the surface temperature. In case of HOPG T_{rot} is independent of the incidence energy as well. This is a sign of a direct scattering mechanism. For NO/Gr/Pt, the rotational temperature increases linearly with increasing surface temperature, which is a sign of equilibration between the surface and the rotational degrees of freedom of the NO and indicates trapping desorption. For the lowest surface temperature, T_{rot} deviates from this trend.

observed for NO/HOPG is expected, because the parallel momentum of the molecules is conserved during the collision. Note that the peak position of the angular distributions changes for the different incidence translational energies, because the chamber had to be opened for repairs the measurements. During the repairs, the tilt of the surfaces in the lab-frame changed, resulting in different peak positions of the angular distributions.

The scattering mechanisms predicted by the rotational state distributions agree with the observations from the angular distributions. NO scattered from HOPG shows a narrow angular distribution that peaks at the specular angle, which indicates a direct scattering process. On the contrary, scattering NO from graphene leads to broad angular distributions, indicating a trapping desorption scattering mechanism.

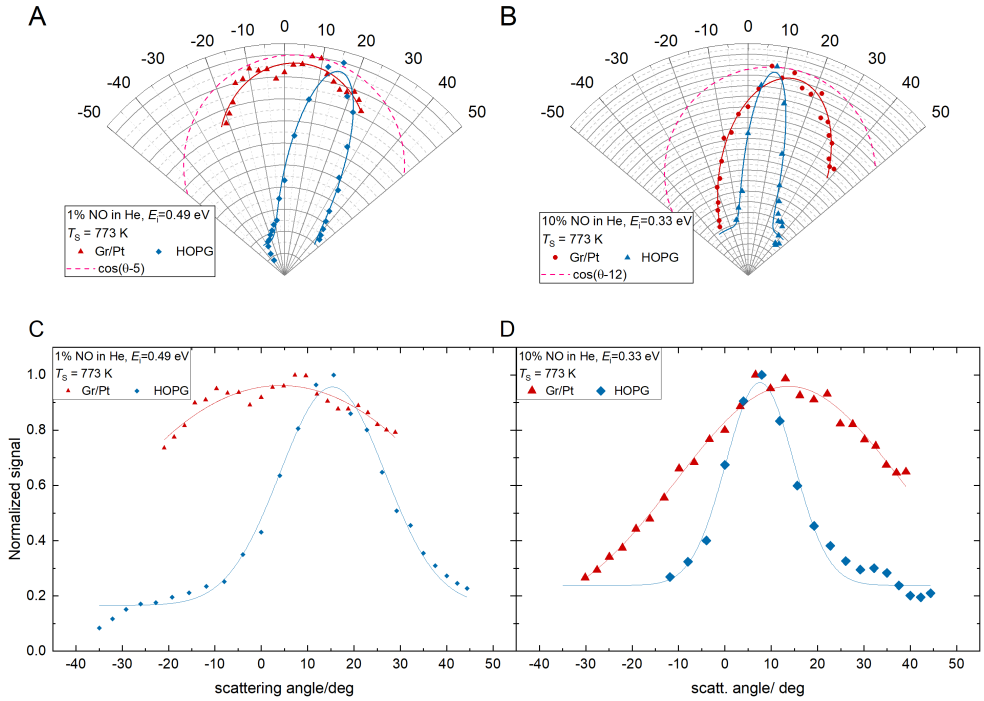

Figure 4.7: Angular distributions of scattered NO($v = 1, J = 8.5$) from Gr/Pt (red triangles) and HOPG (blue diamonds) fitted with a gaussian function for two different incidence translational energies - $E_i = 0.49$ eV (A,C) and $E_i = 0.33$ eV (B,D). The angular disitributions for NO/HOPG are very narrow, which is in agreement with a direct scattering mechanism. For NO on graphene, the angular disitributions are very broad and agree relatively well with a $\cos(\beta)$ distribution that is expected for a trapping desorption mechanism. The peak position changes for different incidence translational energies because the chamber was opened for repairs in between the measurements, hence the surfaces are tilted at a different angle. The angular resolution is about 10°. [56]

State to state time of flight

To better understand the scattering mechanism responsible for the vibrational excitation of NO on Gr/Pt, state to state time of flight measurements were carried out. The scattered NO($v = 1$) was tagged by the IR laser to NO($v = 3$), which was then detected.[59,88,101] See Figure 4.8 for a sketch of the detection geometry. The used transitions for the IR and the REMPI laser are listed in Table 3.3. Exemplary time of flight data is shown in Figure 4.9 for two different incidence translational energies at two different surface temperatures. NO($v = 1, J = 8.5$) was tagged for these measurements. The fit (red line) shows a Maxwell-Boltzmann-distribution fixed at the surface temperature and agrees well with the data. The agreement of the data with a thermal distribution fixed to T_S is expected for molecules equilibrated with the surface. This is a sign of trapping desorption, if detailed balance does not need to be taken into account. That is, if the trapping probability is

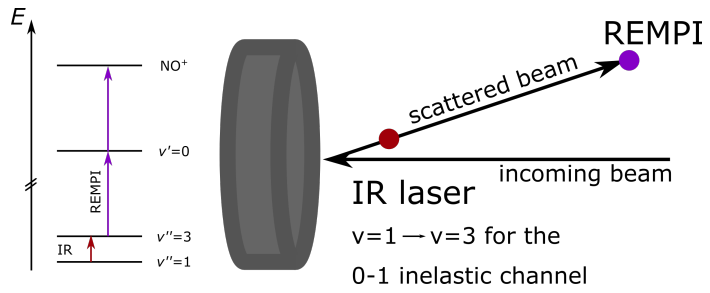

Figure 4.8: Sketch of the tagging geometry used for the state to state time of flight measurements of the vibrationally inelastic scattering channel. A single rotational state of the scattered NO($v = 1$) was tagged to NO($v = 3$) by the IR laser. The NO($v = 3$) was then detected using REMPI, as shown in the energy diagram on the left.

independent of the incidence conditions of the molecules.

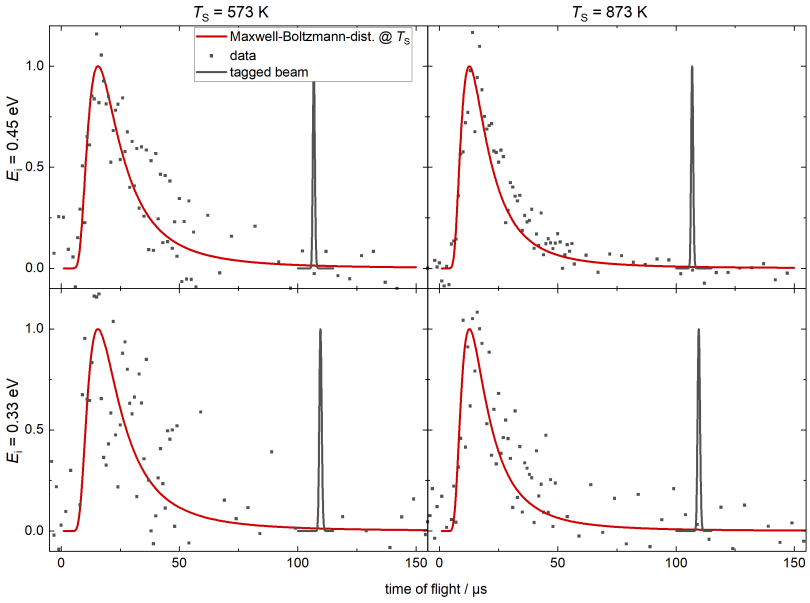

Figure 4.9: State-to-state time of flight measurements of NO($v = 1, J = 8.5$) scattered from Gr/Pt. The fit (red line) is a Maxwell-Boltzmann-distribution fixed at the surface temperature and agrees very well with the data, meaning the molecules thermalize with the surface during the scattering, which indicates a trapping-desorption mechanism. It is assumed that the trapping probability is independent of the kinetic and rotational energy of the molecule. The black line shows the width of the tagged molecules to indicate the resolution.

Summary

Scattering nitric oxide from HOPG revealed no vibrational excitation under the applied experimental conditions. The thermal population of NO($v = 1$) in the incoming beam is vibrationally elastically scattered from HOPG following a direct scattering mechanism.

The rotational temperature of the scattered NO($v = 1$) is independent of the surface temperature and narrow angular distributions are observed for two incidence kinetic energies. Both of these findinds support the idea of directly scattered molecules.

These observations are drastically different for NO/Gr/Pt, where thermal vibrational excitation of NO($v = 1$) during the collision was observed. The amount of NO($v = 1$) strongly depends on the surface temperature, similar to the rotational state distribution. The rotational temperature increases linearly with increasing surface temperature (except for $T_S < 500\,\mathrm{K}$), and the angular distributions are broad. These observations indicate a trapping-desorption scattering mechanism, which was supported by the state to state time of flight measurements. A thermal speed distribution of the scattered NO($v = 1$) is observed that matches the surface temperature. No sign of detailed balancing could be found for the rotational or the kinetic energy distributions, which means the trapping probability is independent of these two. No signs of a direct mechanical energy transfer from translational to vibrational energy (T–V energy transfer) similar to the vibrational excitation of NH_3 on Au(111)[27] was observed. Similarly, no evidencec of non-adiabatic energy transfer from the surface to the NO was found, because the NO($v = 1$) signal is dominated by trapping desorption, while both of these mechanisms are possbile for directly scattered molecules.

4.2 Translational inelasticity of NO

In the last chapter, a large difference in the scattering mechanism of NO from graphene and graphite was observed. NO is directly scattered from HOPG, and no vibrational excitation was observed. In contrast, the vibrational excitation that was observed for NO scattered from Gr/Pt is the result of a trapping desorption mechanism. Enhanced sticking of gas molecules on graphene would make it an interesting substrate for catalysts. The reaction rates could be increased, because molecules easily stick to the surface and then diffuse to the catalytically active site, where they react and desorb. To gain further insight into the enhanced sticking probability of graphene, the translational inelasticity of NO scattered from Gr/Pt and HOPG was investigated using state to state time of flight experiments.

In the first part, the scattering of vibrationally excited NO($v = 3$) will be discussed. Only the vibrationally elastic channel will be considered, because no vibrational relaxation to $v = 2$ or $v = 1$ was observed (see lower panel of Figure 3.16). The advantage of this scattering channel is that it is background free, because no NO($v = 3$) is present in the

incoming molecular beam. In the second part, vibrationally elastic scattering of NO(v = 0) from Gr/Pt will be discussed. The results will then be compared to the findings of Greenwood *et al.*, who found a translational energy loss of ground state NO scattered from graphene on gold of up to 80%, but no signs of trapping.[17] A translational inelasticity of this magnitude could reveal further information on why NO sticks on graphene but not on graphite.

4.2.1 Vibrationally excited NO

A sketch of the tagging setup used for the vibrationally elastic scattering of NO(v = 3) is shown in Figure 4.10. The incoming NO molecules are tagged 1 mm in front of the surface by the IR laser to NO(v = 3, J = 1.5). After scattering, the five different rotational states of NO(v = 3) shown in Figure 4.10 are investigated to gather information about the coupling between rotation and translation. For the used transitions, see Table 3.3.

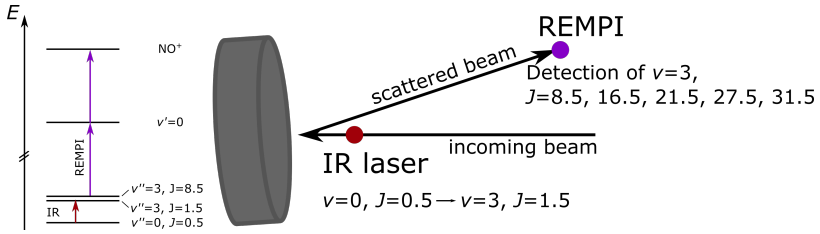

Figure 4.10: Sketch of the tagging geometry used for the state to state time of flight measurements of the vibrationally elastic scattering channel. The incident NO(v = 0, J = 0.5) was tagged via the R(0.5) transition to NO(v = 3, J = 1.5) by the IR laser. Different J-states of the scattered NO(v = 3) were then detected using REMPI.

Translational inelasticity

Panels (a) and (b) of Figure 4.11 show exemplary time of flight data and the corresponding fits using equation 4.2 for scattered NO(v = 3, J = 8.5) scattered from Gr/Pt and HOPG, respectively.

$$S(t) = A\left(\frac{l}{t}\right)^3 \exp\left[-\left(\frac{v - v_0}{\alpha}\right)^2\right] l^{-1} \tag{4.2}$$

Here, A is a scaling factor, t the time of flight, l the length of the flight path, v the velocity, v_0 the center velocity and α the width of the distribution.[81,88,101] The fitting paramters are listed in Table 4.1. The fit described both sets of data very well, with v_0 being non-zero, indicating a direct scattering mechanism. Comparing both sets of data, it is obvious that

the time of flight distributions for NO/HOPG are a lot narrower compared to their counterparts of NO/Gr/Pt, which is reflected in the values of α. v_0 is also higher for NO/HOPG, indicating faster scattered molecules. However, it is hard to compare the time of flight data directly, because the flight distance l is different for Gr/Pt and HOPG due to the way the surfaces are mounted. Figure 4.11 c shows the same fits converted into energy space, red for NO on graphene and blue for NO on HOPG. Similar to the observation from the time of flight data, the energy distributions of NO/HOPG are a lot narrower and the final translational energy is higher compared to NO/graphene. For the slowest incidence energy of 0.11 eV, a significant part of the NO molecules are scattered with a translational energy greater than the incidence one, which is shown in black. This is likely caused by thermal motion of the surfce, because it depends strongly on the surface temperature, but it is not observed on HOPG.

Table 4.1: The fitting parameters of the time of flight fits shown in Figure 4.11. NO($v = 3, J = 8.5$) was detected after scattering NO($v = 3, J = 1.5$) from the surface. Data is fitted with Equation 4.2. v_0 is the center velocity and α the spread of the distribution.

		Gr/Pt(111)		HOPG	
E_i/eV	T_S/K	v_0/ms^{-1}	α/ms^{-1}	v_0/ms^{-1}	α/ms^{-1}
0.49	873	466	505	843	344
	573	508	435	835	329
	373	487	386	852	305
0.33	873	413	456	707	274
	573	439	390	637	301
	373	448	332	620	286
0.11	873	388	328	455	189
	573	333	293	423	183
	373	293	268	396	174

The final translational energy distributions shown in Figure 4.11 only show the data for a single ro-vibrational state of NO. Since five different rotational states were investigated, the kinetic energy of the scattered NO can be plotted as a function of the rotational energy, which is shown in Figure 4.12 for three different surface temperatures. Under all conditions, an anti-correlation between the final translational and the rotational energy is

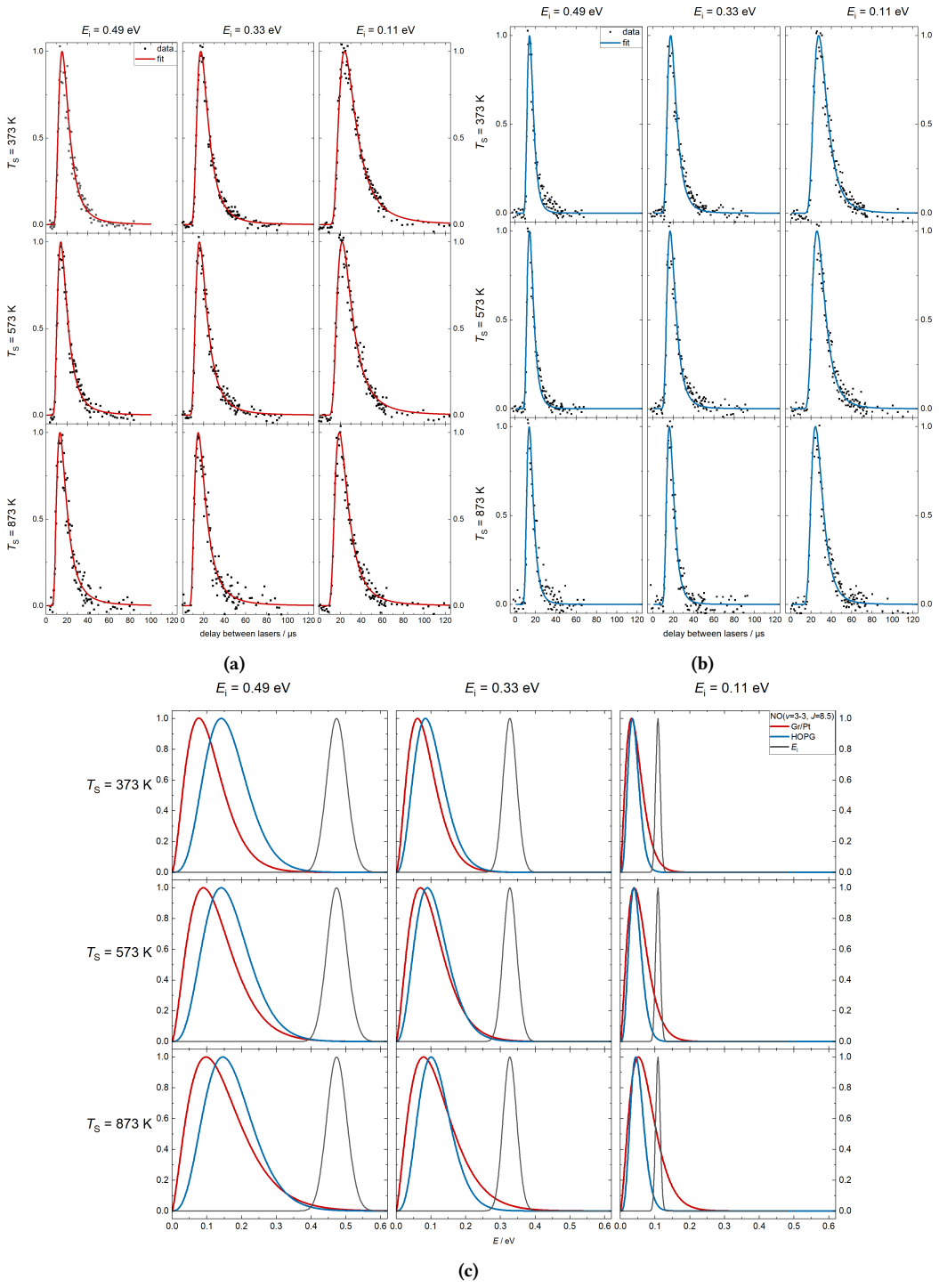

Figure 4.11: Time of flight data for scattered NO($v = 3, J = 8.5$) scattered from Gr/Pt (a) and HOPG (b) the fits for three different incidence energies at three different surface temperatures. (c) Corresponding energy distributions of the NO scattered from Gr/Pt (red) and HOPG (blue). The incidence energy distribution is shown in black. The final energy distributions for NO/HOPG are narrower and lose less translational energy than on Gr/Pt. At high surface temperatures and low incidence energies, a fraction of the NO molecules scattered from graphene gain translational energy.

observed, meaning that higher rotational excitation during the collision leads to a slower kinetic energy. This translation to rotation coupling will be discussed in the next section.

For the highest incidence kinetic energy of $E_i = 0.49\,\text{eV}$, the NO loses more energy when scattered from graphene on platinum, independent of the final rotational state. For $E_i = 0.33\,\text{eV}$, the energy loss is similar on both surfaces, whereas for $E_i = 0.11\,\text{eV}$, the NO loses more translational energy on HOPG than on graphene. During the collision with graphene, a significant number of molecules gain kinetic energy from the surface, and scatter with higher energies than the incoming beam, as can be seen in Figure 4.11 c. Hence, the energy distribution of the scattered NO gets a lot broader, which causes a higher mean final energy. This energy gain is only visible for the lowest incidence energy on graphene, but not on graphite.

Extrapolating the final translational energy to $E_{rot} = 0\,\text{eV}$ allows for a comparison of the mean final translational energy without any rotational contribution. Figure 4.13 shows this dependence of the mean final translational energy of NO scattered from graphene and graphite. The final translational energy is dependent on the incidence kinetic energy (also shown in Figure 4.14), which is a sign of a direct scattering mechanism, because the molecules don't lose information about the conditions prior to the collision, which happens during trapping (and the following equilibration) on the surface. Translational energy transfer to the surface is very efficient for both surfaces, as the molecules lose a majority of their kinetic energy during the collision. Moreover, Figure 4.13 shows a

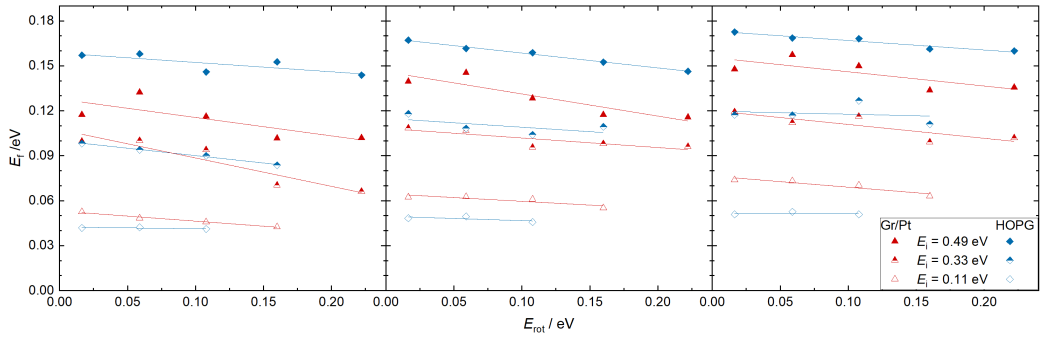

Figure 4.12: Final translational energy as a function of the surface temperature for three different surface temperatures and incidence energies for Gr/Pt (red triangles) and HOPG (blue diamonds). For both surfaces, the final translational energy decreases approximately linearly with increasing rotational energy, which can be assigned to a transfer of translational to rotational energy during the surface collision. The linear fits are used for extrapolation to $J = 0$ to view the dependence of the final translational energy on the surface temperature without any rotational influence. See Fig. 4.13.

surface temperature dependence of the mean final energy that is more pronounced on graphene than on graphite. Assuming a linear dependence of E_i on T_S and fitting the

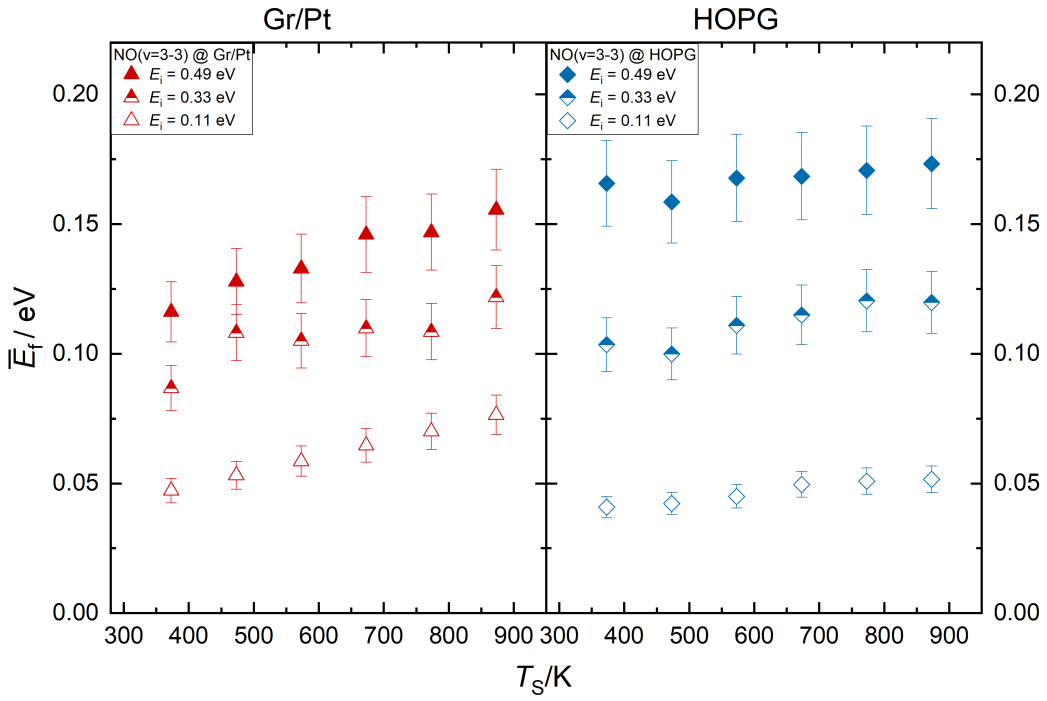

Figure 4.13: Mean final translational energy of NO scattered from Gr/Pt (left) and HOPG (right) as a function of the surface temperature. All values for E_f are shown without any rotational contribution (see text for explanation). The final translational energy is dependent on the incidence energy, a sign of direct scattering. E_f is higher for NO/HOPG and the dependence of the mean final translational energy on the surface temperature is a lot smaller for HOPG than for Gr/Pt.

data, the slopes are 64 µeV/K for graphene and 30 µeV/K for HOPG. Using the slope as an indication, the effect of the surface temperature on the final translational energy is twice as large on graphene than on graphite.

Comparing the dependence of the mean final translational energy as a function of the incidence energy (Figure 4.14) with the prediction made by the Baule limit,[58] which describes the scattering based only on the mass ratio of the molecule and the surface (collision of two hard spheres), shows that the Baule limit predicts the correct slope for scattering from HOPG, when a surface mass of 108 u is assumed. This mass equals eleven carbon atoms, and although the slope is correct, the mean final translational energy is always underestimated. In contrast, the predictions of the Baule limit don't match the NO/Gr data. No effect of the surface temperature on the slopes $\Delta\bar{E}_f/\Delta E_i$ is observed. Similar to the observations from Figure 4.13, the surface temperature has a stronger effect on the final kinetic energy for Gr/Pt than for HOPG.

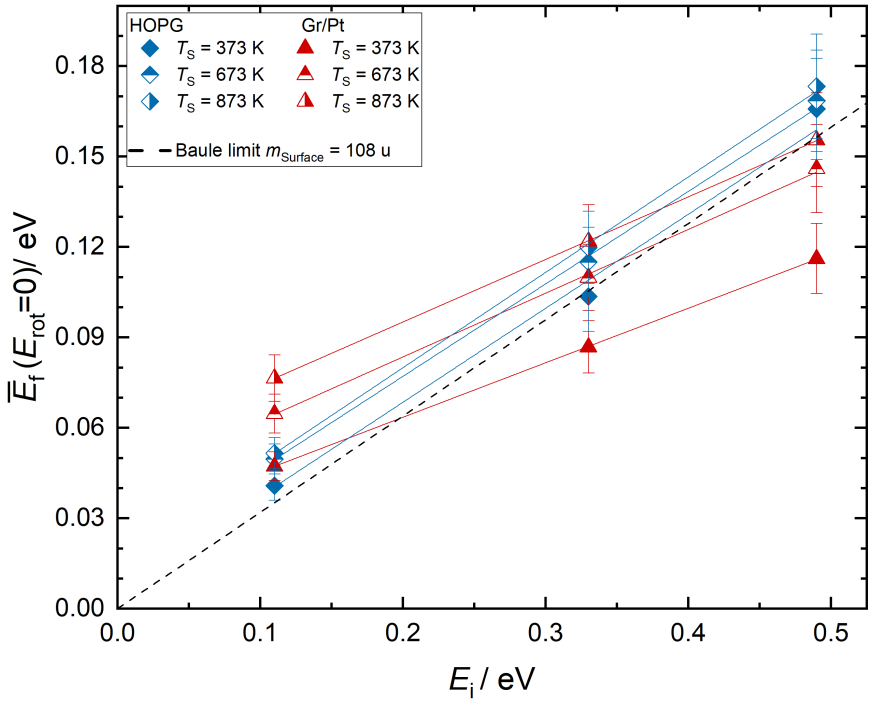

Figure 4.14: Mean final translational energy as a function of the incidence energy for Gr/Pt (red triangles) and HOPG (blue diamonds) for the 3–3 scattering channel. The black dashed line indicates the prediction of the Baule model for a surface mass of 108 u, which equals eleven carbon atoms.

Translation–rotation-coupling

To investigate the coupling of translational and rotational degrees of freedom, five different rotational states were investigated. The dependence of the mean final translational energy on the rotational energy is shown in Fig. 4.12 for three different surface temperatures and incidence translational energies for graphene (red) and HOPG (blue). As stated earlier, an anti-correlation of translation and rotation is observed, meaning that for increasing rotational excitation a slower translational energy is observed.

Kimman *et al.*[102] and Golibrzuch *et al.*[59] investigated the translation to rotation coupling (T–R-coupling) for NO scattered from Ag(111) and Au(111), and observed an anti-correlation between the mean final translational and the rotational energy. They interpreted the slopes $\Delta\overline{E}_f/\Delta E_{rot}$ as the T–R-coupling strength and gave two limiting cases: If $\Delta\overline{E}_f/\Delta E_{rot} \rightarrow -1$, all of the energy required for rotational excitation of the molecules during the collision is taken from the translational energy. This would be expected for a purely mechanical collision with a stiff surface and means that $E_f + E_{rot} = \text{const}$. For $\Delta\overline{E}_f/\Delta E_{rot} \rightarrow 0$, the incidence translational energy does not have any effect on the rotational excitation, all of the energy is taken from the surface, leading to $E_{Surface} + E_{rot} =$

const.

Figure 4.15 shows the slopes taken from Figure 4.12 for four different surface temperatures. Data for vibrationally elastic scattering of NO($v = 3$) from Au(111) is also shown as a comparison and is taken from Reference [56]. This data is identical with the ones referenced earlier from Reference [59]. For Gr/Pt and HOPG, the values are close to zero, with $-0.15 < \Delta\overline{E}_f/\Delta E_{rot} < 0$. Hence, the majority of the rotational excitation comes from the surface and not from the incidence translational energy. The contribution of the incidence translational energy on the rotational excitation decreases with decreasing incidence energy, and for graphite, increasing the surface temperature has the same effect. For graphene on platinum, no surface temperature dependence of the T–R-coupling strength is visible within the experimental accuracy.

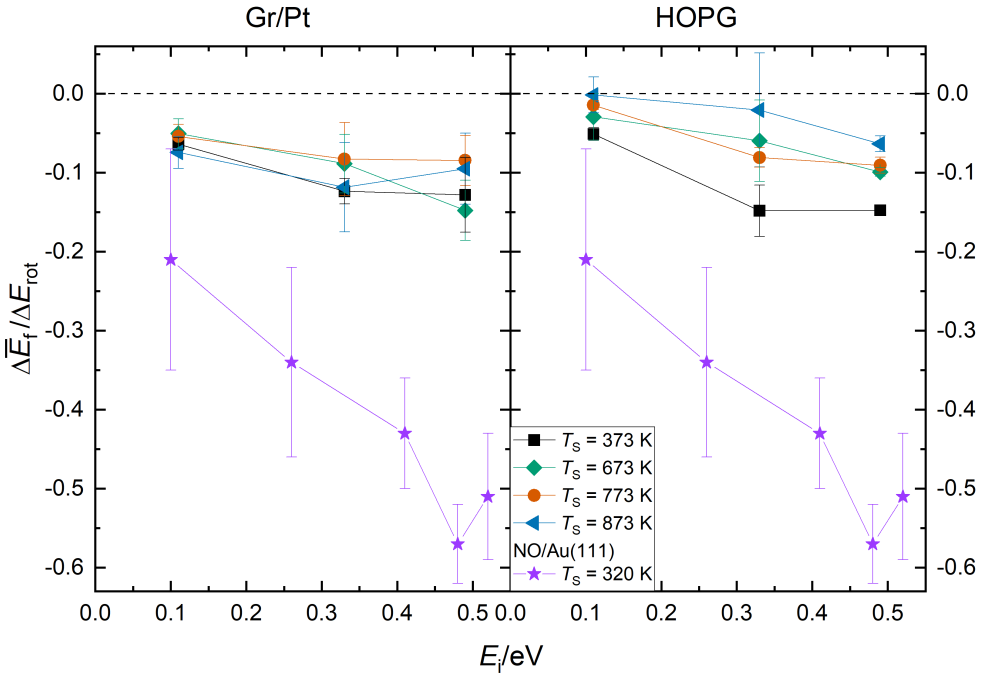

Figure 4.15: The slopes $\Delta\overline{E}_f/\Delta E_{rot}$ taken from Figure 4.12 as a function of the incidence energy for Gr/Pt (left) and HOPG (right), representing the energy transfer efficiency from translation to rotation. The purple stars show the values for vibrationally elastic scattering of NO($v = 3$) from Au(111) and were taken from Reference [56].

Scattering NO from Au(111) revealed slopes in the range of $-0.6 < \Delta\overline{E}_f/\Delta E_{rot} < -0.2$ for vibrationally elastic scattering of $v_i = [3, 11]$,[32,59] which means that the incidence translational energy plays an important role in the rotational excitation. $\Delta\overline{E}_f/\Delta E_{rot}$ strongly depends on the incidence kinetic energy and decreases by a factor of three from $E_i = 0.5$ eV to $E_i = 0.2$ eV (-0.6 to -0.2), which is similar to Gr/Pt and HOPG (both from -0.15 to -0.05) at the closest surface temperature of $T_S = 373$ K. The large difference in coupling strength

compared to graphene and graphite can be explained by the different surface mass. In a purely mechanical picture, a surface with a significantly larger mass will behave more stiff than a surface with a lower mass than the impinging molecule, and a softer surface will in turn ”buffer” the translational energy, instead of transferring it into rotational excitation.

Summary

The translational inelasticity of vibrationally elastically scattered NO($v = 3$) has been investigated. Only direct scattering was observed for both surfaces, with no signs of trapping desorption. Scattering NO from graphite results in narrower energy distributions with less energy loss than on graphene. For the lowest incidence kinetic energy, a fraction of the NO molecules gain kinetic energy during the scattering process. This effect strongly increases with increasing surface temperature. The effect of the surface temperature on the final translational energy only differs by a factor of two between graphene and graphite, and the T–R coupling is also quite similar. Considering the fact that NO sticks on graphene but not on graphite, as observed during the vibrational excitation experiments, this small difference is quite surprising.

Moreover, non-adiabatic interactions for the NO/Gr system seem highly unlikely considering these results. If non-adiabatic effects were present, vibrational relaxation to $v = 2$ or $v = 1$ should be observable, but no NO in lower vibrational states was found. A very efficient non-adiabatic interaction could cause complete relaxation to the vibrational ground state. However, this would result in no vibrationally elastically scattered NO($v = 3$), because all the molecules relaxed.

4.2.2 Ground state NO

When vibrationally excited NO($v = 3$) is scattered from a surface, a few things can happen. First, the molecules can scatter in a vibrationally elastic manner. Second, vibrationally inelastic scattering can take place, which means that the NO loses some or all of its vibrational energy during the collision, which, for example, has been observed for NO/Au(111) scattering,[59,101] but not for NO/Gr or NO/HOPG. Third, the molecules can trap at the surface and then scatter back, most likely completely equilibrated with the surface. As a result, it is unlikely to observe NO($v = 3$), because NO($v = 3$) will not be significantly populated for the investigated temperature range.[1] However, this changes,

[1] However, it should be noted that vibrational lifetimes on the order of $1 \cdot 10^{-10}$ s have been reported for CO on Au(111).[103] As a result, some vibrationally excited molecules might survive a trapping desorption process.

when NO in its vibrational ground state is scattered from a surface, because the majority of the molecules will be in $v = 0$ for both trapping desorption and direct scattering. As a result, the vibrationally elastic scattering of ground state NO from Gr/Pt should consist both of direct and trapping desorption scattering. Direct scattering has been discussed in the previous chapter, and trapping-desorption of NO on graphene has already been observed in the vibrational excitation of NO, and has been analyzed in section 4.1. No sign of trapping was observed for HOPG, hence the 0–0 channel was not investigated.

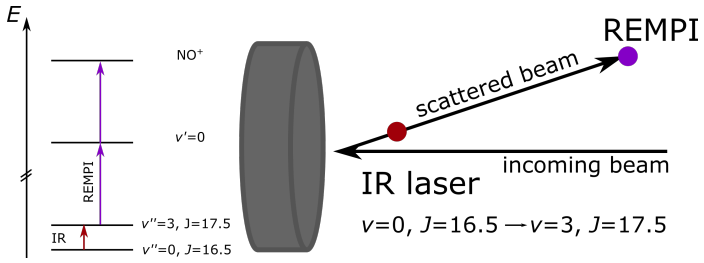

Figure 4.16: Sketch of the tagging geometry used for the state to state time of flight measurements of the vibrationally elastic scattering channel. The scattered NO($v = 0, J = 16.5$) was tagged via the R(16.5) transition to NO($v = 3, J = 17.5$) by the IR laser, which was then detected using the REMPI laser.

To selectively detect the NO($v = 0 - 0$) scattering channel, NO($v = 0, J = 16.5$) was tagged after scattering to NO($v = 3, J = 17.5$), see Figure 4.16 for a sketch of the tagging geometry. The REMPI laser was set to ionize the NO($v = 3, J = 17.5$) rotational state via the Q_{11}-branch. See Table 3.3 for the used transitions. All detectable molecules must have been excited during the interaction with the surface, because $J = 16.5$ is not populated in the incoming beam. A REMPI scan showing the populated rotational states in the incoming beam is shown in Figure 3.8.

Figure 4.17 shows time of flight data for the previously discussed $v = 3 - 3$ scattering (black) and the $v = 0 - 0$ scattering channel (green). During trapping desorption, the molecules equilibrate with the surface and leave with a thermal velocity. The thermal velocity is lower than that of the directly scattered molecules, which results in a slow tail (large time of flight) in the time of flight data. Comparing the 3–3 and 0–0 scattering channels, the tail is clearly visible for the latter and becomes more dominant for slower incidence energies. It also seems to decrease in intensity for higher surface temperatures, but the trapping desorption distributions will shift to faster energies with increasing surface temperature, causing this effect. For the slowest incidence energy of 0.11 eV, the rising edge of the signal shifts to longer times of flight, which can be interpreted as a decrease in the amount of directly scattered molecules.

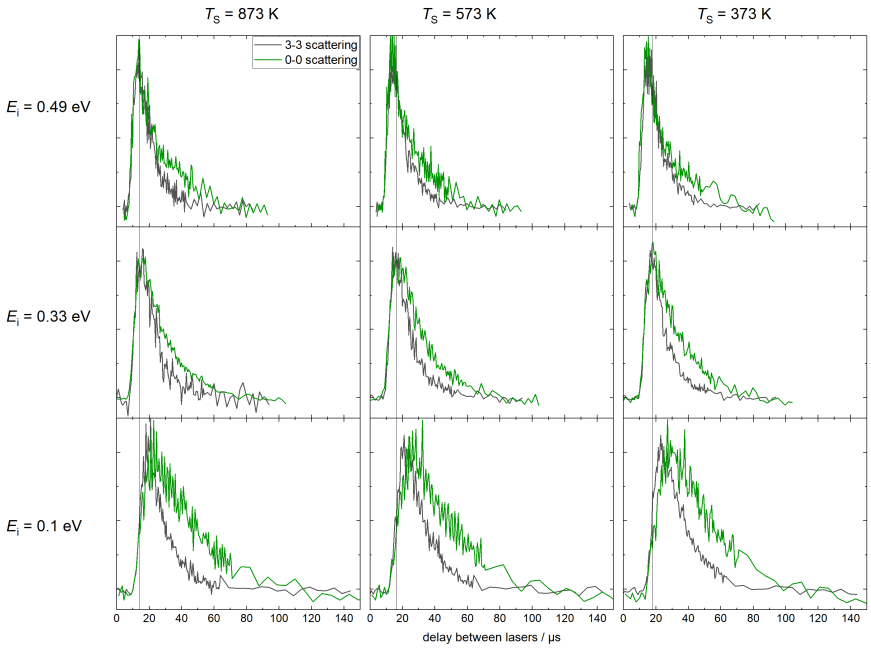

Figure 4.17: Normalized time of flight spectra for NO scattered from Gr/Pt. The black curve shows the 3-3 scattering channel discussed in the previous chapter, and the green curve the 0-0 scattering channel. For the latter, a tail at high time of flight is present that is typical for a trapping desorption scattering mechanism and is absent in the former. For an incidence energy of $E_i = 0.11$ eV, the rising edge shifts to later laser delays, which can be interpreted as the absence of the direct scattering component.

Modeling the data with detailed balance

To fit this combination of direct scattering and trapping desorption, the fitting function consists of two component: A thermal Maxwell-Boltzmann distribution fixed to the surface temperature that is weighted by detailed balance and the flowing 3D Maxwell-Boltzmann distribution used for fitting the direct scattering component. The resulting thermal component show a sub-thermal speed distribution, which means that the speed of the desorbing molecules is described by a Maxwell-Boltzmann distribution at temperature lower than the surface temperature in the experiment. Similar translational energy distributions were observed by Rettner and co-workers for Ar scattering from a hydrogen saturated W(100) surface,[67] hence a sticking function of the same form was used in the current analysis. The sticking function $S(E)$ describes the sticking probability as a function of incidence energy and is shown in Equation 4.3. According to detailed balance, if slow molecules have a higher sticking probability than fast molecules, the latter is also less likely to desorb from the surface, which is described by the sticking function.

$$S(E) = \frac{1}{1 + \exp(nE\cos(\theta) - A)} \tag{4.3}$$

Here n and A are fitting parameters, E is the energy and θ is the angle of incidence relative to the surface normal. Using this sticking function, Rettner *et al.* were able to properly fit their data.

The complete model used to fit the NO($v = 0 - 0$) scattering data is shown in Equation 4.4

$$S_{\text{direct}}(t) + S_{\text{trap}}(t) \cdot \text{MB}(T_S), \tag{4.4}$$

where $S(t)$ is the flowing 3D Maxwell-Boltzmann distribution (see Equation 3.8), $S_{\text{trap}}(t)$ is the sticking function tranformed into time-space and $\text{MB}(T_S)$ is a thermal Maxwell-Boltzmann distribution fixed at the surface temperature (Equation 4.5). The $\cos(\theta)$-term in the sticking function was neglected, because all experiments were carried out at close to normal incidence angle.

$$\text{MB}(T_S) = f_v(v) = A_{\text{MB}} \cdot 4\pi \cdot v^3 \left(\frac{m_{\text{NO}}}{2\pi \cdot k_B T_S} \right)^{\frac{3}{2}} \cdot \exp\left[-\frac{m_{\text{NO}} v^2}{2 k_B T_S} \right] l^{-1} \tag{4.5}$$

Due to the leading edge of the time of flight signal for the lowest incidence kinetic energy shifting to later times (see Figure 4.17 and text), it was assumed that more than 90% of all scattering for $E_i = 0.11$ eV is trapping-desorption and as such can be fitted only with $S_{\text{trap}} \cdot \text{MB}(T_S)$. The data was then fitted using the model shown in Equation 4.4, with the sticking function being fit globally, and the thermal component being fixed to a Maxwell-Boltzmann distribution at the surface temperature.

Translational inelasticity

The resulting fits and its components are shown in Figure 4.18 a in time-space and in Figure 4.18 b in energy space: the sticking function (green), the direct scattering component (blue, dashed), the trapping desorption component multiplied with the sticking function (red, dash-dotted) and the complete model (black, the sum of the latter two). For the slowest incidence energy, the data is only fitted with the thermal component, as no deconvolution of direct scattering and trapping desorption is possible due to overlapping signals. The resolution of the experiment is not good enough to distinguish between a possible directly scattered component and trapping desorption, because of the high translational energy loss during direct scattering. For both $E_i = 0.33$ eV and $E_i = 0.49$ eV, the model describes the data very well. A small dependence of the directly scattered component on the surface temperature is visible, as shown by the fitting parameters shown in

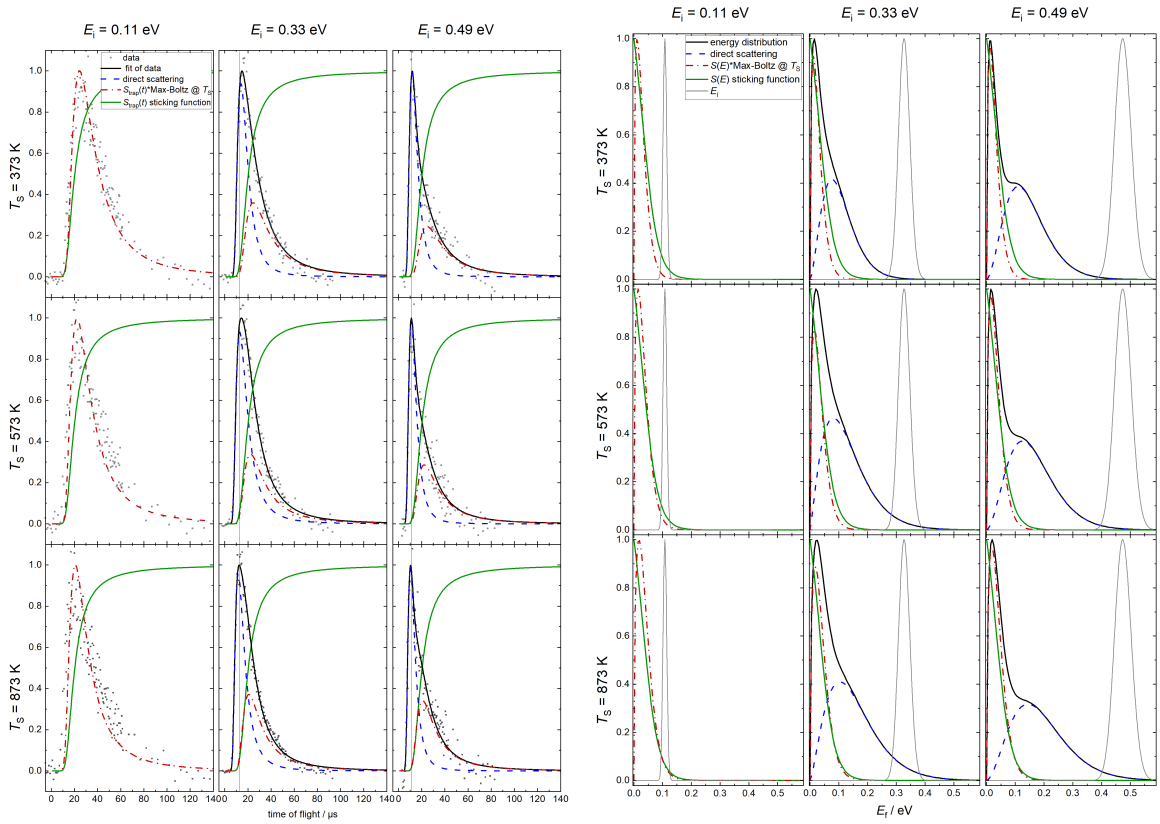

Figure 4.18: (a) Normalized data fitted with the model (black line) consisting of a direct scattering part (blue, dashed), a trapping desorption part that includes the sticking function (red, dash-dotted) as well as the sticking function (green). (b) The same fits transformed into energy space. The incident beam is shown in gray.

Table 4.2. For $E_i = 0.33$ eV, a small amount of molecules with a final translational energy larger than the incident one are observed.

The mean final translational energies of the direct scattering component are shown in Fig. 4.19 as green circles together with the corresponding values of the 3–3 scattering channel. Note that in this case all values are for $J = 16.5$. For both scattering channels, $\overline{E}_f$ shows the same small dependence on the surface temperature as well as a dependence on the incidence kinetic energy. The final translational energy is also very similar for both scattering channels. The small deviation in E_f is likely due to the mathematical model used in the analysis and not be discussed here, as they are close to the resolution of the experiment.

Table 4.2: Fitting parameters of the directly scattered component.

E_i/eV	T_S/K	v_0/ms^{-1}	α/ms^{-1}
0.49	373	640	409
	573	685	434
	873	723	475
0.33	373	494	374
	573	359	509
	873	494	510

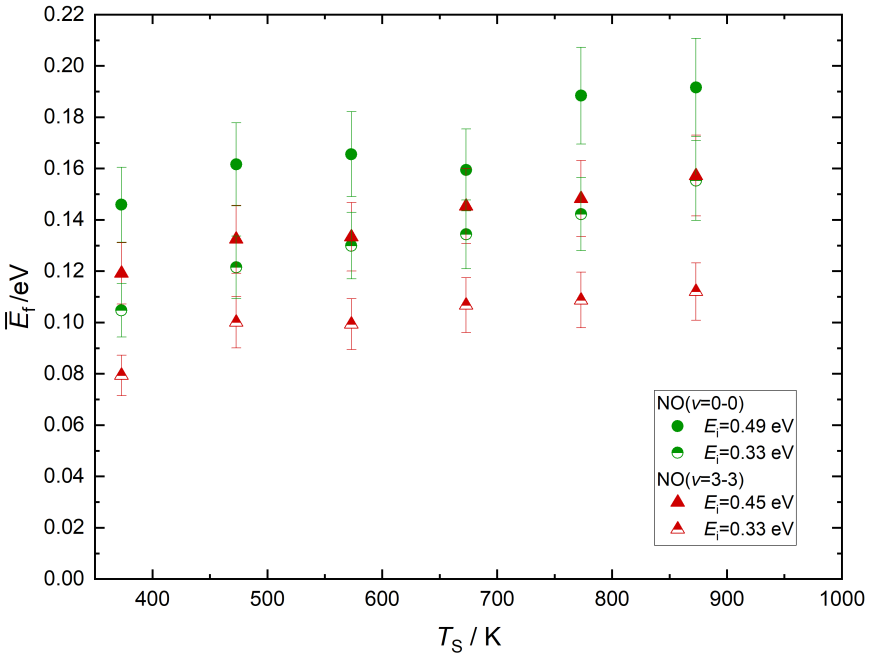

Figure 4.19: Mean final translational energies of the NO(v=0–0) (green circles) and NO(v=3–3) (red squares) scattering channels on Gr/Pt. All values for $J = 16.5$. For the 0-0 scattering channel, the mean velocities of the directly scattered component are shown. The energy loss is very similar for both vibrationally elastic scattering channels.

Sticking probability

Figure 4.20 shows the sticking functions used for the fitting. One sticking function was used per surface temperature and a surface temperature dependence of $S_{\mathrm{trap}}(E)$ is visible, although the effect is very small. The inset shows the half-value of the sticking function, which changes by about 0.015 eV over the range of 500 K. However, it should be noted that the trapping probability given by the sticking function disagrees with the experimentally observed one. For the lowest incidence kinetic energy of $E_{\mathrm{i}} = 0.11\,\mathrm{eV}$, an experimental trapping probability >90% was found, whereas the sticking function predicts 3%–11% trapping probability, increasing with increasing surface temperature. For higher incidence translational energies, these values are even lower, to the point, where no sticking should be observed. A precurser-mediated trapping mechanism could explain this discrepancy. Under these conditions, a direct comparison with detailed balance would not be valid anymore, because detailed balance assumes a direct equilibrium between two states without any intermediates.

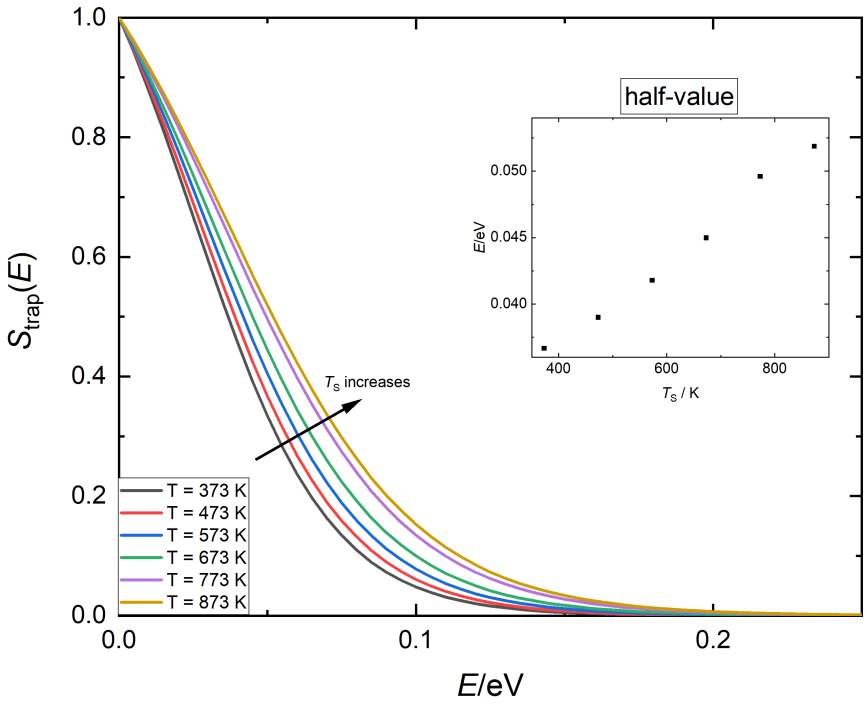

Figure 4.20: Sticking function $S(E)$ for different surface temperatures. The inset shows the values of $S(E) = 0.5$ as a function of the surface temperature.

Branching ratio

A branching ratio between the directly scattered and the trapped molecules can be extracted from the fits by integrating each component separately. This value is then divided by the integral of the whole model to get the fraction of directly scattered molecules shown in Figure 4.21. Over the investigated temperature range, more molecules are scattered directly and the branching ratio remains constant within the uncertainty of the experiment.

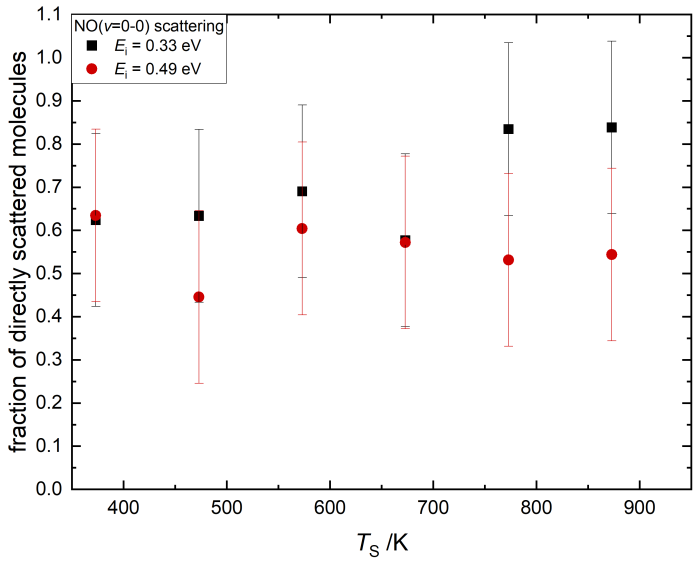

Figure 4.21: Branching ratio between direct scattering and trapping desorption for two incidence kinetic energies as a function of the surface temperature. The fraction of directly scattered molecules remains constant within the uncertainty of the experiment over the whole temperature range.

Summary

For vibrationally elastic scattering of NO in its vibrational ground state, a combination of direct scattering and trapping desorption has been observed. The trapping component had to be weighted by detailed balance, which resulted in sub-thermal speed distributions of the desorbing nitric oxide, because the sticking probability decreases with increasing incidence kinetic energy. On graphite, no sticking was observed in the investigated temperature range, an observation that is in agreement with the findings of Frenkel *et al.*, who found no signs of trapping for $T_S > 300$ K.[40] Similar results were reported by Segner *et al.* for NO scattering from graphitized Pt(111).[39]. It is important to point out, that Segner and co-workers investigated NO scattering from "graphitized platinum", which is not the

same as the high quality graphene used in this work. Segner and co-workers found "a graphite overlayer as characterized by the well-known ring-like LEED pattern".[39] They did not show a LEED pattern, but since they dosed the platinum with a high dose of ethylene at 1000 K, a LEED pattern similar to that of HOPG is expected. This ring-like pattern is caused by multiple graphene domains of different orientation with respect to the substrate, whereas the LEED pattern of a high quality graphene surface shows distinct spots.[54] See Figure 4.22 for a comparison of LEED images of Gr/Pt(111) and HOPG.

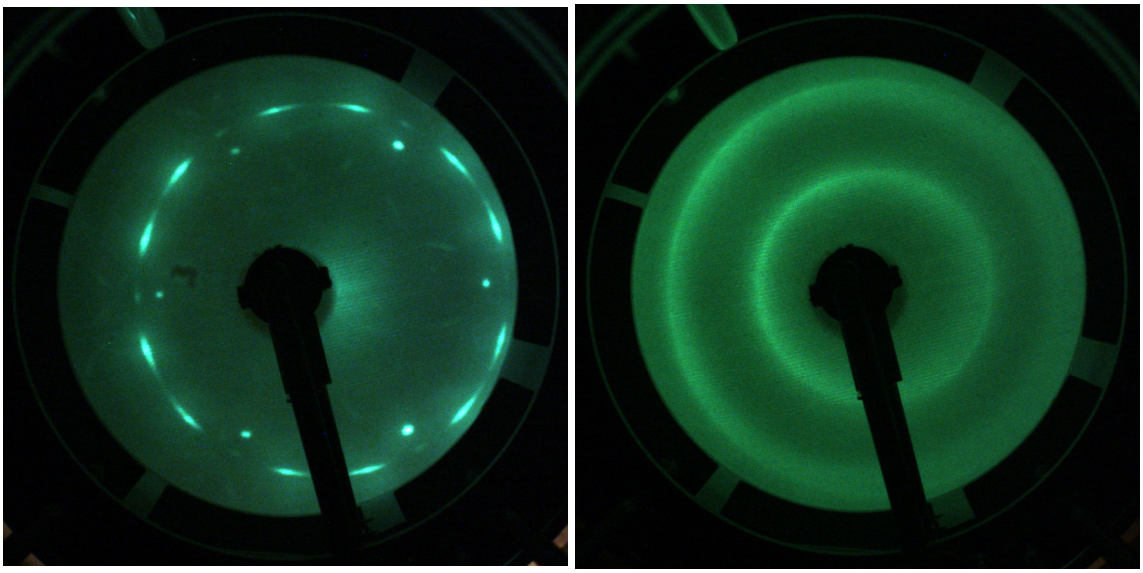

(a) (b)

Figure 4.22: (a) LEED image of graphene on Pt(111). Measured at 83 eV electron energy, 39 µA emission and 2.45 µA beam current at 650 ms exposure time. The LEED pattern is off-center, because the surface was tilted slightly. (b) LEED pattern of HOPG. Measured at 185 eV electron energy, 41 µA emission and 2.31 µA beam current at 162 ms exposure time.

4.3 Discussion

On one hand, the scattering dynamics of NO from epitaxial graphene on platinum and graphite are very different. On Gr/Pt, trapping desorption is observed, that leads to vibrational excitation of the trapped molecules. On graphite, no trapping is observed and the translational energy loss is smaller than on graphene. On the other hand, the T–R-coupling is surprisingly similar for both surfaces. Neither of the latter two can be used to explain the large difference in stickyness.

The high amount of translational energy lost of NO scattered from graphene has also been observed by Greenwood *et al.*[17], who investigated NO($v = 0 - 0$) scattering on

Gr/Au and found a similar energy loss of up to 80% both in experiment and molecular dynamics simulations. They also found NO gaining translational energy for low incidence translational energies in the simulations[104] and assigned the increased "softness" of the graphene to the large interlayer distance of 3.4 Å between the Au substrate and the graphene.[17] This interlayer distance is very similar to the 3.31 Å in Gr/Pt[37] and the 3.34 Å in graphite[53], which makes the interlayer distance an unlikely reason for the observed effects. Another possible explanation for the large translational energy loss is the coupling to phonons, which has been observed to be very efficient for N_2 scattering from HOPG.[41,42], even though they observed a smaller energy loss between 10-30%. If the translation-phonon coupling is efficient, not only can this explain the translational inelasticity, but also make the transfer of thermal energy from the surface to the NO molecules possible, increasing the final translational energy to values above the incidence velocity. As this effect is most prominent at the lowest kinetic energy, it could be caused by interactions of the NO with the out-of-plane optical (ZO) and acoustical (ZA) phonons of graphene.[52,105] See Figure 4.23 for a phonon spectrum of graphene, and Figure 2.4 b for a comparison of the phonon dispersion of graphene and graphite. Although the same authors reported that the phonon dispersion of Gr/Pt and graphite are very similar, one important difference is the lifted degeneracy of the ZO and ZA modes at the $\overline{\text{K}}$-point, which could change the way the NO interacts with both surfaces.[52]

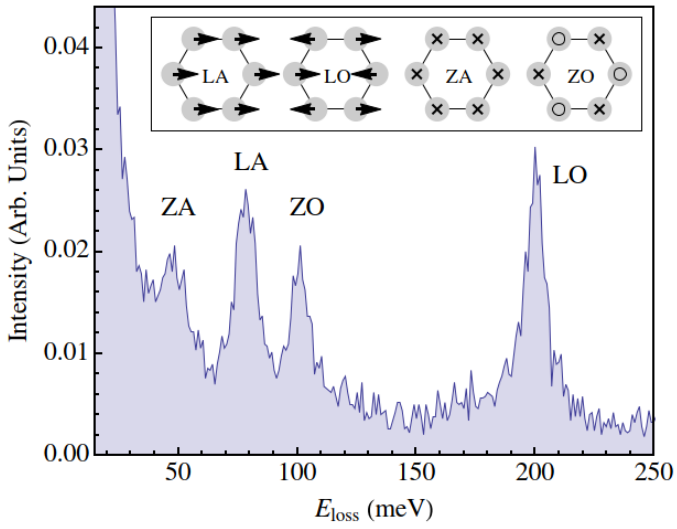

Figure 4.23: Phonon spectrum of Gr/Pt(111) measured by HREELS. Data shown in for a scattering angle of $\theta_s = 48°$. The inset shows the displacement of the observed phonons. Crosses indicate movement into the plane, and circles movement out of it. Reprinted with permission from Reference [106]. Copyright (2015) by the American Physical Society.

Interaction of the vibrational motion of trapped NO with the phonons of graphene

could also be an explanation for observed vibrational excitation on graphene. The energy required for the excitation of one vibrational quantum in NO is 0.233 eV, which is close to the energy of the phonons. The out-of-plane phonon modes have energies of 0.01 eV (ZA) and 0.1 eV (ZO), and the two in-plane phonon modes of 0.2 eV (longitudinal (LO) and transverse (TO) optical phonons).[52] Theory for NO adsorbed on freestanding graphene found NO to be an electron donor, increasing the N=O-bond length of the adsorbed NO compared to gas-phase NO,[43,45,46] in turn reducing the frequency and thus the energy of the vibration. Moreover, Politano *et al.* observed electron-phonon-coupling (EPC) for the ZO and LO modes in graphene on platinum, which can influence many physical properties of the graphene. For the ZO mode, these have been speculated to cause a spontaneous buckling of the graphene lattice.[106] This buckling could be similar to the defomation of graphene that happens during the transient bond formation with the H-atoms and possibly enhance the sticking probability.

Regarding the trapping of NO, a comparison of possible bound states and their adsorption energies on graphene and graphite does not provide further clarity. The experimental binding energy for NO on graphite is 0.124 eV[107], and calculated binding energies for NO on freestanding graphene vary between −0.029 eV to − 2.4 eV[43–47], with most calculations finding $E_{\mathrm{ads}} < 0.3$ eV. All calculations only found physisorbed NO, but since NO is a radical, transient bond formation might play an important role, similar to the findings of Jiang *et al.*[34] They found that transient bond formation during the scattering causes a large translational energy loss for H-atoms scattered from Gr/Pt(111). More recent calculations looking for the adsorption of NO on Gr/Pt also only found a physisorbed state with a binding energy of $E_{\mathrm{ads}} = -0.322$ eV. However, in these calculations, the graphene–platinum distance is increased to 3.42 Å,[108] but no chemisorbed or bound state was found. The binding geometry is shown in Figure 4.24. Moreover, it should be noted that the trapping probability seems to depend on the vibrational state of the NO molecule. The NO($v = 1$) time of flight data were described well by a thermal speed distribution, while the thermal component of the scattered NO($v = 0$) had to be weighted by detailed balance.

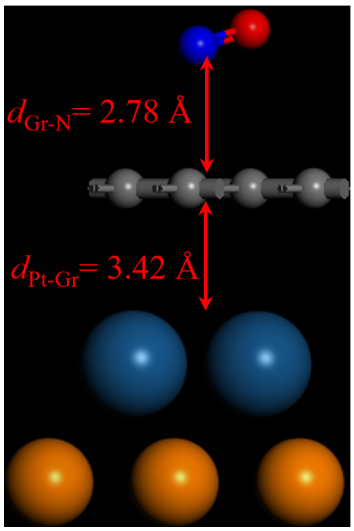

Figure 4.24: Calculated physisorption geometry of NO on Gr/Pt.[108]. The N-atom is shown in blue, and the O-atom in red.

5 Conclusion

Vibrational excitation during the collision of gas molecules with metal surfaces has been observed for different systems. For NH_3 scattered from Au(111), an adiabatic transfer of kinetic energy to vibrational motion was observed.[27] The vibrational excitation of NO on Ag(111) on the other hand is the result of a non-adiabatic mechanism that involves an interaction of thermal electron hole pairs in the surface with the molecule.[28] Molecule-surface scattering at insulator surfaces has shown a purely adiabatic behavior, as would be expected, because no electronic states are available.[29] Semiconductors are in between metals and insulators in regards to their electronic structure. Graphene is an especially interesting semiconductor because of its special zero-bandgap electronic structure, which lead to the following question: Does the interaction of molecules with graphene show signs of non-adiabatic behavior?

Moreover, Greenwood and Köhler recently studied vibrationally elastic scattering of NO($v = 0$) from Gr/Au.[17] In their experiments, the NO loses up to 80% of its kinetic energy to the surface, but no signs of a trapping-desorption scattering mechanism were found. These findings agree with experiments on NO scattering from graphite and graphitized platinum.[39,40] However, preliminary experiments conducted in our group on NO scattering from Gr/Pt(111) showed clear signs of trapping desorption, which lead to the next questions: Does nitric oxide trap on epitaxial graphene on Pt(111)? Is the sticking a direct result of the large kinetic energy loss during the scattering process, and is this energy loss different on graphite?

To investigate these questions, a molecular beam surface scattering study has been carried out, in which NO molecules in a defined quantum state were scattered from Gr/Pt(111) and HOPG at different surface temperatures. Thermal vibrational excitation of NO($v = 0$) to NO($v = 1$) has been observed during the collision with Gr/Pt as the result of a trapping desorption scattering mechanism in the range from 373 K to 873 K. Trapping desorption scattering as a mechanism is further supported by broad angular distributions, as well as a rotational and kinetic energy distribution of the scattered molecules that agrees with the thermally expected distributions for each surface temperature. No signs of a non-adiabatic

interaction were found. On the contrary, no vibrational excitation of NO was observed during the collision with HOPG. The observed scattered NO($v = 1$) is a results of vibrationally elastic scattering of the thermal population of NO($v = 1$) in the incoming beam. The rotational distribution and vibrational population of NO($v = 1$) were independent of the surface temperature and the angular distributions were narrow, which indicates a direct scattering mechanism. This direct scattering mechanism is in agreement with the results of Frenkel *et al.* and Segner *et al.* that were mentioned earlier.[39,40]

Vibrationally elastic scattering of NO($v = 3, J = 0.5$) allowed for a background free investigation of the translational inelasticity of NO scattering from graphene and graphite. For both surfaces, state to state time of flight experiments revealed a pure direct scattering mechanism with very efficient transfer of kinetic energy to the surface. As a result, the NO molecules lose up to 66% of their kinetic energy on HOPG, and up to 80% on Gr/Pt, which agrees with the results of Greenwood and Köhler.[17] The final translational energy of NO scattered from graphene shows a stronger dependence on the surface temperature than that of NO scattered from graphite. Moreover, at the slowest kinetic energy of $E_i = 0.11$ eV, a fraction of the NO molecules are accelerated by the graphene surface, resulting in molecules that have a final translational energy larger than the incidence one. Analysis of the translation–rotation coupling revealed strong interactions with the phonons for both surfaces.

Additionally, vibrationally elastic scattering of NO($v = 0$) was studied to gain further insight into the trapping of NO on graphene. The time of flight data were fitted by a combination of direct scattering and trapping desorption weighted by detailed balance. The directly scattered component showed a similarly large energy loss as the vibrationally elastically scattered NO($v = 3$), although with a small deviation. This deviation is most likely a result of the mathematical model used to describe the data. A noticeable difference is that the incidence kinetic energy seems to affect the sticking probability in the vibrationally elastic scattering of NO($v = 0$), but does not have any influence on the sticking probability of NO($v = 1$). It should also be noted that it is not clear, if detailed balance can be used to properly describe the current system, because the sticking probability given by the sticking function disagrees with the observations from the experiment. A precursor-mediated adsorption mechanism would explain this difference, as detailed balance would not be applicable anymore.

As a conclusion, the experimental results presented in this thesis show a difference between the surface scattering dynamics of Gr/Pt and HOPG. While only direct scattering is observed on HOPG, epitaxial graphene on Pt(111) shows clear evidence of direct scatter-

ing and trapping desorption. The increased stickyness of graphene compared to graphite cannot be explained by a significantly higher translational energy loss at either surface, because this transfer is only 1.2-times more efficient on graphene. However, interactions with the phonons of the surface could play an important role, as the out-of-plane phonons are energetically favorable at 0.1 eV (ZO) and 0.01 eV (ZA). Even though they are similar for graphite and graphene near the Γ-point, their degeneracy is lifted for the latter.[52] Moreover, electron-phonon coupling has been observed for the ZO phonon of graphene, which is not present in graphite.[106] The interlayer distance in graphene and graphite is also too similar at 3.31 Å[37] and 3.34 Å,[53] respectively, to cause a significant softening of the graphene surface.

Overall, further theoretical calculations are needed to fully understand the processes involved in the scattering of NO from graphene on platinum. The experimental results provided by this work can be used as a reference for theory.

As for further experimental work, the observed degradation of graphene in the presence of NO/H_2 (or other oxidizing gases in that matter) are an interesting area of research, especially when looking at the possible applications of graphene, either in catalysis, electronics or gas sensing.[6,11,12] Understanding the adsorption mechanism and reactivity of gas molecules on graphene could make it an interesting substrate for catalytically active nanoparticles. The graphene would act as a ”net”, that catches all the molecules, which can then reach the active sites via diffusion. The high translational energies achievable in the molecular beam experiments under ultra-high vacuum conditions might not be important for these catalytic devices, but as graphene is a possible material for heat shields in air- and space craft,[9–11] impacts of oxidizing molecules with high translational energy are another important area of research. Graphene based electronics might be of use in satellites due to the possibility of producing very thin, light, flexible and efficient devices.[9]

Bibliography

[1] K. S. Novoselov, V. I. Fal'ko, L. Colombo, P. R. Gellert, M. G. Schwab, K. Kim, A roadmap for graphene, *Nature* **490** (2012) 192–200. doi:10.1038/nature11458.

[2] A. C. Ferrari, F. Bonaccorso, V. Fal'ko, K. S. Novoselov, S. Roche, P. Bøggild, S. Borini, F. H. L. Koppens, V. Palermo, N. Pugno, J. A. Garrido, R. Sordan, A. Bianco, L. Ballerini, M. Prato, E. Lidorikis, J. Kivioja, C. Marinelli, T. Ryhänen, A. Morpurgo, J. N. Coleman, V. Nicolosi, L. Colombo, A. Fert, M. Garcia-Hernandez, A. Bachtold, G. F. Schneider, F. Guinea, C. Dekker, M. Barbone, Z. Sun, C. Galiotis, A. N. Grigorenko, G. Konstantatos, A. Kis, M. Katsnelson, L. Vandersypen, A. Loiseau, V. Morandi, D. Neumaier, E. Treossi, V. Pellegrini, M. Polini, A. Tredicucci, G. M. Williams, B. Hee Hong, J.-H. Ahn, J. Min Kim, H. Zirath, B. J. van Wees, H. van der Zant, L. Occhipinti, A. Di Matteo, I. A. Kinloch, T. Seyller, E. Quesnel, X. Feng, K. Teo, N. Rupesinghe, P. Hakonen, S. R. T. Neil, Q. Tannock, T. Löfwander, J. Kinaret, Science and technology roadmap for graphene, related two-dimensional crystals, and hybrid systems, *Nanoscale* **7** (2015) 4598–4810. doi:10.1039/C4NR01600A.

[3] A. K. Geim, Graphene: Status and prospects, *Science* **324** (2009) 1530–1534. doi:10.1126/science.1158877.

[4] S. Kang, D. Lee, J. Kim, A. Capasso, H. S. Kang, J.-W. Park, C.-H. Lee, G.-H. Lee, 2D semiconducting materials for electronic and optoelectronic applications: potential and challenge, *2D Materials* **7** (2020) 022003. doi:10.1088/2053-1583/ab6267.

[5] W. Liu, M. Liu, X. Liu, X. Wang, H.-X. Deng, M. Lei, Z. Wei, Z. Wei, Recent advances of 2D materials in nonlinear photonics and fiber lasers, *Advanced Optical Materials* **8** (2020) 1901631. doi:https://doi.org/10.1002/adom.201901631.

[6] M. Nomani, R. Shishir, M. Qazi, D. Diwan, V. Shields, M. Spencer, G. S. Tompa, N. M. Sbrockey, G. Koley, Highly sensitive and selective detection of NO_2 using epitaxial graphene on 6H-SiC, *Sensors and Actuators B: Chemical* **150** (2010) 301–307. doi:https://doi.org/10.1016/j.snb.2010.06.069.

[7] F. Schedin, A. K. Geim, S. V. Morozov, E. W. Hill, P. Blake, M. I. Katsnelson, K. S. Novoselov, Detection of individual gas molecules adsorbed on graphene, *Nature Materials* **6** (2007) 652–655. doi:10.1038/nmat1967.

[8] H. Huang, H. Shi, P. Das, J. Qin, Y. Li, X. Wang, F. Su, P. Wen, S. Li, P. Lu, F. Liu, Y. Li, Y. Zhang, Y. Wang, Z.-S. Wu, H.-M. Cheng, The chemistry and promising applications of graphene and porous graphene materials, *Advanced Functional Materials* **30** (2020) 1909035. doi:https://doi.org/10.1002/adfm.201909035.

[9] E. J. Siochi, Graphene in the sky and beyond., *Nature Nanotech* **9** (2014) 745–747. doi:10.1038/nnano.2014.231.

[10] Joshuamukesh, V. Kumar, Mathankumar, M. Ferozudeen, Thermal analysis of reentry capsule over the heat shield, *International Journal of Progressive Research in Science and Engineering* **1** (2020) 121–124.

[11] C. Luo, T. Jiao, J. Gu, Y. Tang, J. Kong, Graphene shield by SiBCN ceramic: A promising high-temperature electromagnetic wave-absorbing material with oxidation resistance, *ACS Applied Materials & Interfaces* **10** (2018) 39307–39318, pMID: 30351896. doi:10.1021/acsami.8b15365.

[12] R. R. Mohan, S. J. Varma, M. Faisal, J. S, Polyaniline/graphene hybrid film as an effective broadband electromagnetic shield, *RSC Adv.* **5** (2015) 5917–5923. doi:10.1039/C4RA13704C.

[13] C. Herbig, T. Michely, Graphene: the ultimately thin sputtering shield, *2D Materials* **3** (2016) 025032. doi:10.1088/2053-1583/3/2/025032.

[14] Y. Fu, J. Hansson, Y. Liu, S. Chen, A. Zehri, M. K. Samani, N. Wang, Y. Ni, Y. Zhang, Z.-B. Zhang, Q. Wang, M. Li, H. Lu, M. Sledzinska, C. M. S. Torres, S. Volz, A. A. Balandin, X. Xu, J. Liu, Graphene related materials for thermal management, *2D Materials* **7** (2019) 012001. doi:10.1088/2053-1583/ab48d9.

[15] D. G. Papageorgiou, I. A. Kinloch, R. J. Young, Mechanical properties of graphene and graphene-based nanocomposites, *Progress in Materials Science* **90** (2017) 75–127. doi:10.1016/j.pmatsci.2017.07.004.

[16] A. K. Geim, K. S. Novoselov, The rise of graphene, *Nature Materials* **6** (2007) 183–191. doi:10.1038/nmat1849.

[17] T. Greenwood, S. P. K. Köhler, Nitric oxide scattering off graphene using surface-velocity map imaging, *The Journal of Physical Chemistry C* **125** (2021) 17853–17860. doi:10.1021/acs.jpcc.1c05014.

[18] J. C. Tully, Perspective on "Zur Quantentheorie der Molekeln", *Theoretical Chemistry Accounts* **103** (2000) 173–176. doi:10.1007/s002149900049.

[19] I. Rahinov, R. Cooper, D. Matsiev, C. Bartels, D. J. Auerbach, A. M. Wodtke, Quantifying the breakdown of the born–oppenheimer approximation in surface chemistry, *Physical Chemistry Chemical Physics* **13** (2011) 12680–12692. doi:10.1039/C1CP20356H.

[20] C. T. Rettner, D. J. Auerbach, J. C. Tully, A. W. Kleyn, Chemical dynamics at the gas–surface interface, *The Journal of Physical Chemistry* **100** (1996) 13021–13033. doi:10.1021/jp9536007.

[21] A. M. Wodtke, J. C. Tully, D. J. Auerbach, Electronically non-adiabatic interactions of molecules at metal surfaces: Can we trust the Born-Oppenheimer approximation for surface chemistry?, *International Reviews in Physical Chemistry* **23** (2004) 513–539. doi:10.1080/01442350500037521.

[22] B. C. Krüger, N. Bartels, C. Bartels, A. Kandratsenka, J. C. Tully, A. M. Wodtke, T. Schäfer, NO vibrational energy transfer on a metal surface: Still a challenge to first-principles theory, *The Journal of Physical Chemistry C* **119** (2015) 3268–3272. doi:10.1021/acs.jpcc.5b00388.

[23] C. T. Rettner, H. A. Michelsen, D. J. Auerbach, Quantum-state-specific dynamics of the dissociative adsorption and associative desorption of H_2 at a Cu(111) surface, *The Journal of Chemical Physics* **102** (1995) 4625–4641. doi:10.1063/1.469511.

[24] A. M. Wodtke, H. Yuhui, D. J. Auerbach, Insensitivity of trapping at surfaces to molecular vibration, *Chemical Physics Letters* **413** (2005) 326 – 330. doi:10.1016/j.cplett.2005.06.031.

[25] J. Neugebohren, D. Borodin, H. W. Hahn, J. Altschäffel, A. Kandratsenka, D. J. Auerbach, C. T. Campbell, D. Schwarzer, D. J. Harding, A. M. Wodtke, T. N. Kitsopoulos, Velocity-resolved kinetics of site-specific carbon monoxide oxidation on platinum surfaces, *Nature* **558** (2018) 280–283. doi:10.1038/s41586-018-0188-x.

[26] G. Park, T. N. Kitsopoulos, D. Borodin, K. Golibrzuch, J. Neugebohren, D. J. Auerbach, C. T. Campbell, A. M. Wodtke, The kinetics of elementary thermal reactions in heterogeneous catalysis, *Nature Reviews Chemisty* **3** (2019) 723–732. doi:10.1038/s41570-019-0138-7.

[27] B. D. Kay, T. D. Raymond, M. E. Coltrin, Observation of direct multiquantum vibrational excitation in gas-surface scattering: NH_3 on Au(111), *Physical Review Letters* **59** (1987) 2792–2794. doi:10.1103/PhysRevLett.59.2792.

[28] C. T. Rettner, F. Fabre, J. Kimman, D. J. Auerbach, Observation of direct vibrational excitation in gas-surface collisions: NO on Ag(111), *Phys. Rev. Lett.* **55** (1985) 1904–1907. doi:10.1103/PhysRevLett.55.1904.

[29] Y. Huang, C. T. Rettner, D. J. Auerbach, A. M. Wodtke, Vibrational promotion of electron transfer, *Science* **290** (2000) 111–114. doi:10.1126/science.290.5489.111.

[30] P. R. Shirhatti, J. Werdecker, K. Golibrzuch, A. M. Wodtke, C. Bartels, Electron hole pair mediated vibrational excitation in CO scattering from Au(111): Incidence energy and surface temperature dependence, *The Journal of Chemical Physics* **141** (2014) 124704. doi:10.1063/1.4894814.

[31] J. D. White, J. Chen, D. Matsiev, D. J. Auerbach, A. M. Wodtke, Vibrationally promoted electron emission from low work-function metal surfaces, *The Journal of Chemical Physics* **124** (2006) 064702. doi:10.1063/1.2166360.

[32] B. C. Krüger, *From diatomic to polyatomic quantum-state-resolved molecule-surface scattering*, Dissertation, Georg-August-Universität Göttingen, Göttingen **(2017)**.

[33] A. H. Castro Neto, F. Guinea, N. M. R. Peres, K. S. Novoselov, A. K. Geim, The electronic properties of graphene, *Rev. Mod. Phys.* **81** (2009) 109–162. doi:10.1103/RevModPhys.81.109.

[34] H. Jiang, M. Kammler, F. Ding, Y. Dorenkamp, F. R. Manby, A. M. Wodtke, T. F. Miller, A. Kandratsenka, O. Bünermann, Imaging covalent bond formation by H atom scattering from graphene, *Science* **364** (2019) 379–382. doi:10.1126/science.aaw6378.

[35] H. Jiang, *Dynamics of Hydrogen Atoms Scattering from Surfaces*, Ph.D. thesis, Georg-August-Universität Göttingen **(2016)**.

[36] G. W. Cushing, V. Johánek, J. K. Navin, I. Harrison, Graphene growth on Pt(111) by ethylene chemical vapor deposition at surface temperatures near 1000 K, *The Journal of Physical Chemistry C* **119** (2015) 4759–4768. doi:10.1021/jp508177k.

[37] M. Gao, Y. Pan, C. Zhang, H. Hu, R. Yang, H. Lu, J. Cai, S. Du, F. Liu, H.-J. Gao, Tunable interfacial properties of epitaxial graphene on metal substrates, *Applied Physics Letters* **96** (2010) 053109. doi:10.1063/1.3309671.

[38] P. Sutter, J. T. Sadowski, E. Sutter, Graphene on Pt(111): Growth and substrate interaction, *Physical Review B* **80** (2009) 245411. doi:10.1103/physrevb.80.245411.

[39] J. Segner, H. Robota, W. Vielhaber, G. Ertl, F. Frenkel, J. Häger, W. Krieger, H. Walther, Rotational state populations of no molecules scattered from clean and adsorbate-covered pt(111) surfaces, *Surface Science* **131** (1983) 273–289. doi:https://doi.org/10.1016/0039-6028(83)90277-7.

[40] F. Frenkel, J. Häger, W. Krieger, H. Walther, G. Ertl, J. Segner, W. Vielhaber, Rotational state populations and angular distributions on surface scattered molecules: NO on graphite, *Chemical Physics Letters* **90** (1982) 225–229. doi:10.1016/0009-2614(82)80031-6.

[41] M. Majumder, H. N. Bhandari, S. Pratihar, W. L. Hase, Chemical dynamics simulation of low energy N_2 collisions with graphite, *The Journal of Physical Chemistry C* **122** (2018) 612–623. doi:10.1021/acs.jpcc.7b10338.

[42] N. A. Mehta, V. J. Murray, C. Xu, D. A. Levin, T. K. Minton, Nonreactive scattering of n2 from layered graphene using molecular beam experiments and molecular dynamics, *The Journal of Physical Chemistry C* **122** (2018) 9859–9874. doi:10.1021/acs.jpcc.7b11721.

[43] Q. Zhou, Y. Yong, X. Su, W. Ju, Z. Fu, C. Wang, X. Li, Adsorption sensitivity of defected graphene towards NO molecule: a DFT study, *Journal of the Iranian Chemical Society* **15** (2018) 1755–1763. doi:10.1007/s13738-018-1373-4.

[44] X. Zhao, K. Li, P. Ning, C. Wang, X. Sun, Y. Ma, X. Song, L. Jia, X. Hao, Theoretical study on simultaneous removal of SO2, NO, and Hg^0 over graphene: competitive adsorption and adsorption type change, *Journal of Molecular Modeling* **25** (2019) 364. doi:10.1007/s00894-019-4254-6.

[45] H. Gao, Z. Liu, DFT study of NO adsorption on pristine graphene, *RSC Adv.* **7** (2017) 13082–13091. doi:10.1039/C6RA27137E.

[46] O. Leenaerts, B. Partoens, F. M. Peeters, Adsorption of h_2O, Nh_3, CO, No_2, and no on graphene: A first-principles study, *Phys. Rev. B* **77** (2008) 125416. doi:10.1103/PhysRevB.77.125416.

[47] S. Tang, Z. Cao, Adsorption of nitrogen oxides on graphene and graphene oxides: Insights from density functional calculations, *The Journal of Chemical Physics* **134** (2011) 044710. doi:10.1063/1.3541249.

[48] P. R. Wallace, The band theory of graphite, *Physical Review* **71** (1947) 622–634. doi:10.1103/PhysRev.71.622.

[49] K. S. Novoselov, A. K. Geim, S. V. Morozov, D. Jiang, Y. Zhang, S. V. Dubonos, I. V. Grigorieva, A. A. Firsov, Electric field effect in atomically thin carbon films, *Science* **306** (2004) 666–669. doi:10.1126/science.1102896.

[50] The nobel prize in physics 2010 (retrieved 18.01.2022).

[51] K. S. Novoselov, A. K. Geim, S. V. Morozov, D. Jiang, M. I. Katsnelson, I. V. Grigorieva, S. V. Dubonos, A. A. Firsov, Two-dimensional gas of massless dirac fermions in graphene, *Nature* **438** (2005) 197–200. doi:10.1038/nature04233.

[52] A. Politano, A. R. Marino, G. Chiarello, Phonon dispersion of quasi-freestanding graphene on Pt(111), *Journal of Physics: Condensed Matter* **24** (2012) 104025. doi:10.1088/0953-8984/24/10/104025.

[53] L. Spanu, S. Sorella, G. Galli, Nature and strength of interlayer binding in graphite, *Phys. Rev. Lett.* **103** (2009) 196401. doi:10.1103/PhysRevLett.103.196401.

[54] M. Gao, Y. Pan, L. Huang, H. Hu, L. Z. Zhang, H. M. Guo, S. X. Du, H.-J. Gao, Epitaxial growth and structural property of graphene on Pt(111), *Applied Physics Letters* **98** (2011) 033101. doi:10.1063/1.3543624.

[55] C. R. Arumainayagam, R. J. Madix, Molecular beam studies of gas-surface collision dynamics, *Progress in Surface Science* **38** (1991) 1 – 102. doi:10.1016/0079-6816(91)90006-P.

[56] K. Golibrzuch, *Quantum-state specific scattering of molecules from surfaces*, Ph.D. thesis, Georg-August Universität Göttingen **(2014)**.

[57] C. T. Rettner, The search for direct vibrational excitation in gas–surface collisions of CO with Au(111), *The Journal of Chemical Physics* **99** (1993) 5481–5489. doi:10.1063/1.465965.

[58] B. Baule, Theoretische Behandlung der Erscheinungen in verdünnten Gasen, *Annalen der Physik* **349** (1914) 145–176. doi:10.1002/andp.19143490908.

[59] K. Golibrzuch, P. R. Shirhatti, I. Rahinov, D. J. Auerbach, A. M. Wodtke, C. Bartels, Incidence energy dependent state-to-state time-of-flight measurements of NO(v = 3) collisions with Au(111): the fate of incidence vibrational and translational energy, *Physical Chemistry Chemical Physics* **16** (2014) 7602–7610. doi:10.1039/C3CP55224A.

[60] J. C. Tully, Dynamics of gas-surface interactions: Thermal desorption of Ar and Xe from platinum, *Surface Science* **111** (1981) 461 – 478. doi:10.1016/0039-6028(81)90402-7.

[61] R. C. Tolman, Duration of molecules in upper quantum states, *Phys. Rev.* **23** (1924) 693–709. doi:10.1103/PhysRev.23.693.

[62] R. C. Tolman, The principle of microscopic reversibility, *Proceedings of the National Academy of Sciences of the United States of America* **11** (1925) 436–439. doi:10.1073/pnas.11.7.436.

[63] R. C. Tolman, *The principles of statistical mechanics*, Oxford University Press, London, **1938**.

[64] R. H. Fowler, *Statistical Mechanics*, Cambridge University Press, **1929**.

[65] J. C. Batty, R. E. Stickney, Thermodynamics and kinetics of heterogeneous reactions., Tech. rep., Massachusetts Institute of Technology (1969).

[66] U. Leuthäusser, Kinetic theory of desorption: Energy and angular distributions, *Zeitschrift für Physik* **50** (1983) 65–69.

[67] C. T. Rettner, E. K. Schweizer, C. B. Mullins, Desorption and trapping of argon at a 2H–W(100) surface and a test of the applicability of detailed balance to a nonequilibrium system, *The Journal of Chemical Physics* **90** (1989) 3800–3813. doi:10.1063/1.455838.

[68] M. Cardillo, M. Balooch, R. Stickney, Detailed balancing and quasi-equilibrium in the adsorption of hydrogen on copper, *Surface Science* **50** (1975) 263–278. doi:https://doi.org/10.1016/0039-6028(75)90024-2.

[69] H. A. Michelsen, C. T. Rettner, D. J. Auerbach, R. N. Zare, Effect of rotation on the translational and vibrational energy dependence of the dissociative adsorption of D_2 on Cu(111), *The Journal of Chemical Physics* **98** (1993) 8294–8307. doi:10.1063/1.464535.

[70] S. Kaufmann, Q. Shuai, D. J. Auerbach, D. Schwarzer, A. M. Wodtke, Associative desorption of hydrogen isotopologues from copper surfaces: Characterization of two reaction mechanisms, *The Journal of Chemical Physics* **148** (2018) 194703. doi:10.1063/1.5025666.

[71] Q. Shuai, S. Kaufmann, D. J. Auerbach, D. Schwarzer, A. M. Wodtke, Evidence for electron–hole pair excitation in the associative desorption of H_2 and D_2 from Au(111), *The Journal of Physical Chemistry Letters* **8** (2017) 1657–1663, pMID: 28338329. doi:10.1021/acs.jpclett.7b00265.

[72] F. R. Gilmore, Potential energy curves for N_2, NO, O_2 and corresponding ions, *Journal of Quantitative Spectroscopy and Radiative Transfer* **5** (1965) 369–IN3. doi:https://doi.org/10.1016/0022-4073(65)90072-5.

[73] C. Amiot, R. Bacis, G. Guelachvili, Infrared study of the $X^2\Pi v = 0, 1, 2$ levels of $^{14}N^{16}O$. Preliminary results on the $v = 0, 1$ levels of $^{14}N^{17}O$, $^{14}N^{18}O$ and $^{15}N^{16}O$, *Canadian Journal of Physics* **56** (1978) 251–265. doi:10.1139/p78-032.

[74] C. Amiot, J.-P. Maillard, J. Chauville, Fourier spectroscopy of the OD infrared spectrum. merge of electronic, vibration-rotation, and microwave spectroscopic data, *Journal of Molecular Spectroscopy* **87** (1981) 196–218. doi:https://doi.org/10.1016/0022-2852(81)90089-8.

[75] C. Amiot, The infrared emission spectrum of NO: Analysis of the $\Delta v = 3$ sequence up to $v = 22$, *Journal of Molecular Spectroscopy* **94** (1982) 150 – 172. doi:10.1016/0022-2852(82)90301-0.

[76] A. Meling, *Scattering of vibrationally excited NO from vanadium dioxide*, Ph.D. thesis, Georg-August-Universität Göttingen **(2020)**.

[77] J. Danielak, U. Domin, R. Ke, M. Rytel, M. Zachwieja, Reinvestigation of the emission γ band system $\left(A^2\Sigma^+ \leftarrow X^2\Pi\right)$ of the NO molecule, *Journal of Molecular Spectroscopy* **181** (1997) 394 – 402. doi:10.1006/jmsp.1996.7181.

[78] G. Herzberg, *Molecular Spectra and Molecular Structure: I. Spectra of Diatomic Molecules*, Van Nostrand Reinhild Company, **1950**.

[79] S. N. Dixit, D. L. Lynch, V. McKoy, W. M. Huo, Rotational branching ratios in (1+1) resonant-enhanced multiphoton ionization of NO via the $a^2\Sigma^+$ state, *Physical Review A* **32** (1985) 1267–1270. doi:10.1103/PhysRevA.32.1267.

[80] N. Bartels, *Orientation–dependent energy transfer in gas–surface collisions: Scattering highly vibrationally excited nitric oxide from Au(111)*, Ph.D. thesis, Georg-August-Universität Göttingen **(2015)**.

[81] J. D. Geweke, *Scattering HCl molecules from Au(111) and Ag(111) surfaces*, Ph.D. thesis, ISIC, Lausanne **(2019)**. doi:10.5075/epfl-thesis-9742.

[82] U. Even, J. Jortner, D. Noy, N. Lavie, C. Cossart-Magos, Cooling of large molecules below 1 k and he clusters formation, *The Journal of Chemical Physics* **112** (2000) 8068–8071. doi:10.1063/1.481405.

[83] D. C. Jacobs, R. J. Madix, R. N. Zare, Reduction of 1+1 resonance enhanced MPI spectra to population distributions: Application to the NO $A^2\Sigma^+ \leftarrow X^2\Pi$ system, *The Journal of Chemical Physics* **85** (1986) 5469–5479. doi:10.1063/1.451557.

[84] N. Bartels, K. Golibrzuch, C. Bartels, L. Chen, D. J. Auerbach, A. M. Wodtke, T. Schäfer, Dynamical steering in an electron transfer surface reaction: Oriented no($v = 3, 0.08 < e_i < 0.89$ ev) relaxation in collisions with a Au(111) surface, *The Journal of Chemical Physics* **140** (2014) 054710. doi:10.1063/1.4863862.

[85] R. Cooper, Z. Li, K. Golibrzuch, C. Bartels, I. Rahinov, D. J. Auerbach, A. M. Wodtke, On the determination of absolute vibrational excitation probabilities in molecule-surface scattering: Case study of NO on Au(111), *The Journal of Chemical Physics* **137** (2012) 064705. doi:10.1063/1.4738596.

[86] R. Cooper, I. Rahinov, C. Yuan, X. Yang, D. J. Auerbach, A. M. Wodtke, Efficient translational excitation of a solid metal surface: State-to-state translational energy distributions of vibrational ground state HCl scattering from Au(111), *Journal of Vacuum Science & Technology A* **27** (2009) 907–912. doi:10.1116/1.3071971.

[87] J. Luque, D. R. Cosley, *LIFBASE: Database and Spectral Simulation Program (Version 1.5)*, **1999**.

[88] I. Rahinov, R. Cooper, C. Yuan, X. Yang, D. J. Auerbach, A. M. Wodtke, Efficient vibrational and translational excitations of a solid metal surface: State-to-state time-of-flight measurements of HCl($v = 2, J = 1$) scattering from Au(111), *The Journal of Chemical Physics* **129** (2008) 214708. doi:10.1063/1.3028542.

[89] G. Comsa, R. David, Dynamical parameters of desorbing molecules, *Surface Science Reports* **5** (1985) 145–198. doi:https://doi.org/10.1016/0167-5729(85)90009-3.

[90] J. Sun, Y. Nam, N. Lindvall, M. T. Cole, K. B. K. Teo, Y. Woo Park, A. Yurgens, Growth mechanism of graphene on platinum: Surface catalysis and carbon segregation, *Applied Physics Letters* **104** (2014) 152107. doi:10.1063/1.4871978.

[91] T. Land, T. Michely, R. Behm, J. Hemminger, G. Comsa, Stm investigation of single layer graphite structures produced on pt(111) by hydrocarbon decomposition, *Surface Science* **264** (1992) 261–270. doi:https://doi.org/10.1016/0039-6028(92)90183-7.

[92] J. Y. Guo, C. X. Xu, F. Y. Sheng, Z. L. Shi, J. Dai, Z. H. Li, X. Hu, Simulation on initial growth stages of graphene on pt (111) surface, *Journal of Applied Physics* **111** (2012) 044318. doi:10.1063/1.3686609.

[93] S. Choubak, M. Biron, P. L. Levesque, R. Martel, P. Desjardins, No graphene etching in purified hydrogen, *The Journal of Physical Chemistry Letters* **4** (2013) 1100–1103, pMID: 26282027. doi:10.1021/jz400400u.

[94] S. Kim, M. Henry, A. G. Fedorov, Using an energized oxygen micro-jet for improved graphene etching by focused electron beam, *Applied Physics Letters* **107** (2015) 233102. doi:10.1063/1.4937118.

[95] A. Kantrowitz, J. Grey, A high intensity source for the molecular beam. Part I. Theoretical, *Review of Scientific Instruments* **22** (1951) 328–332. doi:10.1063/1.1745921.

[96] R. Cooper, I. Rahinov, Z. Li, D. Matsiev, D. J. Auerbach, A. M. Wodtke, Vibrational overtone excitation in electron mediated energy transfer at metal surfaces, *Chem. Sci.* **1** (2010) 55–61. doi:10.1039/C0SC00141D.

[97] C. T. Rettner, J. Kimman, D. J. Auerbach, Inelastic scattering of NO from Ag(111): Internal state, angle, and velocity resolved measurements, *The Journal of Chemical Physics* **94** (1991) 734–750. doi:10.1063/1.460342.

[98] A. W. Kleyn, A. C. Luntz, D. J. Auerbach, Rotational energy transfer in direct inelastic surface scattering: NO on Ag(111), *Phys. Rev. Lett.* **47** (1981) 1169–1172. doi:10.1103/PhysRevLett.47.1169.

[99] D. C. Jacobs, K. W. Kolasinski, R. J. Madix, R. N. Zare, Rotational alignment of NO desorbing from Pt(111), *The Journal of Chemical Physics* **87** (1987) 5038–5039. doi:10.1063/1.452820.

[100] D. C. Jacobs, K. W. Kolasinski, S. F. Shane, R. N. Zare, Rotational population and alignment distributions for inelastic scattering and trapping/desorption of NO on Pt(111), *The Journal of Chemical Physics* **91** (1989) 3182–3195. doi:10.1063/1.456939.

[101] K. Golibrzuch, P. R. Shirhatti, J. Altschäffel, I. Rahinov, D. J. Auerbach, A. M. Wodtke, C. Bartels, State-to-state time-of-flight measurements of NO scattering from au(111): Direct observation of translation-to-vibration coupling in electronically nonadiabatic energy transfer, *The Journal of Physical Chemistry A* **117** (2013) 8750–8760. doi:10.1021/jp403382b.

[102] J. Kimman, C. T. Rettner, D. J. Auerbach, J. A. Barker, J. C. Tully, Correlation between kinetic-energy transfer to rotation and to phonons in gas-surface collisions of NO with Ag(111), *Phys. Rev. Lett.* **57** (1986) 2053–2056. doi:10.1103/PhysRevLett.57.2053.

[103] P. R. Shirhatti, I. Rahinov, K. Golibrzuch, J. Werdecker, J. Geweke, J. Altschäffel, S. Kumar, D. J. Auerbach, C. Bartels, A. M. Wodtke, Observation of the adsorption and desorption of vibrationally excited molecules on a metal surface, *Nature Chemistry* **10** (2018) 592–598. doi:10.1038/s41557-018-0003-1.

[104] S. Köhler, private communications (2021).

[105] A. Politano, V. Formoso, G. Chiarello, Evidence of composite plasmon–phonon modes in the electronic response of epitaxial graphene, *Journal of Physics: Condensed Matter* **25** (2013) 345303. doi:10.1088/0953-8984/25/34/345303.

[106] A. Politano, F. de Juan, G. Chiarello, H. A. Fertig, Emergence of an out-of-plane optical phonon (ZO) kohn anomaly in quasifreestanding epitaxial graphene, *Phys. Rev. Lett.* **115** (2015) 075504. doi:10.1103/PhysRevLett.115.075504.

[107] J. M. Brown, E. A. Colbourn, J. K. G. Watson, F. D. Wayne, An effective Hamiltonian for diatomic molecules: Ab initio calculations of parameters of HCl^+, *Journal of Molecular Spectroscopy* **74** (1979) 294 – 318. doi:10.1016/0022-2852(79)90059-6.

[108] X. Zhou, H. Guo, private communications (2022).

Danksagung

First of all, I would like to thank Prof. Dr. Alec Wodtke for the opportunity to work in his group and for sharing his invaluable knowledge and his wisdom with me. He not only gave me freedom to conduct the experiments that I did, but always had new ideas, if things seemed stuck. Secondly, I would like to thank Prof. Dr. Martin Suhm for being the second referee, and his ideas during our meetings, as well as Prof. Dr. Jürgen Troe, Prof. Dr. Theofanis Kitsopoulos, Prof. Dr. Dirk Schwarzer, and Dr. Daniel Steil for being part of the committee for this thesis. Thanks to Dirk for all the assistance with the nozzle, and to Theo for keeping the spirits high with all those amazing treats you brought from Greece.

Thanks to the Deutsche Forschungsgemeinschaft (DFG) for financing part of this work as a member of project A04 of the SFB1073.

Very special thanks to Dr. Bastian Krüger, who introduced me to the field of surface science during my bachelor thesis, when he was working on his master thesis. All his knowledge that he shared with me, both in the lab as well as in analysis have proven invaluable to my growth as a researcher and as a player of table-soccer. It was an absolut pleasure working with him on the ”orientation machine”. Prof. Dr. G. Barratt Park also joined said machine when I started my PhD and I would like to thank him not only for sharing his amazing spectroscopic knowledge with me, but also for all the great discussions we had on the English and German languages, when we shared and office.

Very special thanks also go to Dr. Tim Schäfer, for all his scientific advice, organization of the group ski-trips, all the pigs we roasted, and most importantly, for always seeing the positive things, even if the lab is on fire (which luckily never actually happened). Without his positive attitude and expertise, repairing all the broken lasers and equipment would definitely have been a lot more challenging. Thank you, you taught me a lot, not only about science.

Special thanks to Dr. Jan Geweke, for introducing me to the ”Beamer I” machine, to all the associated laser systems, and for sharing his knowledge of the time of flight data with me. It certainly made the experiments a lot more managable.

Without the mechanical and electronic workshops (die Werkstätten), most of this work would not have been possible. They were the ones to repair electronic controllers on a moments notice, helping me change super heavy turbomolecular pumps and constructing whatever weird contraptions I needed for the machine to get my experiment working.

I also would like to thank Yingying Cai, and Dominik Vogler for their assistance in the lab during their internship/master thesis. They helped a lot with measuring the data that is presented in this thesis.

Thanks to Kerstin, Tim, and Georg for the nice atmosphere in the office, and thanks to Dr. Oliver Bünermann, Dr. Hongyan Jiang, Dr. Kai Golibrzuch, Dr. Dmitriy Borodin, and Prof. Dr. Sven Köhler for all the interesting discussions and the help in the lab.

Additional thanks to Dr. Tim Schäfer, Dr. Hannes and Dr. Christian for proof reading this thesis.

Special thanks go to Dr. Hannes, Dr. Kathi and Dr. Lara for brightening my days during our shared lunch breaks. The mutual nagging on the food of the Nordmensa made it kind of enjoyable. Last but not least, very special thanks to Judith, for all the moral support during this work, it means a lot to me.

Publikationen

[1] N. Bartels, B. C. Krüger, S. Meyer, A. M. Wodtke, T. Schäfer Suppression of Spontaneous Emission in the Optical Pumping of Molecules: Pump-Dump-Sweep-Probe *J. Phys. Chem. Lett.* **2013**, 2367-2370, DOI: 10.1021/jz401266m

[2] Bastian C. Krüger, Sven Meyer, Alexander Kandratsenka, Alec M. Wodtke, and Tim Schäfer Vibrational Inelasticity of Highly Vibrationally Excited NO on Ag(111) *The Journal of Physical Chemistry Letters* **2016** 7 , 441-446, DOI: 10.1021/acs.jpclett.5b02448

[3] G. B. Park, B. C. Krüger, S. Meyer, D. Schwarzer, T. Schäfer The ν_6 fundamental frequency of the tildeA state of formaldehyde and Coriolis perturbations in the $3\nu_4$ level *J. Chem. Phys.* **2016**, 194308, DOI: 10.1063/1.4948635

[4] G. B. Park, B. C. Krüger, S. Meyer, A. M. Wodtke, T. Schäfer A 1 + 1′ resonance-enhanced multiphoton ionization scheme for rotationally state-selective detection of formaldehyde via the $\tilde{A}^1A_2 \leftarrow \tilde{X}^1A_1$ transition *Phys. Chem. Chem. Phys.* **2016**, 22355-22363, DOI: 10.1039/c6cp03833f

[5] G. B. Park, B. C. Krüger, S. Meyer, A. Kandratsenka, A. M. Wodtke, T. Schäfer An axis-specific rotational rainbow in the direct scatter of formaldehyde from Au(111) and its influence on trapping probability *Phys. Chem. Chem. Phys.* **2017**, 19904-19915, DOI: 10.1039/c7cp03922k

[6] B. C. Krüger, G. B. Park, S. Meyer, R. J. V. Wagner, A. M. Wodtke, T. Schäfer Trapping-desorption and direct-scattering of formaldehyde at Au(111) *Phys. Chem. Chem. Phys.* **2017**, 19896-19902, DOI: 10.1039/c7cp03907g